



HAL
open science

Needle modeling, insertion planning and steering for CT or MR image-guided robot-driven percutaneous procedures

Ederson Antônio Gomes Dorileô

► To cite this version:

Ederson Antônio Gomes Dorileô. Needle modeling, insertion planning and steering for CT or MR image-guided robot-driven percutaneous procedures. Micro and nanotechnologies/Microelectronics. Université Montpellier, 2015. English. NNT : 2015MONTTS222 . tel-02059022

HAL Id: tel-02059022

<https://theses.hal.science/tel-02059022>

Submitted on 6 Mar 2019

HAL is a multi-disciplinary open access archive for the deposit and dissemination of scientific research documents, whether they are published or not. The documents may come from teaching and research institutions in France or abroad, or from public or private research centers.

L'archive ouverte pluridisciplinaire **HAL**, est destinée au dépôt et à la diffusion de documents scientifiques de niveau recherche, publiés ou non, émanant des établissements d'enseignement et de recherche français ou étrangers, des laboratoires publics ou privés.

THÈSE

Pour obtenir le grade de
Docteur

Délivré par **Université de Montpellier**

Préparée au sein de l'école doctorale **Information,
Structures, Systèmes (I2S)**
Et de l'unité de recherche **Laboratoire d'Informatique,
de Robotique et de Microélectronique de Montpellier
(LIRMM)**

Formation Doctorale : **Systèmes Automatiques
et Microélectroniques (SyAM)**

Discipline : **Génie Informatique, Automatique et
Traitement du Signal**

Présentée par **Éderson Antônio GOMES DORILÊO**

**Modélisation, planification et guidage
d'aiguille pour les procédures percutanées
robotisées sous imagerie SCANNER ou IRM**

*« Needle Modeling, Insertion Planning and Steering for CT or MR
Image-guided Robot-driven Percutaneous Procedures »*

En vue d'une autorisation de soutenance
le 25 Septembre 2015 devant le jury composé de

M. Alexandre Krupa, Chargé de Recherche, Rapporteur
INRIA Rennes – Bretagne Atlantique

M. Pierre Vieyres, Professeur, Université d'Orléans Rapporteur

M. Ivan Bricault, PU-PH, Université Joseph Fourier et Examineur
CHU de Grenoble

M. Philippe Poignet, Professeur, Directeur de Thèse
Université de Montpellier

M. Nabil Zemiti, Maître de Conférences, Co-directeur de Thèse
Université de Montpellier

Éderson A. Gomes Dorileo: Needle Modeling, Insertion Planning and Steering for CT or MR Image-guided Robot-driven Percutaneous procedures (*Modélisation, planification et guidage d'aiguille pour les procédures percutanées robotisées sous imagerie SCANNER ou IRM*), © September 2015.

Supervisors: Philippe Poignet and Nabil Zemiti

*To my dear wife, Pâmela.
To the lovely memory of my mother, Ecelise (1959-2012).*

“As we go on maturing, we are a spectacle for ourselves, and, God willing, for others, too. A spectacle, in other words, of limitation and betrayal, and therefore of humiliation, and at the same time of inexhaustible certainty in the power of grace that is given us and is renewed every morning.”

-- Luigi Giussani

Acknowledgments

This thesis represents the cumulative results of a number of opportunities, encounters and lived experiences over the last three years. Being close to situations testing the consciousness of my limits, weakness and uncertainties was prove that it was a very special moment devoted to my personal and professional growth. I would like to express my deepest gratitude to my advisor Philippe, for his patience and for providing me this unique opportunity to work in LIRMM, in special with persons of the Medical Robotics team.

I thank also my co-advisor, Nabil, for his countless contributions and support to my work as well as, the guidance through the pertinent direction.

Thanks to the ROBACUS project’s partners, co-workers and collaborators, especially TIMC-IMAG laboratory, CHU Grenoble (Ivan Bricault) and Axe Systems (Bruno Mouzon and Bruno Schaefer). I was very fortunate to have access to the LPR robot and CT scanner for my needle insertion experiments. Thank you, Céline Fouard, for all the efforts during my days in Grenoble and for your commitment to the ROBACUS project management. I must also thank Jocelyne Troccaz (GMCAO/CAMI) for her welcomed and humanity ever-present. I truly admire her technical experience, but above all, her incredible ability to build human relationship with people around her. I also thank to Nikolai for his comprehension and company during a number of times that we worked together. Thank you, Nicolas, for the technical support with CamiTK. I also recognize that this research would not have been possible without the financial assistance of ANR (*French National Research Agency* - ANR-11-TECS-020-01), LIRMM, Robot Department and the University of Montpellier. I express my gratitude to those institutions.

Thank you to Mr. Etienne Dombre, Chao and Salih for the valuable contributions during the expositions of my work. A very big thank you to all the colleagues of Medical Robotics team for sharing part of their walk with me. Thank you, Mohamed, Jing, Antonio, Mussab, Fabien, Samah, Julien, Gamal, Irina and Alonso for the confidence, for the help, contributions, talks and support during absolutely all the moments during this thesis. My special gratitude to Abdulrahman for its friendship, comprehension and assistance during the insertion experiments under Raven II platform. I also thank the master students Lars and Kilian who worked with me on needle modeling and insertion experiments.

A particular acknowledgement to Cécile Lukasik, Caroline Ycre, Laurie, Nicolas, Virginie, Olivier Floucat, Gildas Cousin, Olivier Tempier and all the staff and lab assistants. Thank you for all kind of technical, administrative, communication and information assistance. The life would be much harder without the work of all of you.

Thank you to Mrs. Izard, Mylene, Quyen, Georges, Stefano, Mathia, Valentina, Luigia, Gérard and a number of other persons that showed how amazing can be unpredictable encounters in our life. Thank you for your company, effective support and friendship.

Teleoperated Robot-Assisted Needle Insertion and Steering

Thank you to Leonardo, Adriana, Ost, Cathy, João, Danny, Raphael, Carol, Garibotti, Manú, Pedro, Renata, Mariana, Guilherme, Flávia, Perin, Cris, Roberto, Raquel and a number of other members of the Brazilian community that passed by Montpellier and left here a little of their history. Thank you for share good and hard moments of the life into this amazing, intense and unique experience of community and fellowship in foreign land.

Of course, I would like to thank my parents, relatives and friends: Antonio and Ecelise (*in memorian*), Rosângela, Edlayne, Alex, Paulo, Mirely, João, Léia, Paolo and Maúna by the force, encouragement and companionship.

Finally, and most importantly, I would like to thank my dear wife Pamela to whom I dedicate this work. No limits for sacrifices and patience when I most needed. Thank you to provide me space and time when it was important to me. Thank you for the nice talks, opportune words, wise advices and above all, confidence. Obstacles overcoming into personal and professional life were witness of her acceptance and commitment to this familiar project. Living together this journey abroad will be always part of our deepest and exciting memories. Let come new ones! (Now, welcoming the little Luciano).

Index

Acknowledgments	5
Index	7
Short Acronym Dictionary	9
Introduction	11
Goals	11
Thesis' organization	12
Chapter 1. Interventional Radiology	15
1.1. Brief history of interventional radiology	15
1.2. Image-guided percutaneous interventions	16
Imaging	16
Needles	17
Clinical aspects of puncture	17
1.3. Interventional robotics	18
ARCS-based robot platforms	19
The LPR robot	20
1.4. Conclusion	22
Chapter 2. Needle-Tissue Interaction Modeling	23
2.1. Locally applied forces and motion	23
2.2. Needle deformation	25
Mechanics-based models	26
Kinematic models	28
Phenomenological models	31
2.3. Toward fundamental numerical-based solutions	33
“Tissue-numerical” approaches	33
Stochastic modeling	35
2.4. Conclusion	35
Chapter 3. The Adaptive Slope Model	37
3.1. Conceptual basis	37
3.2. Preliminary observations	43
Qualitative tissue properties measurements	44
3.3. Results	45
3.4. Conclusion	52
Chapter 4. Teleoperated Robot-Assisted Needle Insertion and Steering	55
4.1. From surgery to remote therapeutic systems	55

■ Early experiences _____	56
■ Navigation for IR gestures _____	57
■ Teleoperated navigation platform _____	58
■ Discussion _____	63
4.2. Adaptive needle insertion planner _____	63
■ Conceptual basis _____	63
■ Methods _____	66
■ Results _____	70
■ Discussion _____	74
4.3. Needle steering assistance _____	74
■ Conceptual basis _____	75
■ Experimental validation of the steering _____	77
■ Steering Results _____	78
■ Discussion _____	82
4.4. Conclusion _____	84
Chapter 5. General Conclusion _____	85
5.1. Thesis' summary _____	85
5.2. Final discussion _____	86
5.3. Contributions _____	88
5.4. Perspectives _____	89
5.5. Publications _____	91
Appendix A: LPR workspace _____	93
Appendix B: Planning algorithm _____	95
Appendix C: Flowcharts for planning with steering _____	97
Appendix D: Geometric model of Raven-II _____	98
References _____	103
List of figures _____	109
List of tables _____	113
Abstract _____	115
Résumé _____	115

Short Acronym Dictionary

ANR	l'Agence Nationale de la Recherche
AR	Augmented Reality
ARCS	Abdominopelvic Robotic-driven semi-rigid needle insertion performed into CT/MR image-guided Scenario
ATM	Automated Teller Machine
CamiTK	Computer Assisted Medical Intervention Toolkit
CT	Computed Tomography
DARPA	Defense Advanced Research Projects Agency
DH	Davit Harteberg
DoF	Degrees of Freedom
FEM	Finite Element Method
GUI	Graphical User Interface
IP	Internet Protocol
IR	Interventional Radiology
LIRMM	Laboratoire d'Informatique, de Robotique, de Microélectronique de Montpellier
LPR	Light Puncture Robot
MRI	Magnetic Resonance Imaging
NASA	National Aeronautics and Space Administration
NEEMO 9	NASA Extreme Environment Mission Operations
NIH	National Institutes of Health
RFA	RadioFrequency Ablation
RR	Rayleigh-Ritz
RT	Real Time
TCP/IP	Transmission Control Protocol
TIMC-IMAG	laboratory of Techniques for bioMedical engineering and Complexity management – Informatics, Mathematics and Applications – Grenoble
UDP	User Data Protocol
US	Ultrasound

Introduction

Interventional Radiology (IR) treatments now play a major role in many disease processes and continue to mushroom with novel procedures appearing almost, on a yearly basis. Indeed, advances of robotic and computer aided systems have become an established part of IR's clinical routine. Many physicians have enumerated the advances of using robot-assisted systems, however its true potential has yet a lot to be explored. Moreover, difficulties such as decreased workspace, reduced visibility, ionizing radiation absorption are imposed every day to the interventional radiologist. In such context, robotic assistance aims to aid radiologists to overcome such difficulties, making the IR act more accurate and safer.

Nevertheless, limitations of generic robot platforms - notably regarding to the ferromagnetic incompatibilities and impossibility to work under reduced workspace - prevent their use, especially when using imaging modalities such as Computed Tomography (CT) or Magnetic Resonance Imaging (MRI). Additional constraints are expected in the context of abdominopelvic CT/MRI-guided percutaneous interventions, in which only a few robots can currently perform translation, rotation and insertion.

Goals

General Goal

This thesis was designed inside of the context of the TECSAN ROBACUS project, granted by the ANR (*l'Agence Nationale de la Recherche*): ANR-11-TECS-020-01. The project proposes extending previous experience related to the development of the LPR puncture robot towards: a) development of a new version of the LPR; b) advance robot validation through the several phases of clinical tests; c) improve needle insertion planning and control tasks; d) develop teleoperation architecture; e) study detection and compensation feasibility for physiologic movements of the target.

Part of the goals exposed above is subject of scientific studies and industrial development and is being conducted in parallel by other partners. The prototype version of the LPR (*Light Puncture Robot*) used in this study is called *Arli*. It will be presented in the next chapter, as well as its architecture and main characteristics.

Specific Goal

The study presented in this thesis contributes to the works developed previously in the development of the CT/MRI-guided LPR (*Light Puncture Robot*) robot (Zemiti et al., 2008) (Hung et al., 2011). Now, we propose methods with potential to improve accuracy and feasibility of this robot platform under ARCS (*Abdominopelvic Robotic-driven semi-rigid needle insertion performed into CT/MR image-guided Scenario*). We target procedures involving kidney therapies and biopsies.

As specific goals, we aim to:

- Develop a teleoperation architecture aiming to support percutaneous insertions;
- Develop an ARCS-compatible modeling and needle insertion planning.

Thesis' organization

The works developed in this thesis aim to contribute with the study and development of applications proposed to improve targeting accuracy and safety into robot-assisted needle interventions. Teleoperation architecture allows performing insertion of the needle at a distance. It could prevent the ionizing radiation of the radiologist under CT-guidance. In addition, it could offer the possibility to perform needle insertion under space constraints of MRI bore.

During the insertion, the interaction of the long needle with the tissue causes needle deflection orthogonal to the insertion direction. A needle deflection prediction model is merged into strategies in order to support insertion point assistance, adaptive needle insertion planning and needle steering. The Fig. 1, provides a graphical outline for the various computational and physical systems needed to achieve teleoperated robot-assisted needle insertion. Main efforts of this thesis are associated to the demands related to the computation systems illustrated, aiming to provide support to offline and online (adaptive) needle insertion planning, needle steering, interacting with a Graphical User Interface (GUI) developed under a teleoperation architecture.

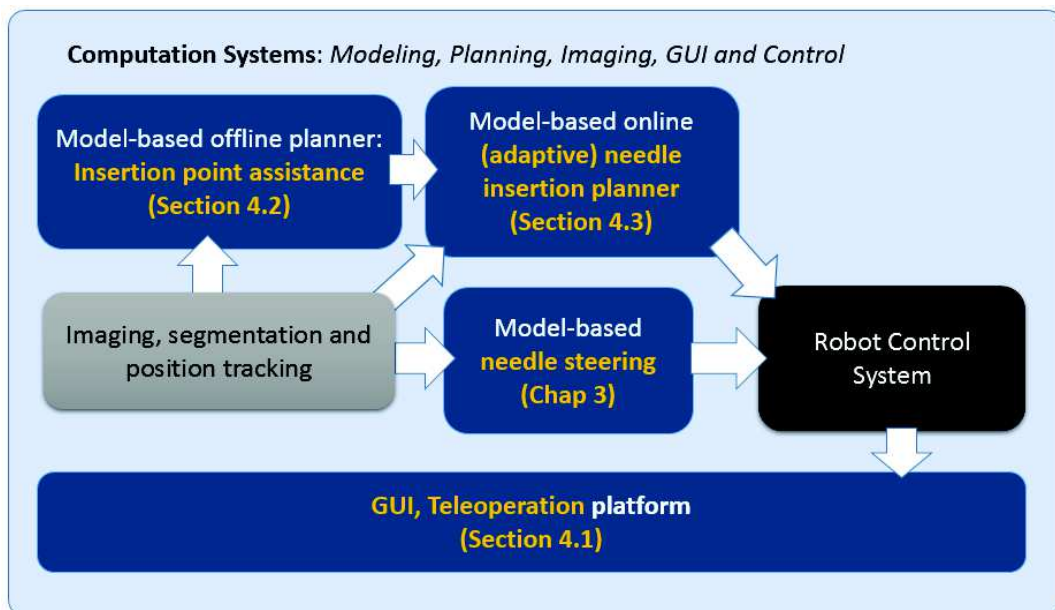


Figure 1 - Computational and physical systems that outline the work developed in this thesis.

This thesis is organized as follows: In Chapter 1 and 2, the goal is to provide basics for an easy comprehension of the following chapters. Chapter 1 presents a review on the main concepts behind IR and robot-driven needle insertions, with focus on the ARCS-compatible platforms. Next, Chapter 2 discuss effects of forces involved into needle-tissue interaction, as well as main needle's deflection prediction techniques presented in the literature. The main contributions of this thesis are presented in the Chapter 3. We devised an in-depth study on needle-tissue interactions to assist semi-rigid needle modeling that supports ARCS-compatible needle's tip deflection prediction. As first step, needle tip deflection is characterized through of merging of needle-tissue properties, tip asymmetry and needle tip position updates. Next, in Chapter 4, the robustness of the prediction model is evaluated under an unknown context such as a different robotic platform, facing uncertainties conditions not conceived previously in the model's confection. In addition, insertion experiments were design to validate an adaptive needle insertion planner that uses the model as predictor's strategy. It provides preoperative planning assistance, as well as intraoperative decision-making support. Finally, we evaluate the

feasibility and advantages of merging steering assistance, offline deflection prediction and online adaptive corrections. Cross-platform validation tests are proposed to evaluate the potential of the needle deflection prediction when submitted to unknown experimental conditions into different scenarios.

Works performed during the three years of this thesis have been carried out in collaboration with the TIMC-IMAG team. From the University Joseph Fourier, Grenoble. This work has been the object of publications in international conferences (CARS'14, ICRA'15 and CARS'15). The publications and work references are respectively listed in special section, in the end of this thesis.

Chapter 1.

Interventional Radiology

The past decades have witnessed the notable development of Interventional Radiology (IR). Also referred to as Surgical Radiology, IR is an independent (minimally invasive) medical specialty, which was a sub-specialty of Radiology until recently. According to (Hungar, 2014), 11.5 million IR acts were realized in the US in 2008, of which 35% were non-cardiovascular. The popularity of these acts has incited a growing interest in robotic-assisted techniques.

In this chapter, a brief overview of IR and image-guided percutaneous needle insertions is given. Brief history and concepts into IR, clinical issues and demands involving image-guided percutaneous interventions are discussed. Next, an overview of the current interventional robotic systems compatible with ARCS is presented as well as, their potential benefits, advantages and drawbacks.

1.1. Brief history of interventional radiology

The birth of interventional radiology. IR was developed from diagnostic angiography and from the innovative minds and technical skills of many angiographers. Early history began in the 1920's with the development of the angiography technique, which constitutes the basis for vascular interventions. Modern medicine was later pioneered with the invention of angioplasty and catheter-delivered stent. It was conceived in the early 1960s by Charles Dotter (Friedman and Dotter, 1989) and the first official spoke about IR was on June 19th, 1963 at the Czechoslovak Radiological Congress in Karlovy Vary. His more than one hour presentation was titled "*Cardiac catheterization and angiographic techniques of the future*". Dotter discussed among other topics, catheter biopsy, controlled exit catheterization, occlusion catheterization for various purposes and the rationale of catheter endarterectomy". Then, after his conclusion he stated that "the angiographic catheter can be more than a tool for passive means for diagnostic observation; used with imagination, it can become an important surgical instrument". Until then, none of them had even thought that it might be able to treat patients percutaneously with use of catheters and guide wires. Also, none between the presents at the congress realized or even dreamed that Dotter's words would soon become reality (Rösch, Frederick and Kaufman, 2003).

IR was born on January 16th, 1964, when Dotter percutaneously dilated a tight, localized stenosis of the superficial femoral artery (SFA) in a 82-year-old woman with painful leg ischemia and gangrene who refused leg amputation. The dilatation of the stenosis was successfully performed with a guide wire and coaxial Teflon catheters. After that, the circulation returned to her leg. Charles related that his skeptical surgical colleagues kept the patient in the hospital under observation for several

Introduction

weeks expecting the dilated artery to thrombosis. However, she left the hospital on her feet-both of them. The dilated artery stayed open until her death from pneumonia 2.5 years later.

The term “Interventional Radiology” was coined by a gastrointestinal radiologist called Alexander Margulis, in 1967 and issued in the editorial of the *American Journal of Roentgenology* (Margulis, 1967).

Occasional reports published previously in mid 1960s were published on treatment with radiologic techniques involving transluminal angioplasty, shoulders treatments using aortography, abscess drainages, intrauterine transfusion of fetus under fluoroscopic guidance, pulmonary and liver biopsy, catheter placement for intra-arterial chemotherapy and trans-jugular cholangiography.

Margulis realized that a new trend and a new specialty were developing in radiology. In his editorial, he not only defined interventional radiology, but also set requirements for its performance that are still valid today. He defined IR as manipulative procedures controlled and followed under fluoroscopic guidance that may be predominantly therapeutic or primarily diagnostic. High-quality radiologic imaging equipment was one of basic requirements for performance of interventional radiologic procedures. Dotter was not enthusiastic about the term “interventional”, calling it imperfect. His main reservation about the term interventional was its lack of definition of the work. He believed that this term leads to confusion about what they do among the lay public and many physicians. However, he realized that the generalized use of the term “Interventional Radiology” allowed definition of a new subspecialty in radiology and separated it from general radiology and its other subspecialties.

The official recognition of IR as a “new component of the specialty of radiology” took place at the 2001 annual meeting of the American College of Radiology (ACR).

1.2. Image-guided percutaneous interventions

IR can provide minimally invasive treatments of many illnesses, with a number of advantages over open surgical interventions. It uses minimally invasive image-guided procedures to diagnose and treat diseases in nearly every organ system. The concept behind IR is to diagnose and treat patient using the least invasive techniques currently available in order to minimize risk to the patient and improve health outcomes.

1.2.1 Imaging

An important characteristic of IR is its reliance on medical imaging technology to visualize diseases in the body and guiding minimally invasive tools (such as needle and catheters) to these diseased targets. The primary imaging technologies used in IR are ultrasound (US), X-ray (fluoroscopy, CT) and MRI. CT and MRI are the modalities of major interest for this study.

CT scanners are fast and efficient. They can acquire 3D volumes of any part of the body, with excellent resolution. Differentiation of soft tissue allows the interventional radiologists to target regions with high accuracy. However, 3D volume acquisition and reconstruction intervals are far from real-time (RT). Their availability has increased over the years (OECD, 2012), while MR imaging is by far the least used for interventional guidance. Besides of the advantages of MRI are significant, high cost and ferromagnetic compatibility issues make it a difficulty modality to use for IR procedures. Finally, its improved ability to detect lesions is very attractive for IR by providing a more targeted approach.

IR techniques can be applied using different ways: vascular (arteries and veins), natural (urinary and digestive system), percutaneous (through the skin) or transcutaneous (truly noninvasive, as they do not require surgical access - e.g., MRI-guided focused US surgery of brain tumors). The work developed in this thesis is particularly interested into interventions using percutaneous way.

1.2.2 Needles

Image-guided percutaneous needle placement interventions have become the standard of care in many procedures such as biopsies, aspiration, drugs delivery or tumor ablations.

Percutaneous therapies, typically involves the insertion of tubular delivery devices into target locations in the body with the aid of intraoperative imaging guidance. These delivery apparatuses include instruments such as needles, trocars, bones drills, screws, etc. For the context of this thesis, we will focus on the needles as delivery instruments.

Needles offer several evident advantages over traditional surgery, including less scarring, lighter anesthesia, reduced postoperative pain, reduced complications and faster discharge from the hospital. Conventional needles used in percutaneous therapy and biopsy can be classified as symmetric (e.g. conical or triangular prismatic) or asymmetric (e.g. beveled). The commonly used unity of measure inputted to needles (and to the other delivery tools) is called *gauge* (Fig. 1.1) It corresponds to the internal diameter of the material. In short, it means the number of needles that is possible to insert into a template having the diameter of one inch (1 inch = 2.54 cm).

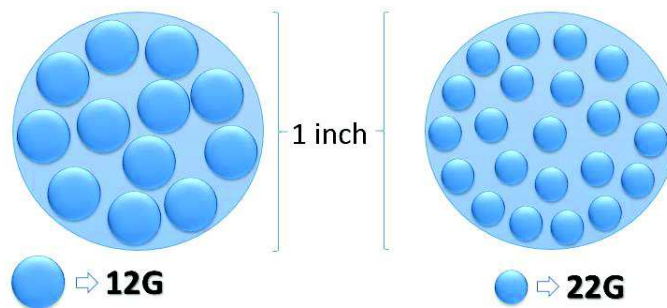


Figure 1.1 - Left: Its is possible to insert 12 needles in the cylinder of 1 inch of diameter. Right: Considering the same cylinder, it is possible to insert 22 needles. These needles (22G) are thinner than the previous one (12G).

The larger is the gauge, smaller is the needle diameter and vice-versa. Therefore, a 24G needle will be used to veins of small caliber, while an interventional tool of 14G would be pertinent to be used into an urgent transfusion, requiring high flow and by consequence, a large needle.

Qualitative definitions of needle stiffness have been found in the literature. They are so varied as rigid, semi-rigid, lightly-flexible, flexible and so on. Because of the lack of an official classification of the needles relating the quantitative properties to the qualitative definitions, often it happens that same needle is characterized using different qualifications or else different qualifications are applied over the same needle.

For sake of nomenclature, *rigid needles* will be hereafter, considered to be the ones that present neglectable deflection during insertion. *Flexible needles* will be the wires such as nitinol that present important deflection when holding one of its extremities in the horizontal position. Therefore, we will call *semi-rigid needles* the needles that are not rigid or flexible. For example, in this study we used 20 cm stainless needles between 18G and 20G.

1.2.3 Clinical aspects of puncture

Punctures procedures performed into clinical scenario, typically includes three decoupled tasks, considering (freehand) needle insertions (Fichtinger et al., 2008):

- 1) *Touch down with the needle tip on the skin entry point, which requires three-dimensional Cartesian translation motion;*
- 2) *Orient the needle by pivoting around the skin entry point, which requires two independent rotations about intersecting axes;*

Introduction

- 3) *Insert the needle into the body along a straight trajectory, which requires one-dimensional translation, possibly combined with some steering effect.*

Percutaneous IR procedures usually begin with a planning stage in which the physician closely examines preoperative images of the patient obtained prior to the intervention. Images from various modalities can be compared in order to make preliminary diagnosis upon which the intervention is based. The intraoperative planning stage starts on the day of the intervention as soon as the patient is installed. The conventional routine for abdominopelvic percutaneous interventions can be associated to the events as described following.

The interventional radiologist takes a first image, plans the insertion on the image and then, tries to mentally reproduce the planned insertion on the patient. This is done by progressively and iteratively inserting the needle bit by bit. At each small insertion, he/she takes a new image to check if the needle is still on the planned trajectory. This loop is repeated until the needle tip reaches the target. If the needle moves off-target during the insertion, the interventional radiologist can withdraw the needle partially or entirely and re-plan and re-insert. These steps result in a procedure that requires a large number of images and in which the radiologist must pass repeatedly from the imaging control room to the patient numerous times.

The process is very delicate since the clinician has a few tools to guide needle insertion. Therefore, the procedure quality is directly connected to the clinician experience. In short, he/she trust on his/her experience and memory in order to perform the planned insertion. Then, he/she must switch between progressive needle insertion and imaging feedback in order to check if the needle trajectory is in accord with the planned one. During acquisitions, the physician could perform manual insertion using online image feedback. However, even though, some additional constraints are yet expected: a) under CT he/she would be irradiated by X-ray, as well as the patient; b) for CT or MRI machines, 3D imaging feedback is not commonly available in real-time or even online (it could take around 4-5s or more depending on the volume and resolution required). In this case, the drawback concerns to the lack of visual information feedback out of the insertion plane. The consequence of this over the design of this work will be discussed further.

From the clinical point of view, the established benefits of classical (freehand) IR are extensive and beyond dispute, but many of the procedures also have the potential to produce patient radiation doses and occupational doses to interventional radiologists high enough to cause concern. According to (Stecker et al., 2009), the radiation dose received by interventional radiologists can vary by more than an order of magnitude for the same type of procedure and for similar patient dose. The use of interventional robots and teleoperators could improve the efficiency, precision and consistency of such processes, while reducing the procedure time, avoiding radiation to the clinician and promoting more comfort to the patient.

1.3. Interventional robotics

We are just around 3 decades from the time when the first robot was used to assist minimally invasive interventions and robots are just beginning to be widely used in the interventional suite. They were introduced in the 1980s, after the dawn of the information age (Rösch, Frederick and Kaufman, 2003).

The development of robots for IR assistance is motivated primarily by the desire to improve effectiveness of a procedure by assembling information to action during the intervention. In contrast to industrial robots, these latter are used since 1961 and developed primarily to automate dirty, dull and dangerous tasks. The evident reason for this dichotomy is that medical care requires human judgment and reasoning to handling a variety and complexity of human anatomy and disease processes. A number of sources - including patient-specific data (*e.g.*, vital signs and images), general medical knowledge (*e.g.* atlases of human anatomy) and physician experience - can generate information that influences medical actions. Computer-assisted interventional systems can gather and present information to the interventional radiologist in a more meaningful way and, via the use of robots,

enable this information to influence the performance of an intervention. It has the potential to improve the consistency and the quality of the clinical result.

Primary motivation for using interventional robots includes potential benefits such as the fact that a robot can usually perform a task more accurately than a human. Moreover, teleoperators can work in areas that are not human friendly (e.g., X-rays) and inaccessible environments including space-constrained areas, such as the inside the patient body or the bore of an imaging system.

Robots are rarely designed to replace a member of the surgical or interventional team. Rather, they are intended to augment the medical staff by imparting superhuman capabilities, such as high motion accuracy, or to enable interventions that would otherwise be physically impossible. Therefore, methods for effective human-robot cooperation are one of the unique and central aspects of medical robotics (Kazanzides et al., 2008).

1.3.1 ARCS-based robot platforms

A multitude of robotic platforms have been described in the literature and that could address most of the difficulties described in the previous paragraphs through abdominopelvic robotic assistance. Such platforms can be classified into two categories: bed-mounted robots and patient-mounted robots (Hung, 2014).

Example of bed-mounted robot is the AcuBot (Stoianovici et al., 2003), a CT-guided robot, which uses a bridge-like macro-micro architecture to insert a needle with 1-2mm precision. Ferromagnetic compatibility issues limit the motor of AcuBot to be used into MRI-guided scenario.

Innomotion (Schell et al., 2012) (Melzer et al., 2008) is a MRI-guided robot that extends over the patient and is bridge-mounted. It uses pneumatic actuators coupled with optical sensors to drive the robot. This robot platform is the only one tested clinically. Needle insertion is performed manually in this platform.

A third example is the B-RobII/iSYS1 platform (Kronreif et al., 2003) which uses two parallel fingers to align the needle above the target, allowing the clinician to insert the needle manually.

Patient-mounted robot platforms are often smaller and able to move with the patient. The effect of motion due to patient discomfort as well as effect of breathing motion over the insertion point on the patient's skin can be minimized to a certain extent. CT-Bot (Maurin et al., 2008) is an example of robot that uses ultrasonic motors to power a parallel-structure with 5 degrees of freedom (DOF). It uses a single line-fiducial mounted on the base of the robot for registration with the CT images, allowing an accuracy of <5mm at typical needle insertion depths (*i.e.*, 50-100 mm). The Robopsy (Barrett, Hanumara and Shepard, 2005) is another example of CT-guided robot that has 3 DOF for needle orientation and insertion, while positioning at the skin insertion point is manual. Neither of these robots are MRI compatible. Fig. 1.2 shows the main IR robot platforms compatible to abdominopelvic procedures, as mentioned above.

It is important to mention that, as far as we know, the patient-mounted LPR (Zemiti et al., 2008) (Hung et al., 2011) is the only CT and MRI-compatible platform that can perform needle translation, orientation and insertion, in the context of abdominopelvic percutaneous procedures (Table 1.1). Its teleoperated platform (Dorileo et al., 2014) allows radiation avoidance, decreasing the exposition of the clinician during CT-guided procedures. Additionally, human-in-the-loop systems are well known for increasing the safety of the insertion procedures (Pacchierotti et al., 2014).

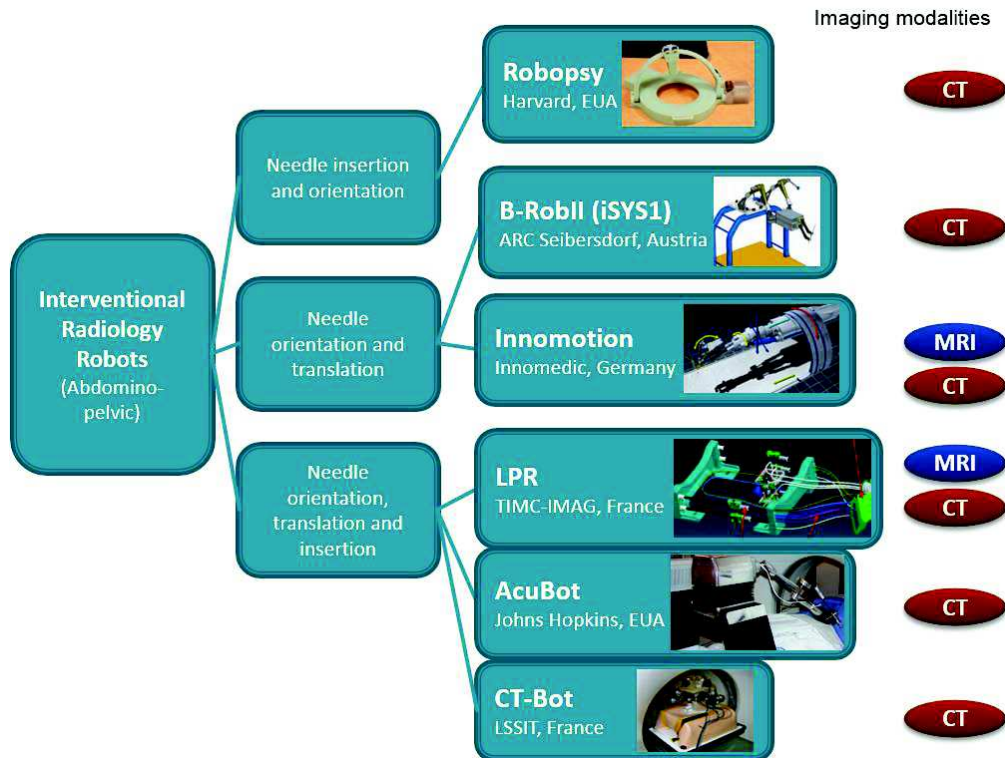


Figure 1.2 - Main Interventional Radiology robots for abdominopelvic procedures.

Table 1.1 - Main robot platforms devised to assist CT/MRI-guided needle insertion for abdominopelvic procedures. The robot validation test is either clinical patient tests (C), live animal tests (A) or phantom tests (P). Robotized needle motions are either translation (T), orientation (O) and/or insertion (I).

Institution	Country	Robot	Validation tests	Imaging modality	Actuation technology	DOF	Needle motions		
							T	O	I
J. Hopkins	USA	B-RobII/iSYS1	P	CT	motor	4	X	X	
J. Hopkins	USA	Acubot	P	CT	motor	6	X	X	X
LSIIT / ICUBE	FRA	CtBot	A	CT	US motor	5	X	X	X
MIT	USA	Robopsy	A	CT	US motor	3		X	X
Innomedic	GER	Innomotion	C	CT/MRI	pneumatic	5	X	X	
TIMC-IMAG	FRA	LPR	A	CT/MRI	pneumatic	6	X	X	X

Such characteristics have lead LPR through promising studies towards clinical validation. Therefore, the experimental conditions released by this robot platform provides odd opportunities to understand the input challenges for needle deflection prediction models and steering algorithms committed to face the ARCS constraints. The LPR robot platform will be presented in details below.

1.3.2 The LPR robot

This section introduces CT and MRI guided interventional radiology robot for percutaneous needle interventions, developed at TIMC-IMAG (laboratory of Techniques for bIoMedical engineering and Complexity management – Informatics, Mathematics and Applications – Grenoble), France. The 6-DoF (Appendix A) patient-mounted LPR has nearly 2 kg and was designed to perform abdominal and thoracic punctures (Zemiti et al., 2008). It has a parallelogram-type manipulator and inserts the needle progressively using piezo motors and pneumatic actuators (Hung et al., 2011). Two strategically placed fiducials are visible under CT and MR images and allow registration of the needle position and inclination in the images. It can translate, orientate and perform percutaneous needle insertions. The Fig. 1.3 shows its control box, motor box, cables and housing.

According to (Hungr et al., 2011), the robot presented following characteristics during the tests:

- It was entirely sterilizable with hydrogen peroxide gas;
- No images artifacts or deformations were noticeable in the CT and MRI;
- It did not affect signal to noise ratio of MR images
- Its mechanical error was observed to be less than 5mm;

The main feature of this robot compared to other existing systems is its compatibility with both CT and MRI guided percutaneous procedures, significantly enlarging its clinical scope.

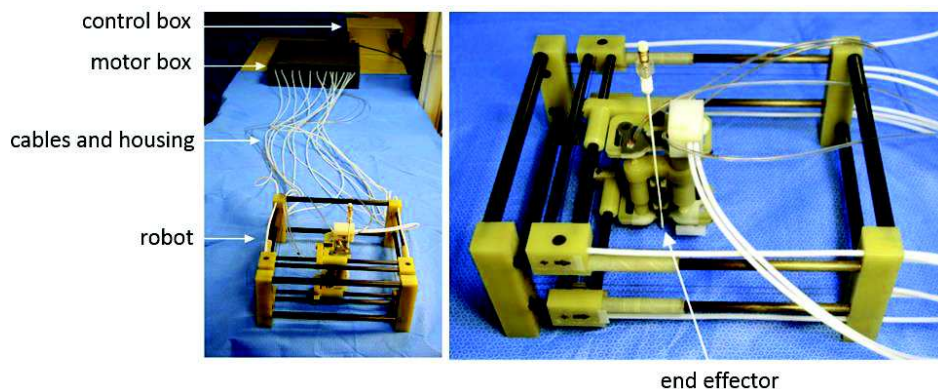


Figure 1.3 - LPR robotic system. Left: main LPR components. Center: parallelogram-type manipulator and needle. Right: Grippers and needle.

The robot architecture is shown in Fig. 1.4. It is based on a parallelogram design, in which the needle is held by two parallel pipes, 85 mm apart, that enable a maximum planar translation of 135mm and a maximum needle inclination of $\pm 60^\circ$ in one direction and $\pm 15^\circ$ in the other. The needle is held by two independent grippers the upper one being mounted on a vertical slider and providing the needle insertion force. The frame is strapped to the patient's body to follow external movements. For safety's sake, the grippers can be released at any time, allowing the switch to manual insertion or needle withdrawing.

Needle insertion is done incrementally by sequentially activating the two needle grippers and the insertion slider (Fig. 1.5). The stroke distance (adjustable between 0 and 40mm) is regulated by a controllable stop that blocks the vertical slider's path. The stop height is regulated by a screw connected to a set of reduction gears.

The characteristics of this robot system, as described above, show an important potential benefit to improve the quality and feasibility of percutaneous IR procedures.

This robot is under continuing development since part of the ROBACUS project is committed to advancing its architecture to a new prototype version towards clinical validation levels.

Introduction

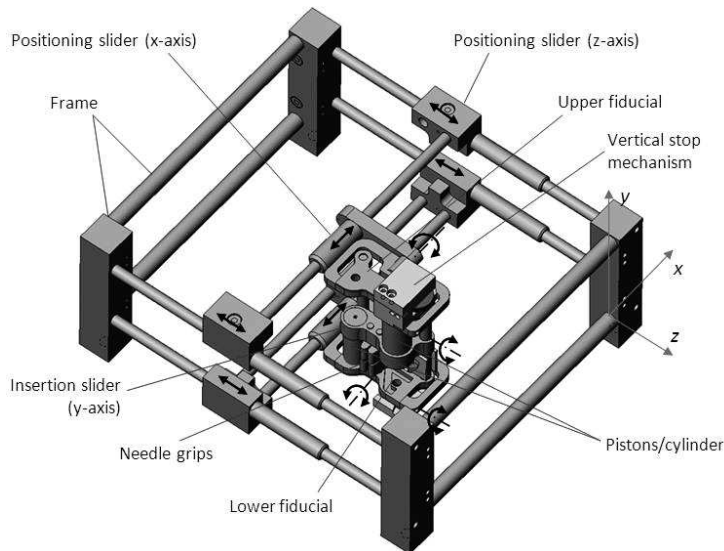


Figure 1.4 - LPR robot architecture. The needle is denoted by a vertical red line in the left image. Source: (Hung, 2014).

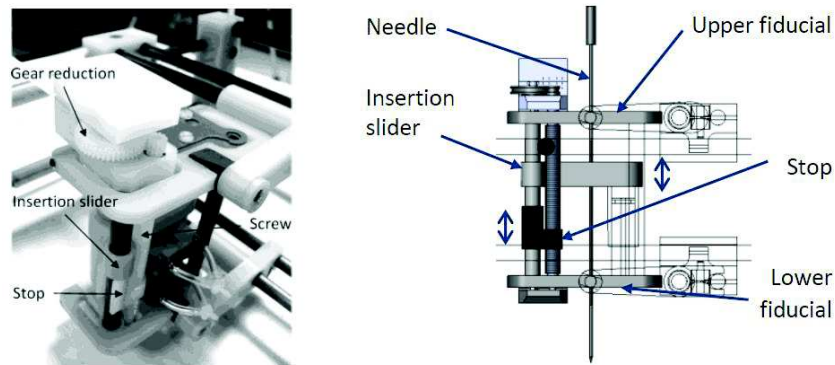


Figure 1.5 - Stop mechanism for inserting the insertion stroke. Source: (Hung, 2014).

1.4. Conclusion

Image-guided robotic systems are clinically viable and promise to substantially enhance targeting accuracy in needle-based interventions.

A number of robot platforms have been proposed to provide IR assistance into abdominopelvic CT/MRI-guided context. However, often, the existent robot platforms cannot perform the full range of decoupled tasks (needle rotation, translation and insertion) demanded for needle punctures. To date, these systems require minimal tissue and needle deformation. Therefore, substantial effort is committed to preventing such deformation because unmodeled deflections of the needle or tissue during insertion, if not compensated, will lead to gross targeting inaccuracy.

The LPR robot can perform inclination, translation and insertion of the needle and it is compatible to ARCS. The next chapters in this work will show the concepts, obstacles and approaches involved in the development of a teleoperation platform and needle insertion assistance compatible to this scenario.

Chapter 2.

Needle-Tissue Interaction Modeling

The previous chapter provided a brief overview of IR and clinical aspects of image-guided percutaneous insertions with description of the current ARCS-compatible interventional robotic systems. The design of motion and steering planners requires a model that predicts needle deflection when interacting with soft tissues. In this chapter, we discuss the effects of needle-tissue interaction in the relation between the locally applied force and motion. Also, we provide a taxonomy of needle's deflection prediction techniques, including last literature models. We show how kinematics and mechanics-based models have captured needle-tissue behavior, as well as ongoing efforts of phenomenological and fundamental numerical-based solutions have being used to assist needle deflection prediction when inserted in soft tissues.

2.1. Locally applied forces and motion

The study of forces acting during the insertion of a needle into soft tissue is important because they can help to provide relevant information about the needle insertion protocol, needle-tissue interaction, tissue relaxation and other relevant feedbacks to the robot-assisted system (Bernardes, 2012). However, there is no way to measure the local force directly since force sensors can only detect the force at their attached point (proximal end) (Kataoka, Washio and Chinzei, 2002). What actually happens is that penetration forces are distributed along the entire length of the needle shaft and needle tip. Such forces are sources of phenomena such as cutting, elastic tissue deformation, needle deflection and friction. Therefore, the needle insertion force measured is the integration of such force distribution along the needle (Simone and Okamura, 2002).

Perfectly symmetric-tip needle when inserted into homogeneous tissue produces forces that are equally distributed in all direction and the cut of tissue occurs in the insertion direction. During needle insertion, the tissue around the tip deforms due to compression. It imposes a reaction force contrary to this compression as shown in Fig 2.1.

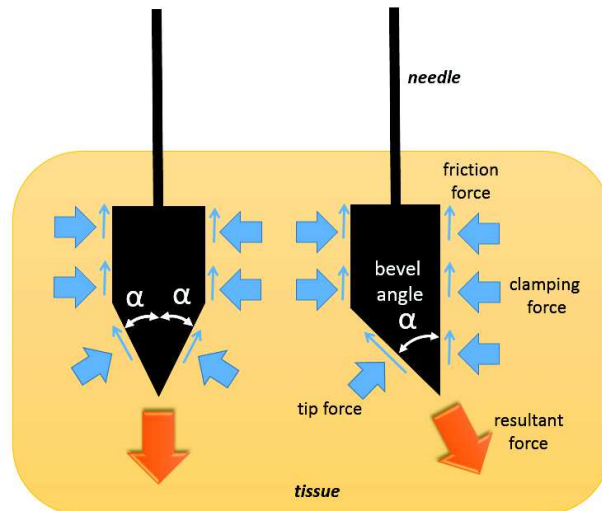


Figure 2.1 - Symmetric and asymmetric forces actuating respectively on prismatic/conic (left) and bevelled (right) needle tips during insertion. Bold arrows indicate the resultant force acting at the distal end. Thin arrows show the clamping forces that cause the friction (Kataoka, Washio and Chinzei, 2002) and are distributed along the needle tip and shaft.

A pioneering methodology for estimating the force distribution that occurs along the needle shaft was proposed by DiMaio and Salcudean (DiMaio and Salcudean, 2002) (DiMaio and Salcudean, 2003) (DiMaio and Salcudean, 2005). They explored the relationship between needle forces and 2D tissue deformation during needle insertion. The simulation was based on a linear elastostatic material model, discretized using the FEM to derive contact force information that is not directly measurable. The obtained force distribution indicated the existence of two forces: an axial and uniform friction force between the needle and the tissue and a force peak at the needle tip, which results from the cutting of the tissue as illustrated in the Fig. 2.2.

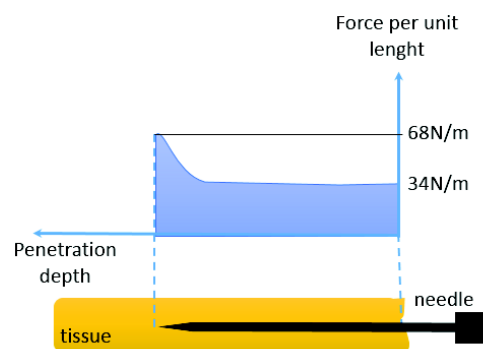


Figure 2.2 - Estimated needle force distribution for a 1mm/s insertion: constant along the needle shaft and higher at the tip. Adapted from (DiMaio and Salcudean, 2002).

Simone and Okamura (Simone and Okamura, 2002) modeled such forces from experimental *ex-vivo* studies (bovine liver). Insertion of a bevel-tip semi-rigid needle was divided in stages of needle insertion, such as pre-puncture, puncture and post-puncture of the organ membrane (Fig. 2.3).

During the pre-puncture, the stiffness forces $f_{stiffness}(x)$ due to the elastic properties of the organ were modeled as a non linear spring with elastic constant obtained by curve fitting the experimental data. The force value rises steadily as the insertion proceeds until a sharp drop indicate the rupture of the liver membrane. For purposes of modeling, they separated force into components, whose subsequent variations are due to stiffness, friction and cutting forces as shown below.

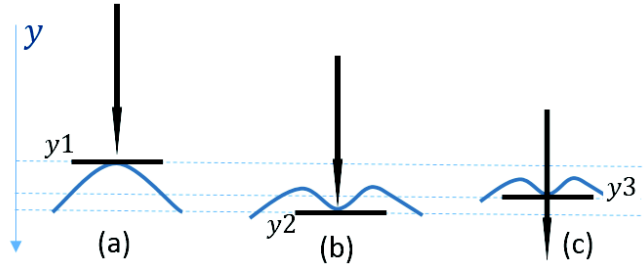


Figure 2.3 - Locations of the tissue surface at different stages of needle insertion. (a) pre-puncture; (b) puncture; (c) post-puncture. y_1 , y_2 and y_3 are the positions of the tissue surface relative to a fixed coordinate system before the puncture. Adapted from: (Simone and Okamura, 2002).

$$f_{needle}(x) = f_{stiffness}(x) + f_{friction}(x) + f_{cutting}(x) \quad (2.1)$$

During post-puncture, friction force $f_{friction}(x)$ and cutting forces $f_{cutting}(x)$ are added to the pre-puncture stiffness force. In order to model the friction during needle insertion, a modified Karnopp friction model, including both static and dynamic friction coefficients, was used. Finally, the cutting forces were obtained by subtracting the puncture and friction force from the total measured force.

Forces involved during *in vivo* percutaneous procedures into liver and kidney of anesthetized pigs were studied by (Maurin et al., 2008). They fitted their experimental data to Simeone and Okamura's model and to a second-order polynomial model taken from (Maurel, 1999), having low errors for both models. The results of CT-guided experiments using semi-rigid needle also confirmed the increase in the insertion forces during membrane punctures. Measurements of insertion forces involved into deflections of pyramidal-tip semi-rigid needle during insertion into a canine prostate were investigated by (Kataoka, Washio and Chinzei, 2002). They were able to measure separately shaft forces and tip forces using a needle consisting of an outer and inner part. The study of friction forces was important to determine the mechanical characteristics of the prostate tissue upon penetration. Moreover, it helped to detect surface puncture, which make possible to estimate the true insertion depth of the needle in the tissue.

The work developed by (Alterovitz et al., 2003), proposed an alternative approach to the modeling of interaction forces. A 2D linear elastic model discretized with a finite element mesh was used to simulate the prostate tissue during a brachytherapy procedure and analyze the sensitivity of tip positioning errors to needle, tissue and trajectory parameters. The effects of changes in the insertion depth, needle sharpness, friction, velocity and tissue mechanical properties were evaluated but only tissue deformation was considered in their simulations, while needle deflection was ignored. Extension of such work to a 3D model was done by (Nienhuys and Stappen, 2004). Using an element subdivision approach to ameliorate the effects of added computation complexity, they considered homogeneous models and rigid needles, neglecting again the effects of needle deflection.

Studies and observations during percutaneous insertions into elastic tissues have showed that the force data - collected from the needle insertion procedures - are a summation of stiffness, friction and cutting forces (Okamura, Simone and O'Leary, 2004). However, the energy of pure needle bending (transversal forces) dominates the total energy contribution to the system for insertions smaller than ~ 100 mm (Misra et al., 2009). They showed that the needle deviation during insertion can be described using energy-based approach and that the needle-tissue interaction and the transverse force in the needle tip holds 99.9% of the stored strain energy during the needle insertion. We will discuss about this work below.

2.2. Needle deformation

A number of works have put efforts in the modeling of needle deformation during interaction with soft tissue. Some studies propose methods for estimating the needle tip motion based on fundamental material, geometrical or motion properties of the needle and tissue, while other

approaches use empirical observations of each needle and tissue combination in order to fit model parameters. Finally, a number of approaches have used numerical simulation to estimate main parameters associated to needle-tissue interaction or predicting needle deviation. Such techniques are discussed in details as follows.

2.2.1 Mechanics-based models

Mechanics-based models aim to relate the needle tip trajectory to the material and geometric properties of the tissue and needle. They have been proposed by several groups to represent needle deformation.

A force-deflection model was proposed by (Kataoka et al., 2001). They described the amount of needle deflection during insertion as function of the needle length inside and outside the tissue, the needle diameter, the needle Young's modulus, the moment of inertia and the force per length (ω) - defined as a new physical quantity, analogous to traction (force for surface area). The force at the fixed end of the beveled semi-rigid needle and the deflection of needles of several diameters were measured using a force sensor and a bi-plane X-ray imaging system. The model supposes the constancy of ω over the needle insertion depth, assuming the relevance of all the parameters embedded in the model. However, no reference to the mechanical properties of the soft tissue (mass of muscle) and the bevel angle of the needle were considered. The results indicated that this assumption does not fully account for the real deflection. They concluded that it strongly suggested that there is an additional degree of freedom: a moment or a rotational force acting on the needle.

This work was very inspiring to the design of our modeling approach, which will be presented in the next chapter. Similarly, we understand that the constancy of ω could be assured if the correct input parameters (degree of freedom) were embedded in the model. However, we also assume that, actually, under realistic scenario an analytic model is never perfect and exact. Then, it is always missing some degrees of freedom and there are always input errors in the measurements or uncertainties conditions present. Therefore, keeping the core of the idea, we considered some further improvements, such as evaluating the use of different input parameters - based on experiments performed by more recent works presented in the literature. Moreover, because we expect for several error sources in the real context, we designed an adaptive approach (based on visual feedback of needle tip position) to compensate the value of the parametric quantity and increasing the model's precision. Detailed discussion will be provided further.

Analysis of the effects of needle diameter and tip asymmetry on semi-rigid needle deflection was done by (Okamura, Simone and O'Leary, 2004). *Ex-vivo* bovine liver and silicone rubber phantoms were used, while measured forces in the insertion direction were performed in experiments guided by CT fluoroscopy imaging. They confirmed that the size and shape of the needle play an important role in determining both the forces of the needle insertion and the amount of needle deformation. In addition, they concluded that smaller needle diameters lead to less resistance force but more needle bending. Moreover, the use of beveled needles also results in more bending when compared to cone and triangular (diamond) tips.

The needle velocity effects and angle of the bevel tip were analyzed on insertions of semi-rigid needle into relatively stiff phantom in (Webster III, Memisevic and Okamura, 2005). Experiments used force/torque sensing, horizontal needle insertion, stereo image acquisition and controlled actuation of needle translation and (spin) rotation. Their results showed that the bevel angles and needle deflection have inverse relationship. Moreover, the results showed that the bevel angle have little impact on the amount of axial force. In addition, needle steering inside tissue does not depend on insertion velocity, but does depend on bevel tip angle. They also observed that the velocity of the needle insertion changes the amount of axial force, but without significant effect on the amount of needle deflection. Finally, forces acting on the needle are directly related to the insertion velocity.

The study presented by (Misra et al., 2008) evaluated the effect of needle shape and tissue material on tip forces and deflection of flexible needle (nitinol). Experimental results on phantom and real tissues aimed to obtain their elasticity and toughness parameters. These tissue properties were

incorporated in a finite element simulation to show the relationship between needle bevel angle and the forces generated at the tip. The interaction of the needle tip deforming and rupturing tissue has been modeled with both contact and cohesive zone models. Forces actuating in the needle tip were observed to be sensitive to the rupture toughness. They also observed that bevel angles have inverse relation with axial and transverse tip forces.

The energy-based model proposed by Misra (Misra et al., 2009) (Misra et al., 2010), is also an example of mechanics-based formulation that incorporates tissue-specific parameters such as rupture toughness, nonlinear material elasticity, interaction stiffness and needle geometric and material properties (Fig. 2.4).

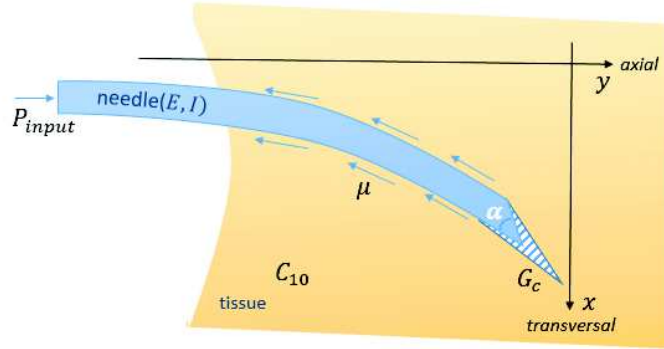


Figure 2.4 - Schematic of a bevelled needle interacting with soft elastic medium. The 2D model incorporates tip forces generated by rupture toughness (G_C), coefficient of friction (μ), toughness (G_C), nonlinear elasticity (C_{10}) and needle properties: bevel angle (α) and flexural rigidity (EI): Young's modulus (E) and second moment of inertia (I). Adapted from: (Misra et al., 2009)

The model was guided by microscopic and macroscopic experiments. The functional form for the deflection of the flexible (nitinol) needle in an elastic medium was initially assumed and the Rayleigh-Ritz (RR) approach was used to evaluate the coefficients of the deflection equation. The RR method is a variational method in which the minimum of a potential defined by the sum of the total energy and work done by the system are calculated. The system potential (Λ), of a needle interacting with an elastic medium, is given by

$$\Lambda = \underbrace{(N_E + S_E)}_{\text{energy}} + \underbrace{(-W_Q - W_P - W_R)}_{\text{work}} + \underbrace{(P_{input} l_i)}_{\text{input work}}, \quad (2.2)$$

where N_E and S_E are the energies associated with needle bending and needle-tissue interaction, respectively, and W_Q and W_P are the work due to transverse and axial bevel tip loads, respectively, and W_R is the work done to rupture the tissue. Finally, P_{input} is the applied needle insertion force and l_i , the length of the needle. Explicit expressions for each of the terms in (2.2) are provided. Needle length was discretized into segments in order to minimize the total energy and work done in the system. As result, the 2D mechanics-based model allowed prediction of deflection and radius of curvature of a bevelled needle inserted through a soft elastic medium. Simulation results followed similar trends (deflection and radius of curvature) to those observed in experimental studies of a robot-driven needle interacting with different kinds of gels. The model was limited to studies into 2D planes and future works were still to be prepared to investigate extension of the model including an energy term to represent friction dissipation. However, these results contribute to a mechanics-based model of robotic needle steering, extending previous work on kinematic models.

From this work, it is possible to deduce that the energy stored in the system due to interaction of the tissue along to the needle shaft (U_T) is very small for short insertions (Fig. 2.5). Finally, they also showed that the sum of the energy associated to the bending due to axial load (U_P) and compression of the elastic medium at the needle tip (U_C) are related to less than 0.1% of the total energy stored in the system, regardless of the insertion depth. (U_B) is energy due to pure (transversal) needle bending. In

the next chapter, we will show how the approximations of our needle deflection model, concerning to the friction and cutting forces, are in accord to the Misra’s observations, as presented above.

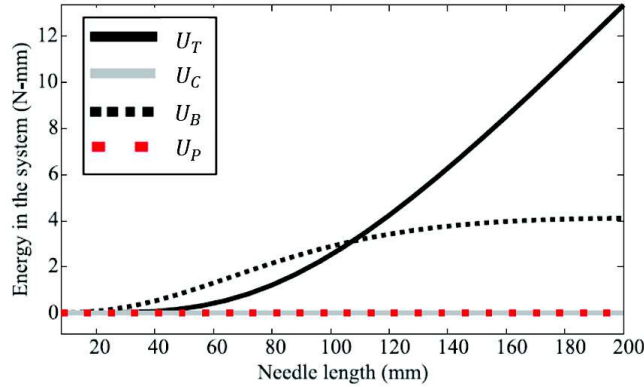


Figure 2.5 - Contribution of various components of the system energy during needle insertion experiments. Source: (Misra et al., 2009).

2.2.2 Kinematic models

Kinematics is a branch of classical mechanics concerned with the motion of objects without reference to the forces that cause the motion. The kinematic model has no reference to mass or force. Its only concern is the relative positions and their changes so that trajectories can be abstracted into purely mathematical expressions (Bernardes, 2012).

The kinematic bicycle and unicycle models of Webster (Webster III et al., 2004) (Webster III et al., 2006) for beveled needles considers the needle to be a nonholonomic system: The needle path cannot slide sideways and, consequently, its mobility is restricted by the pure insertion. Systems with this kind of movement are characterized by constraint equations involving the time derivatives of the system configuration variables. Therefore, representation of the tip motion in such systems, can accurately describe the entire needle shape. In fact, it has been shown that if the needle is significantly more flexible than the tissue (*e.g.*, nitinol needle and Plastisol or chicken breast tissues), its shaft follows the trajectory of the tip almost exactly (Webster III, Memisevic and Okamura, 2005). Insertion speed and (spin) rotation speed are modeled as inputs to a kinematic nonholonomic system and compliance steer while traveling on a smooth path of radius $r = \frac{1}{K}$.

The variation of the standard kinematic bicycle model, with constant yaw front wheel (α) and longitudinal base (ℓ_1) is proposed to specify the curvature K , of the needle path, while a second parameter (ℓ_2), determines the location along the bicycle that is attached to the needle tip, n (Fig. 2.6).

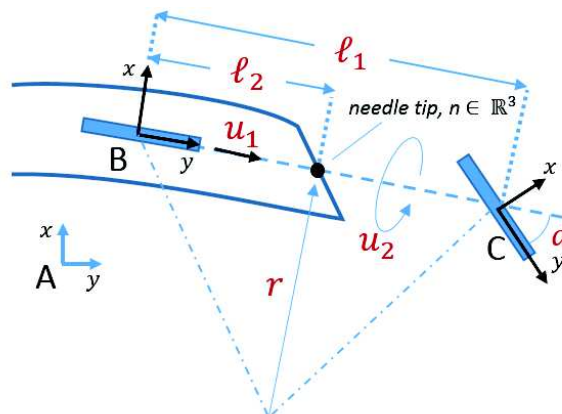


Figure 2.6 - Configuration of a bevel tip needle during steering showing the front and back “wheels” at frames B and C of a superimposed bicycle-like nonholonomic model. This particular configuration presents the z-axes for all three frames pointing into the page. Adapted from (Webster III et al., 2004).

The two-parameter bicycle model can be reduced to a one-parameter “unicycle” model (a single wheel located directly at the needle tip) by appropriate simplifications that remove ℓ_2 while retaining K . The unicycle model has a single no-slip constraint in the plane. As shown in Fig. 2.7, this constraint is $v_y = 0$ when written in body frame coordinates.

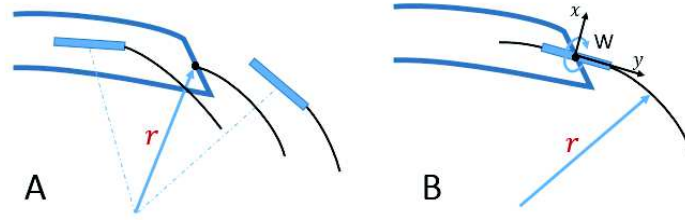


Figure 2.7 - A. Planar bicycle model. Needle rotates as a rigid body about a center of rotation defined by the intersection of the two wheel axes constraints. B. Planar unicycle model with a single no-slip constraint in the plain. Adapted from (Webster III et al., 2006).

The kinematical model considers the reference frame attached to the needle tip with local x -axis being the axis orthogonal to the direction of infinitesimal motion induced by the bevel (*i.e.*, the needle bends in the instantaneous x - y plane) (Fig. 2.8).

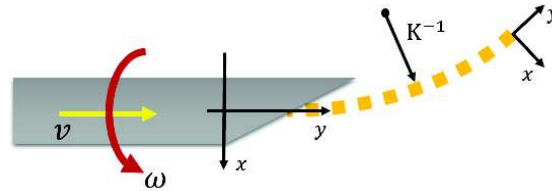


Figure 2.8 - System of coordinates and inputs of the bevelled needle kinematic model. When pushed forward, the steerable needle bends in the direction of its bevelled tip, following an arc of approximately constant radius r . Adapted from (Park, Want and Chirikjian, 2010)

The nonholonomic model for the evolution of the frame at the needle tip, based on the unicycle model can be mathematically expressed as

$$\xi(t) = (g^{-1}(t)\dot{g}(t))^V = [Kv(t) \ 0 \ \omega(t) \ 0 \ 0 \ v(t)]^T, \quad (2.3)$$

where $g(t)$ is the Euclidean motion group, $SE(3)$, which represents rigid-body motions in 3D space and ξ is the element of $SE(3)$, which is the Lie algebra (introduced to study the concept of infinitesimal transformations) associated with $SE(3)$. $SE(3)$ can be identified with \mathbb{R}^6 in the usual way via the mappings $(\)^V : SE(3) \rightarrow \mathbb{R}^6$ (Park, Want and Chirikjian, 2010).





Simultaneous rotation (ω) and insertion (v) velocities, when combined, can move the needle in the three-dimensional space. The Table 2.1 shows different paths that can be achieved depending on the combination of insertion and rotation velocities employed.

Helical path in the 3D space (Duindam et al., 2008) (Hauser et al., 2009) is followed by the needle when constant ω and v are applied simultaneously. Instead, in the stop-and-turn insertion technique, ω and v are performed one at a time. In the case of simultaneous insertion and rotation with ω being relatively larger than v , the 3D helix tends to a straight line. The duty-cycling technique (Engh et al., 2006) explores such idea to achieve different curvature values.

It is interesting to note that the bevel steering approach does not preclude linear paths for the needle. The needle may be inserted along an approximately straight path by continually rotating it at the base as it is inserted - effectively using a “drilling” motion (Webster III et al., 2006). When it is done, the models predict a helical needle trajectory with extremely small radius that approximates a line.

The work presented by (Bernardes, 2012) considered using duty-cycling technique to the development of a planning module for robot-assisted needle steering. They proposed to remove the constant turning radius constraint present in the stop-and-turn technique. It was replaced by a lower-bound constraint in order to reach points that belong to arcs of any curvature ranging from 0 to K_{\max} . The approach was proposed to increase the amount of path possibilities and consequently allowing faster planning. In order to overcome the work-in-plane limitation, they proposed to steer the flexible needle along a 3D trajectory composed from a succession of 2D planar arcs, using a RRT algorithm that pre-computes from the current arcs with their relative orientation. The spin rotation technique allowed re-orientating the bevel-tip nitinol needle in the new planned working plane before applying duty cycling technique.

Table 2.1 - Relation between insertion (v) and rotational (ω) velocities and the correspondent trajectories achieved. Source: (Bernardes, 2012).

	Motion	Input
	Helix	$v > 0 ; \omega \neq 0$
	Arc	$v > 0 ; \omega = 0$
	Direction change	$v = 0 ; \omega \neq 0$
	Straight line	$v > 0 ; \omega \gg 0$

Duty-cycling approach for 3D needle steering was recently implemented by (Krupa, 2014), using bevel-tip flexible needle into percutaneous procedures. The 3-DoF control strategy was devised with advantages over existent methods, such as: a) it does not rely on a trajectory planning. Rather, it opens numerous closed-loop control scheme possibilities, as for example, the implementation of the visual servoing framework based on the task function approach; b) it does not constraint the needle to follow a succession of planar arcs. Rather than this, it allows non-planar 3D trajectories. The approach illustrate an example of approach that can steers the needle to reach a 3D target without relying like other methods on a path planning that uses 3D trajectory, usually composed from limited arcs-based planar bending.

Stop-and-turn technique was used by (Moreira and Misra, 2014) to steer a nitinol (flexible) needle in multi-layer phantom and biological tissues. They were focused to solve the problem of definition of the maximum needle curvature (which has been estimated by performing prior insertions). They developed an US-guided 3D needle steering system that provided combination of online and offline needle curvature estimation. Their approach was able to estimate the maximum needle curvature without performing prior insertions. Needle curvature and Young's modulus were correlated by fitting a power function using previous experimental data. Nonholonomic kinematic model such as defined by (Webster III et al., 2006) was then, combined with biomechanical parameters provided by the customized power function. An indirect feed forward Kalman filter is used to fuse offline and online estimations. The average targeting errors ranges were reported to be between 0.42 ± 0.17 and 1.63 ± 0.29 mm. Despite the validation of the curvature estimation algorithm, the Kalman filter (with the fitted power function) would have to be (re)tuned in order to guarantee that changes in the needle curvature be tracked by the online estimation - especially when running into scenario with different biomechanical characteristics, such as *in vivo* insertions. Another work developed previously by (Wan et al., 2005), tested the relationship between needle deflection and insertion depth, using methods as a) constant orientation, b) constant rotation and c) constant rotation and orientation reversal at half of insertion depth. They used 3D ultrasound guidance to insert brachytherapy needle into chicken tissue phantoms. A 3D principal component analysis was performed to obtain the population distribution of needle tip and seed position relative to the target positions. Insertions were in the average of 6 cm depth without important deflection observed in the 18-gauge 20 cm brachytherapy needle. The obtained targeting errors were respectively a) 2.8mm, b) 0.8 mm and c) 1.2 mm.

Steering of flexible needles based on axial/spin rotational techniques such as helical or duty-cycling rotations has been subject of discussion concerning to patient safety (Seifabadi, Iordachita and Fichtinger, 2012). Moreover, it cannot be used in several cases (*e.g.*, RFA – radiofrequency ablations of kidney tumors) because of needle stiffness (RFA needles are not so flexible when compared with nitinol needles). Therefore, it is important to make a correct analysis of needle deformation and set the appropriate conditions which puncture occurs, taking into account aspects such as safety and restrictions conditions imposed by the application scenario.

2.2.3 Phenomenological models

Rather than purely mechanical or kinematical analysis, phenomenological models have been used to fit data obtained with experiments to parametric models. Such models are based in phenomenological observations of needle and tissue interactions. They were primarily designed to enable real time use. Even though accurate physics is not deemed a priority in phenomenological models, the results presented in the literature have demonstrated that they are able to capture needle-tissue behavior with sufficient accuracy to be used in planning and control (Bernardes, 2012).

The deflection model developed in this thesis belongs to this class of solutions. The phenomena involving the forces structures present in the system are observed into a systematic study using virtual springs. Model's development concerns to the use of biomechanical parameters, such as needle-tissue stiffness, but also takes into account kinematics-based information, such as target and needle tip position. Moreover, its design was originally founded on empirical observations of the (axial-transversal) slope phenomenon and its behavior in the relationship involving all those parameters along the experiments. It will be discussed in details in the next chapter.

Experiments results presented in (Abolhassani and Patel, 2006) (Roesthuis et al., 2011) evaluated beam deflection phenomenon modeled in the context of needle deflections predictions. Euler-Bernoulli cantilever beam theory was designed considering both: a) beam with free end load; and b) beam supported by springs having needle-tissue interaction stiffness (Fig. 2.9). The deflection models were developed aiming to be integrated in further applications of needle path planning and steering. For the first case (Abolhassani and Patel, 2006), the needle is modelled as a flexible beam with clamped support at one end, being its deflection estimated using online force/moment measurements at the needle base. The needle deflection compensation is performed by axial needle rotation through 180° . The friction force was found to be dependent on the insertion velocity and it was determined for needle inserted under controlled velocities. Errors were found to reach 2.3 mm into nonhomogeneous tissue. The model's design did not consider tissue's stiffness during the experiments and neither considered any adaptive device to correct such approximation. Therefore, the experiment results may not be invariant to changes in the tissue's properties, while potential over fit to the experimental conditions might not work under different scenarios. Further work integrated tissue's properties in the beam model (Roesthuis et al., 2011). However, the best results found were restricted to a very short range of nominal value of tissue stiffness.

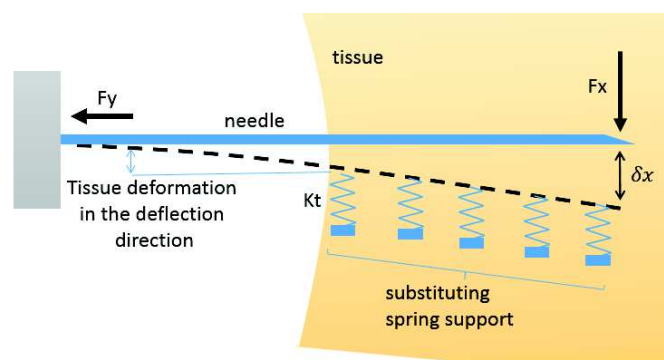


Figure 2.9 - Needle devised as a cantilever beam support by springs. Adapted from (Abolhassani & Patel, 2006).

When the needle is stiff relative to the tissue (e.g., rigid or semi-rigid needles), lateral motions in the needle base (outside the tissue) can be considered. The movement is very similar to the one classically used to steer the needle in the clinical routine (i.e., manual needle insertions). The use of lateral needle motions outside the tissue were first devised by (DiMaio and Salcudean, 2003) and (Glozman and Shoham, 2007) in order to guide the needle through insertion into soft tissue. In the first work, DiMaio (DiMaio and Salcudean, 2003) (DiMaio and Salcudean, 2005) proposed a method to predict needle motion, whose insertion was formulated as a trajectory planning and control problem.

The approach involves numerically calculating the tissue Jacobian which is the matrix that relates the derivatives of needle base and needle tip configurations, as depicted in Fig. 2.10. Using this relation, the tip velocities can be determined from the velocity of the needle base, and consequently, one may obtain the current needle tip position. Simulation results obtained presented variations of the numerical needle insertion models were in the range of nearly 1mm to 2.5mm.

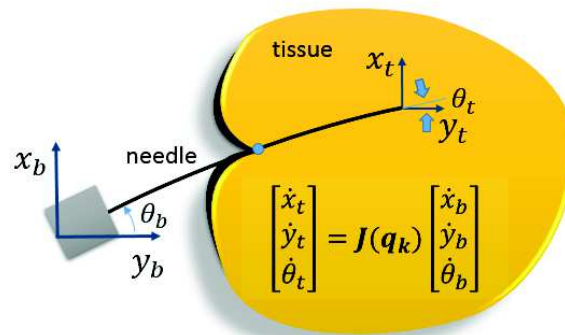


Figure 2.10 - Motion of the needle tip with respect to the motion applied to the base determines needle steerability. The tissue Jacobian matrix $J(q)$ depends on the current needle tip configuration given by $q = [x_{tip} \ y_{tip} \ z_{tip}]^T$. Adapted from (DiMaio and Salcudean, 2005).

The kinematic model designed in (Glozman and Shoham, 2007) is derived by assuming the semi-rigid needle as a linear beam supported by virtual springs, in which the stiffness coefficients of the springs can vary along the needle. In this approach, the needle is subjected to point forces applied by the deformed tissue and modeled as virtual springs. Based on assumptions of quasi-static motion and that linear lateral force respond for small displacements, tissue forces on the needle are modeled as a combination of lateral virtual springs distributed along the needle curve plus friction forces tangent to the needle. No physical meaning is attributed to the free length of the virtual springs. The only important parameter of a spring is the local stiffness coefficient that expresses the force of the tissue on the needle as a function of local displacement. The concept is illustrated in Fig. 2.11.

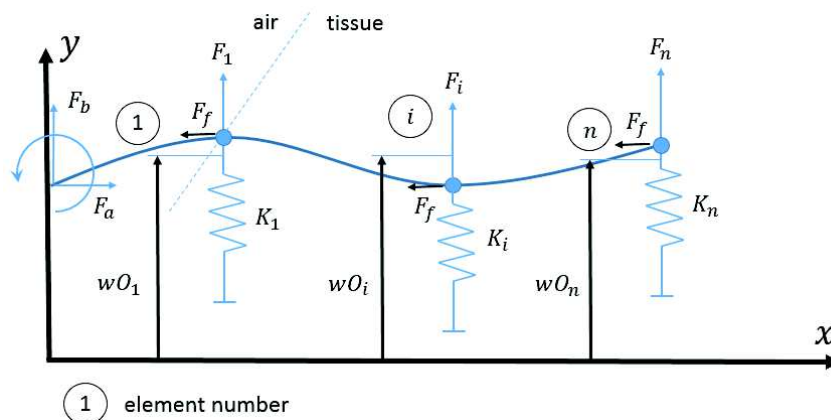


Figure 2.11 - Linear system model. Flexible beam subjected to a number of virtual springs. F_a and F_b are axial and lateral forces at the needle base. F_f is the friction force, wO_i is displacement at point i . K_i is the virtual spring coefficient and F_i is the force applied by a virtual spring at each joint. (Glozman and Shoham, 2007)

The linear beam is subjected to point forces and with appropriate spacing of elements, it can approximate a flexible beam according to the elastic foundation model. At each joint, the force applied by a virtual spring is proportional to the displacement of the spring from its initial position. The linear system model splits the beam into a number of elements, in which the first element is the part of the needle outside of the tissue and each element behaves as a linear beam subjected to shearing forces at its borders. Forward and inverse kinematics of the needle were solved analytically, providing adaptive corrections for real-time (RT) fluoroscopic guidance. The 2D approach was validated using stainless 20G needles, along 40-mm trajectory reaching error around 0.5-mm, guided by X-ray imaging.

Recently, (Khadem, et al., 2015) presented an approach for real-time simulation of insertion of a semi-rigid needle into soft tissue. The model aimed to provide real-time prediction of the needle deflection, useful to support procedures under low-resolution ultrasound images. In addition, it could be utilized for preoperative motion planning and optimized trajectory design in brachytherapy applications. The model is based on the Euler-Bernoulli beam theory with transversal distributed loads. Beam theory was extended such that insertion velocity is used as input to robotic-assisted needle steering. The model also takes into account parameters as tissue deformation, needle-tissue friction, tissue cutting force and needle bevel angle. Cutting and friction forces in two different phases and estimated directly from the forces sensor measurements. The root-mean-squared error of the model in predicting tip position was of 0.38 mm considering a single phantom using synthetic material. The approach considers in-plane axial bending of the needle and parameters of tissue (e.g., stiffness) along the insertion depth is not taken into account.

2.3. Toward fundamental numerical-based solutions

In most cases the mathematical model is sufficiently complicated to make the exact analytic solution very difficult or impossible. Numerical-based models are mathematical models that often use some sort of numerical time-stepping procedure to obtain the models behavior over time.

Numerical solutions have several advantages over analytical solutions. For example, the precision can be greatly improved for a given time step and equations are usually much more intuitive than the complicated mathematics often involving analytics solutions. However, a drawback of using numerical solutions to solve model equations is that they need many iterative calculations to get good results. Therefore, fast computer speeds must be used to perform the thousands of repetitive calculations involved. Rather than an equation, the result is a long list of numbers that can be used in simulations.

2.3.1 “Tissue-numerical” approaches

The puncture conditions, such as the force applied to the needle, are difficult to be decided deterministically, because the experimental data of puncture conditions have variations. Rather than assist needle insertion by estimating needle deflection, the work in (Kobayashi et al., 2009) considered the insertion of a rigid (straight) needle into a FEM-based viscoelastic and nonlinear deformable model of the liver, as well as a probability-based model of puncture conditions, evaluating the expected value of needle placement accuracy (Fig. 2.12).

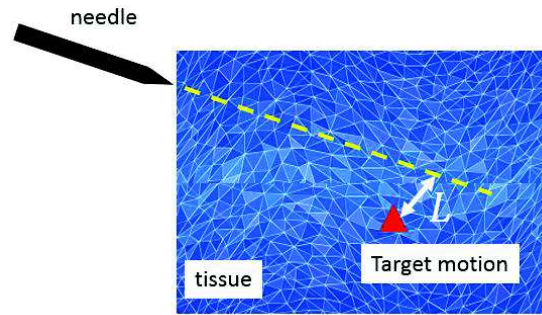


Figure 2.12 - Comparative distance (L) between insertion line and target position.
Adapted from (Kobayashi et al., 2009).

They assumed a percutaneous therapy scenario where the needle path is limited to a straight line because the constraints imposed by the abdominal wall. A numerical simulation and evaluation of their approach was performed using a liver-shaped 2D model. Their purpose was to develop a novel planning method to decide robust paths for insertion of rigid needle, considering various puncture points. Experiments measuring needle placement accuracy showed that the method placed the needle with a mean accuracy of 1.5 mm.

Some research groups have also conducted studies in order to find the optimized insertion point and orientation using linear and nonlinear models (Dehghan and Salcudean, 2007) (Goksel et al., 2005). Dehghan proposed an iterative optimization method to optimize the needle insertion entry point, heading and depth for needle insertion, while minimizing the distance between a number of specified targets and the needle. The deformable tissue is described by a Finite Element Method (FEM) while the neo-Hookean material model is exploited to determine the effects of geometric and mechanical nonlinearities and compressibility effects. The simulation-based optimization algorithm is shown converging in few iterations and decreasing the targeting error effectively under the prostate brachytherapy simulator. However, the use of non-linear models is computationally expensive.

The approach developed in (Goksel et al., 2005) run comparatively faster using a linear model in the brachytherapy simulator using prostate mesh with conforming anatomical boundaries. They extended a FEM-based algorithm, while proposing 3D mesh's nodes reposition and addition as methods for achieving needle-tissue coupling. They claimed to be the first physically-based 3D interaction model of a semi-rigid needle insertion into a soft body. By using the Woodbury formula (matrix inversion lemma), the simulation was able to run faster than 1kHz.

Later, (Goksel, Dehghan, & Salcudean, 2009) they presented three different models to simulate deformations of a needle, in order to improve needle targeting. Geometric nonlinearity was taken into account for the two first models. They were based on finite element method using respectively tetrahedral and nonlinear beam elements to identify Young's modulus. The third approach was modeled as a series of rigid bars connected by angular springs. Lateral forces were applied in the needle base in order to steer the needle. Measurements of such forces and the consequent needle shaft deflection were recorded and compared to simulation results. The angular spring model was the most accurate in modeling as well as computationally the most efficient model during the simulations.

An interactive simulation of semi-rigid needle insertions is presented in (Duriez, Guébert, Marchal, Cotin, & Grisoni, 2009). Needle-tissue interactions are reproduced using a set of dedicated complementarity constraints for physical phenomena such as, puncture, cutting, static and dynamic friction at interactive frame rate. Experimental data is used to provide realistic parametrical inputs to the simulation. The modeling method allows for the 3D simulation and take into account insertions through different tissue layers, as well as parameters as Young Modulus, poisson ratio and area of the cross section of the semi-rigid needle. Simulation results are presented to be close to previous works in the literature, while more realistic constitutive laws for the tissue deformation and validations experiments are proposed as future works. Recently, (Moreira, et al., 2013) implemented SOFA (Simulation Open Framework Architecture) simulations compared with experimental results for tissue indentation and needle insertion. Experimental phantom was built using MR images and tissue

properties were obtained from ultrasound-based Acoustic Radiation Force Impulse imaging technique. Markers were placed on the tissue-surface to identify the indentation, while needle tip position was used to validate the model during the experiments. They've obtained mean square error of 0.36mm for prostate indentation experiments and 0.14mm for semi-rigid needle insertion simulations. Despite the work demonstrating the efficacy of SOFA for surgical simulations and preoperative planning, constraints regarding to computation efficiency imposed by intraoperative needle insertion predictions or planning could difficult the application of such tool into the clinical context.

2.3.2 Stochastic modeling

A stochastic differential equation (SDE) is a differential equation in which one or more of the terms is a stochastic process, resulting in a solution that is itself a stochastic process. SDEs are used to model diverse phenomena into physical systems subject to parametrical input fluctuations. Numerical solution of stochastic differential equations and especially stochastic partial differential equations is a young field, relatively speaking. According to (Vajargah and Asghari, 2014), almost all the algorithms that are used for the solution of ordinary differential equations will work very poorly for SDE's, having very poor numerical convergence.

We discussed above how bicycle and unicycle kinematics-based models can describe the deflection motion of the needle. However, there is inherently variation between insertions (Cowan et al., 2011). Under idealistic scenario, motion $g(t)$ of the flexible needle, obtained by simply integrating ordinary differential equation in (2.3) - Section 2.2.2, would be exact and certain. However, repeatedly insertions of a needle into soft medium such as gelatin - used to simulate soft tissue (Webster III et al., 2006) - will demonstrate an ensemble of slightly different trajectories.

According to (Park, Want and Chirikjian, 2010), a simple stochastic model for the needle is obtained by adding noise to the two input parameters in the ideal model:

$$\omega(t) = \omega_0(t) + \lambda_1 w_1(t), \text{ and } \nu(t) = \nu_0(t) + \lambda_2 w_2(t).$$

Being $\omega_0(t)$ and $\nu_0(t)$ the inputs in the ideal case, $w_i(t)$ are uncorrelated unit Gaussian white noises, and λ_i are constants. Thus, a nonholonomic needle model with noise is

$$(g^{-1}\dot{g})^V dt = [K \ 0 \ \omega_0(t) \ 0 \ 0 \ \nu_0(t)]^T dt + \begin{bmatrix} 0 & 0 & \lambda_1 & 0 & 0 & 0 \\ 0 & 0 & 0 & 0 & 0 & \lambda_2 \end{bmatrix}^T \begin{bmatrix} dW_1 \\ dW_2 \end{bmatrix}, \quad (2.4)$$

where $dW_1 = W_1(t + dt) - W_1(t) = w_1(t)dt$ are the non-differentiable increments of a Wiener process $W_i(t)$. This noise model is a stochastic differential equation (SDE) on SE(3), whose shorthand can be written as

$$(g^{-1}\dot{g})^V dt = h(t)dt + HdW(t). \quad (2.5)$$

2.4. Conclusion

This chapter introduced the latest results in the literature in modeling the needle-tissue behavior during percutaneous insertions. More specifically, a short review on the main approaches for modeling beveled needle interaction with soft tissue has been presented.

In the next chapter, we will justify the choice of developing a novel deflection model in the context of the proposed robot-assisted system. We will introduce the conceptual basis of a novel needle deflection model, proposed as the core of the robot-driven needle insertion system developed in this thesis. The model was designed using observations obtained from preliminary needle insertion experiments using LPR into CT environment. The main aspects of such modeling are discussed in detail below.

Chapter 3.

The Adaptive Slope Model

The submillimeter targeting error results from most of the experiments presented above serve to validate their proposed methodologies. In despite of this, the main challenges for the use of robot-assisted needle insertion approaches go beyond the targeting error quantifications. It is important to mention that methods discussed in several of these works cannot be directly applied under the ARCS context. According to the mentioned previously, concerns related to patient safety, compatibility issues due to the use of semi-rigid needles under nonholonomic approaches are also associated to the current unavailability of mechanical (spin) rotation movements of the needle under ARCS-compatible robot platforms. Finally, the online deflection predictions of most of these models may be conditioned to the previous integration of special non-metallic force sensors into the MRI-guided platform. The issues mentioned above limit or make difficult the use of many of these models under ARCS. The approach presented in this chapter has the potential to fill this blank. We will present below the conceptual basis of the adaptive slope model designed to predict needle tip deflections into ARCS-based percutaneous procedures. The model is conceived as the core and foundation of all the application techniques devised in this thesis to support percutaneous needle insertion. Next, we describe experiments using the LPR robot, which allowed us to obtain preliminary observations. Such observations were crucial to the modeling design and training based on empirical data.

3.1. Conceptual basis

We present now the modeling of percutaneous insertions of a semi-rigid needle (N) interacting with soft medium. The modeling is performed as a function of kinematic-based parameters (δy_i and needle tip position N_i), biomechanical properties (stiffness) of the needle (Kn) and tissue (Kt), as well as geometric-based study, including the needle tip asymmetry (α).

Kinematical modeling: The insertions are assumed to be performed progressively, with quasi-static motions and intermediate insertion depth (δy_i) concerning to the iterative time (i). The needle path is modeled as articulated links, being θ the deflection angle between two respective links. The length of each link depends on the insertion depth (δy_i). The needle entry point (E) is assumed to be fixed in this work.

For each δy_i , the model aims to predict the concerned δx_i , defined as the deflection of the needle tip orthogonal to the insertion direction. Let $\widehat{\delta x_i}$ be predicted value of δx_i . This means that we are interested in our modeling only to the needle position prediction N_i at step i and not to the in-between steps predicted needle trajectory.

The Adaptive Slope Model

The semi-rigid needle is considered as a beveled cylinder whose biomechanical stiffness property is calculated according to (Glozman and Shoham, 2007):

$$Kn = 3EI/L^3. \quad (3.1)$$

Being (EI) the flexural rigidity: Young's modulus (E) and second moment of inertia (I). The parameter E is sensitive to the needle's material (e.g., stainless (316) steel exhibits 193-GPa Young's modulus), while the second moment of inertia of a cylinder relates outer diameter d_o and inner diameter d_i , according to:

$$I = \frac{\pi}{64}(d_o^4 - d_i^4). \quad (3.2)$$

$\mathcal{L} = (\mathcal{L}_{out} + \mathcal{L}_{in})$ is the needle length, defined as the distance between the points concerning to the positions of robot's end-effector, referred here as 'base' (B) and the needle tip (N_i), projected along the y -axis. Where, \mathcal{L}_{out} concerns to the region of the needle outside the soft tissue, while \mathcal{L}_{in} is the needle length inside the tissue. It is important to note that along the insertion, the LPR's architecture leads to a dynamic value of \mathcal{L} , and by consequence, Kn . It happens when the (gripper-based) end-effector presents a constant value for \mathcal{L}_{out} along the insertion. This is the case for the LPR robot. As consequence, needle is progressively *delivered* to the system, according to the insertion steps (δy_i). We say delivered because for each δy_i , it leads to sequential increases in the length of the needle's shaft actually present in the system. In contrast to that, \mathcal{L} could be constant along δy , if we consider the use of other robotic systems, in which the proximal base of the needle is attached to the end effector (\mathcal{L}_{out} dynamic). In this case, \mathcal{L} would be constant because the needle is fully present in the system from the beginning. The effects of \mathcal{L} 's definition over system's behavior will be discussed in details in the end of this thesis.

For sake of simplicity, the experiments performed in this work considered tissue stiffness (Kt) constant along the insertion (i.e., homogeneous tissue), according to the measurements obtained in the tissue's surface. However, in the future, tissue's stiffness information regarding to the full insertion depth could be preoperatively obtained by using MR or Acoustic-based elastography (Moreira and Misra, 2014). In such cases, the iterative model could receive the tissue's stiffness (Kt_i), updated for each sequential (δy_i). It could be done without further modifications in the model's design, as proposed bellow. In addition, for the model development, the needle is considered to move only in a two-dimensional plane, defined by the image slice. However, it could be easily extended to 3D scenarios, if we consider that the needle moves out of this 2D plan, as it has been implemented in Chapter 4.

The semi-rigid needle is assumed to perform deflections according to the small-deflection beam theory ($\delta x/\mathcal{L} < 0.1$) (Timoshenko and Gere, 1972) in the direction of the bevel due to the asymmetric forces acting on the needle tip. As consequence, the needle deflection angle (θ), is considered in the limit of its approximation to zero, according to the small-angle approximation, in which ($\sin \theta \approx \theta$) (Fig. 3.1).

Let L_i be the point concerning to the linear projection (extrapolation) of the segment defined by the two last measured needle's positions N_{i-1} and N_i (see Fig 3.1). I.e.: The point L_0 refers to the linear projection of the segment BE, where E is the entry point defining the initial needle position N_0 (step $i=0$). Point L_1 is the linear projection/extrapolation of the segment defined by N_0 and N_1 , etc.

As a consequence of the small-deflection beam theory, the needle deviation orthogonal to L_i , can be approximated to the deviation orthogonal to the initial insertion direction L_0 . Therefore, ($N_i \approx N'_i$) (Fig. 3.1.III).

The Fig. 3.1 shows progressive evolution of the insertion procedure, taking into account the kinematic-based parameters, as described above. The out-of-scale illustration relates needle tip positions N_i in function of the needle insertion depth δy_i , along the iterative time i . This figure shows

how our model allows to predict, for a needle insertion depth δy_{i+1} , the next deflection $\widehat{\delta x}_{i+1}$ regarding the line L_i defined by the extrapolation of the segment $N_{i-1} N_i$.

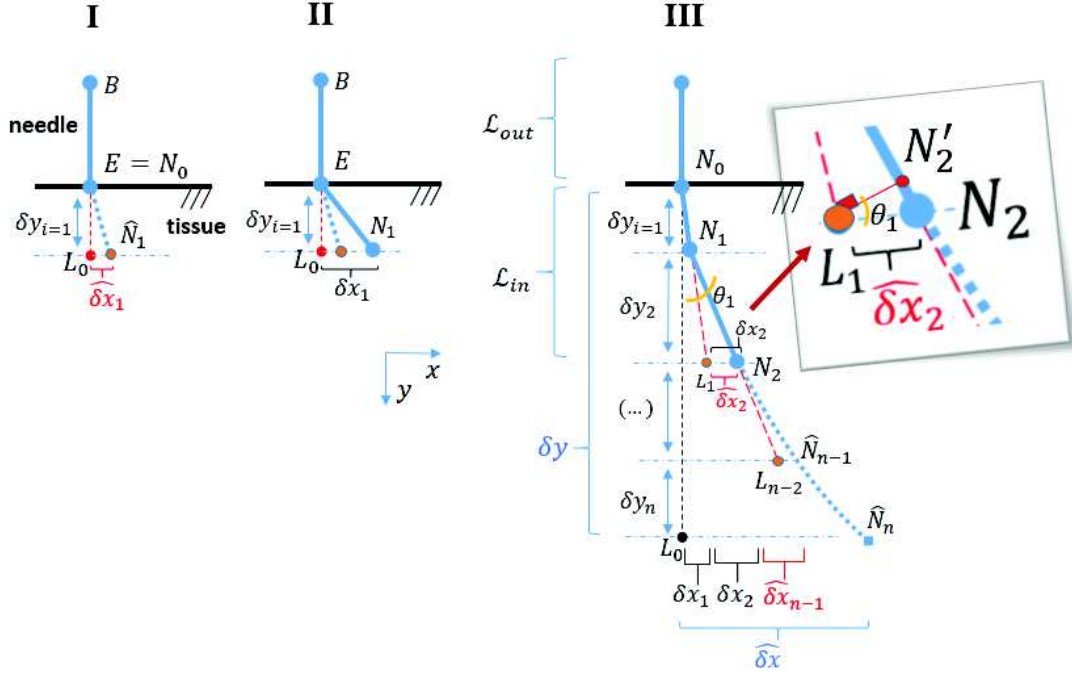


Figure 3.1 - Out of scale illustration of the iterative percutaneous procedure. The kinematics-based analysis devises needle path with deviation angle θ between the articulated links. Needle tip deflection δx_i is defined orthogonal to the insertion direction, according to L_i projected using N_{i-1} and N_i , along δy_i .

The incremental needle deflection estimation ($\widehat{\delta x}_{i+1}$) is calculated as function of a given δy_{i+1} , considering the linear projection (L_i), concerned with the two last position of the needle tip (N_{i-1} , N_i). Therefore, for each insertion step, estimated needle tip position (\widehat{N}_{i+1}) can be expressed into the moving frame attached to the current needle tip (N_i), in which the y -axis is aligned with the L_i direction.

$$\widehat{N}_{i+1}(x, y) = (\widehat{\delta x}_{i+1}, \delta y_{i+1}) \quad (3.3)$$

Indeed, as shown in Fig 3.1.I, the needle is positioned at the entry point E and has a measured position N_0 . At this step $i=0$, the predicted deflection regarding the line L_0 (*i.e.* defined by the segment BE) is given by $\widehat{\delta x}_1$. This allows to calculate the predicted needle position \widehat{N}_1 . After the first insertion step of depth δy_1 , *i.e.* the needle is at the real position N_1 , one can measure the real needle deflection δx_1 (regarding the same previous line L_0). At the next step $i = 1$ (Fig. 3.1.II), one can predict the needle position \widehat{N}_2 defined by the deflection $\widehat{\delta x}_2$ regarding the line L_1 (defined by the segment $\overline{N_0 N_1}$) while inserting the needle at a depth δy_2 . Finally, the Fig. 3.1.III shows the insertion step $i = n$ that corresponds to a full insertion depth: $\Delta y = \sum_{i=0}^n \delta y_{i+1}$ and a total needle deflection Δx regarding the initial insertion direction L_0 .

Interaction modeling: Differently from what have been presented in (Glozman & Shoham, 2007), we assume the needle as a concatenation of an articulated rigid body segments ($\overline{N_{i-1} N_i}$) where the last segments that represents the needle tip is supported by one equivalent orthogonal virtual spring of stiffness Kn attached to the needle tip (see Fig. 3.2).

Based on assumptions of quasi-static motion and that linear lateral force respond for small displacements, needle tip-tissue interaction forces can be modeled as a “slipping motion, in presence

of friction, between two rigid bodies (needle tip and an inclined plane) both attached to virtual springs". Indeed, in our work, the tissue is modeled as a rigid body (inclined plane) on which the needle is relying and will slip in presence of friction. This inclined plane is attached to two virtual springs (Kt) representing the local 2D tissue stiffness's.

The expressions derived from this phenomenological analysis concern the equilibrium of the needle during the insertion into an elastic body. They describe the relationship between the components of the resultant force (R_x) and (R_y) acting on the needle (Fig. 3.2). This equilibrium is considered to hold at the beginning of each insertion step but after tissue relaxation phase. *I.e.*, for our model validity, before each new insertion step, one has to wait for tissue relaxation ($\sim 5s$). This is currently the case in the thesis context where sequential insertion steps are considered with imaging updates between insertions.

The resultant force R represents the sum of all the forces actuating on the system, in particular the input force F and friction force $F\mu$. The analysis assumes that the resultant force's component in the x axis (R_x) is the same one needed to compress parallel virtual springs, in which stiffness of each spring is given by the needle (Kn) and tissue (Kt) stiffness. The needle axial deformation is negligible compared to the tissue deformation. Therefore, the resulting y -component (R_y) is represented by a single spring with stiffness Kt . This lead to:

$$R_x = (Kn + Kt) \delta x \quad (3.4)$$

and

$$R_y = Kt \delta y. \quad (3.5)$$

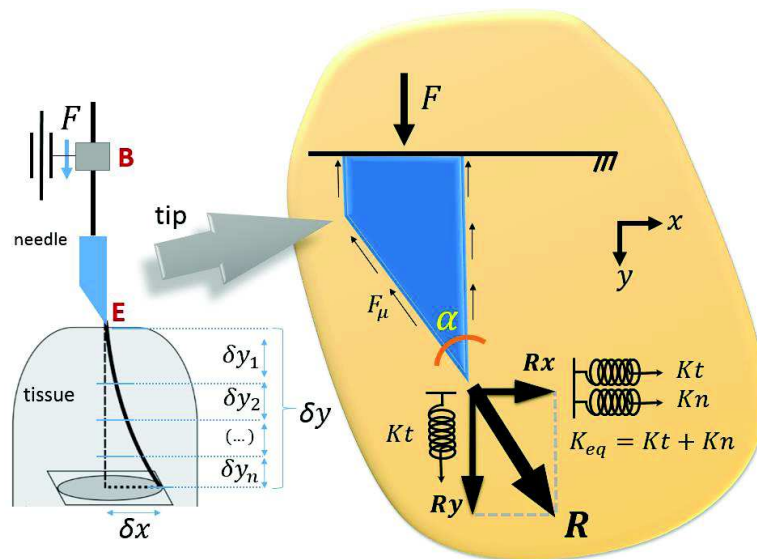


Figure 3.2 - Needle tip deflection modelling. Left: Needle deflections are assumed to be towards the direction of the bevel. Right: Components of the resultant forces.

In the relationship presented below, R_x acts transversally and causes needle deflection, while R_y is the axial force that allows needle displacement in the y axis.

The Fig. 3.3 expresses the forces relationship in terms of the angle and cone of friction. Fig. 3.3.I shows the needle tip body relying on the inclined plan where T_g and N_m are the tangential and the normal axis to the bevel tip. Since the needle is considered moving inside the tissue (thus slipping on the virtual inclined plane), one know that the resultant force R will always be located on the friction cone making an angle γ regarding the normal N_m . Friction cone defines $\tan \gamma = \mu$ (McGraw-Hill, 2003). Fig. 3.3.II shows the study of component forces related to R .

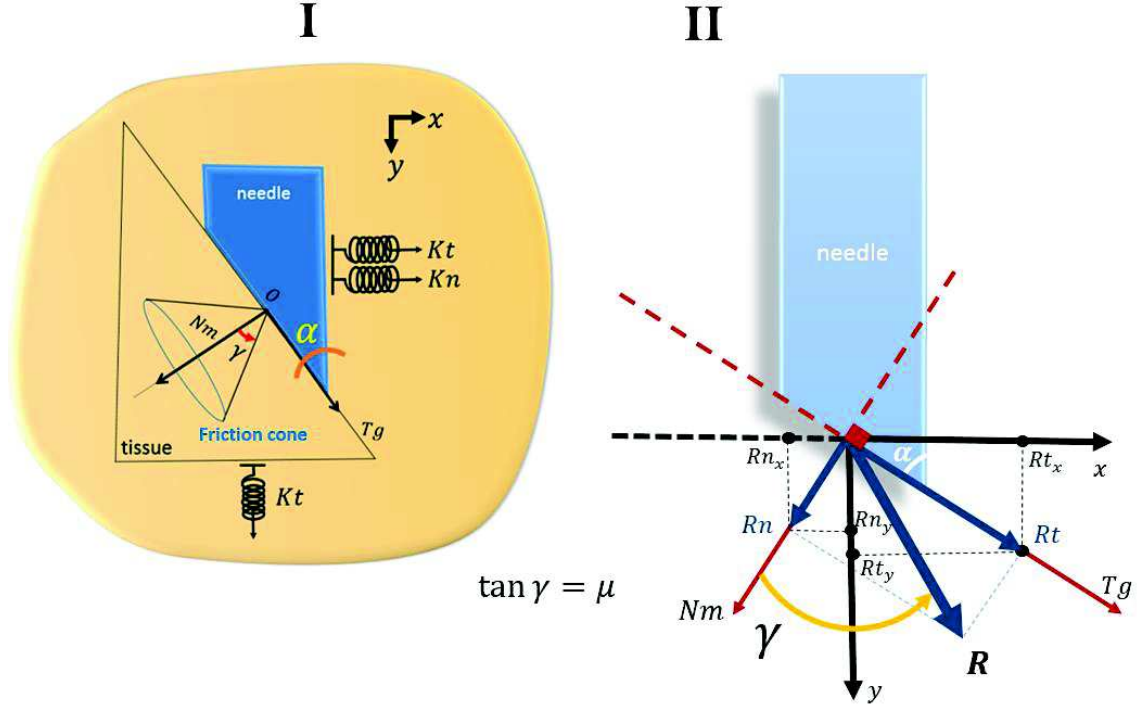


Figure 3.3 - Study of angle and friction cone in the context of needle-tissue interaction.

The projections of the tangential R_t and normal R_n components of the resultant force R in x and y -axis, in function of the friction angle γ and the needle tip angle α , give:

$$R = \begin{bmatrix} R_x \\ R_y \end{bmatrix} = \begin{bmatrix} Rt_x - Rn_x \\ Rt_y + Rn_y \end{bmatrix} = \begin{bmatrix} R \sin \gamma \sin \alpha - R \cos \gamma \cos \alpha \\ R \sin \gamma \cos \alpha + R \cos \gamma \sin \alpha \end{bmatrix} = \begin{bmatrix} R \cos(\gamma + \alpha) \\ R \sin(\gamma + \alpha) \end{bmatrix}. \quad (3.6)$$

Therefore,

$$\frac{R_x}{R_y} = \frac{\cos(\gamma + \alpha)}{\sin(\gamma + \alpha)} = \cot(\gamma + \alpha) \quad (3.7)$$

Finally, combining (3.4-3.5) with (3.8), we can estimate the needle tip deflection for the x direction as:

$$\widehat{\delta x}_{i+1} = \frac{Kt_i \delta y_{i+1} \cot(\gamma + \alpha)}{Kt_i + Kni} = \frac{Kt_i \delta y_{i+1} H_i}{Kt_i + Kni}. \quad (3.8)$$

Where $H_i = \cot(\gamma + \alpha)$ is an unknown parameter that has to be estimated experimentally and adapted online as it will be presented further.

Indeed, this adaptive parameter (H) is originally devised in function of the needle tip asymmetry α , which is known and constant, and the frictional angle γ , which is difficult to be precisely determined pre-operatively. Moreover, it is supposed to vary according to the properties of the material along the insertion depth. Therefore, we devised (H) as a dynamic parameter that is updated along the insertion, in order to correct the initial state of the system. Actually, in this case it assumes the function of a failure contingence mechanism and allows online adaptive correction regarding to model's approximations and user's parametric input errors, for example.

H_i is proposed to be updated for each insertion step, according to the current position of the needle tip N_i . The deflection prediction $\widehat{\delta x}_{i+1}$ for the insertion step δy_{i+1} is performed considering the needle tip update H_i at the time i . Therefore, applying inverse of the equation (3.4), H_i is updated for each insertion step i , according to the measured needle deflection δx_i :

$$H_i = \frac{(Kt_i + Kni) \delta x_i}{Kt_i \delta y_i}. \quad (3.9)$$

Starting from a pre-defined initial value (H_0), position-based updates of the parametrical slope (H_i) are proposed to (re)balance the component's system (3.8) according to the actual state of the scene (fiducials position). Such updates allow adaptive correction regarding to the error ($e_i = \delta x_i - \widehat{\delta x}_i$) between the needle tip deviation observed (δx_i) from the image and the predicted deviation ($\widehat{\delta x}_i$) at the insertion step i .

The definition of H_0 is central to allow offline predictions. Such value is assumed to be invariant for offline prediction, regardless of intra or inter differences of initial scenario setup, including needle and tissue changes through different experimental conditions. Of course, this assumption is idealistic and we know that the model is not perfect. Furthermore, errors are expected from several sources, that is why H_i is updated online.

As mentioned above, once H_0 is computed, the compensation of the model's approximations is performed sequentially. The position-based updates are proposed to overcome approximation errors as friction along the needle shaft, tissue's topological changes or input measurement errors.

For example, some of the experiments evaluate the behavior of the model in the special case of multi-layer tissues, for which only superficial tissue properties measurements of Kt is known. This special case could be particularly interesting when facing a future scenario of needle placement into biological or in-vivo tissues, where no elastography or force sensor input is available intraoperatively (online). Results obtained from experiments along this thesis reveal potential to overcome the initial measurement inaccuracy regarding the heterogeneity and inhomogeneity of tissue's parameters.

Heuristic technique supported the definition of H_0 . It was done using empirical data obtained from preliminary experiments. It will be described further.

Fig. 3.4 summarizes the mechanism of prediction and updates devised to support needle insertion with adaptive corrections. Updates of needle deflection δx_i are based on visual feedback of the needle tip position along the insertion of the needle through the soft tissue. Each update (H_i) at the insertion time i allows measurements of noise and other inaccuracies, as well as predictions that tend to be more precise than those based on a non-adaptive prediction.

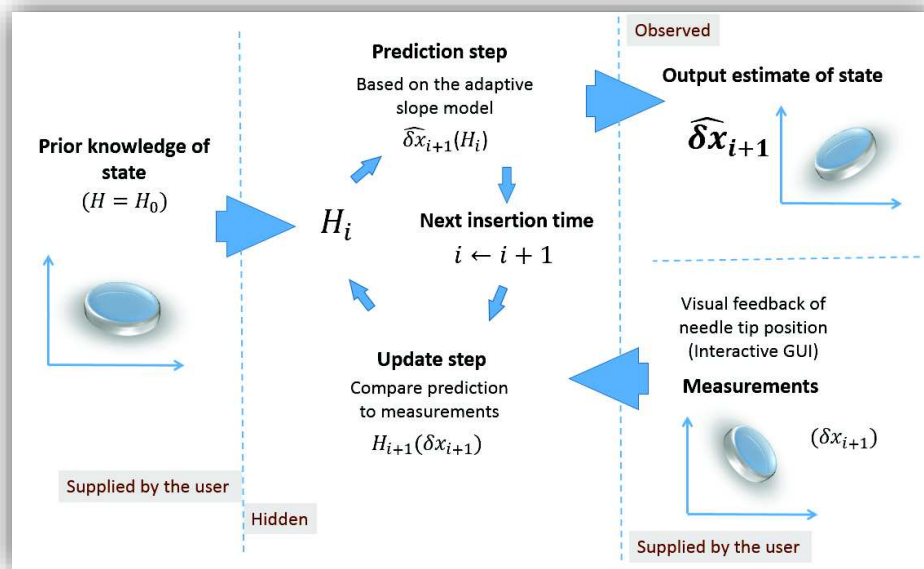


Figure 3.4 - Predictions and updates mechanism. Estimated state of the system is tracked by the needle's deflection prediction model and sequential adaptive updates. Prediction $\widehat{\delta x}_{i+1}$ is updated using inverse modelling (H_i) that absorbs scenario's uncertainties at the insertion time $i-1$, before the i -th measurement.

3.2. Preliminary observations

The adaptive slope model, described above, was developed based on observations of 3D CT images provided by preliminary needle insertion experiments using the LPR robot into PVC and *ex-vivo* pork tissues. The experiments aimed to characterize interactions during needle-tissue placements. The design and observations of this pilot study provided the bases for empirical understanding on needle tip deflection. The images and data assembled into an experiment database were fundamental for later modeling and validation of the work presented in this thesis.

The experiments were led in the CT room of the CHU-Grenoble using the Siemens CT scanner Somatom Sensation 16 (Fig. 3.5).

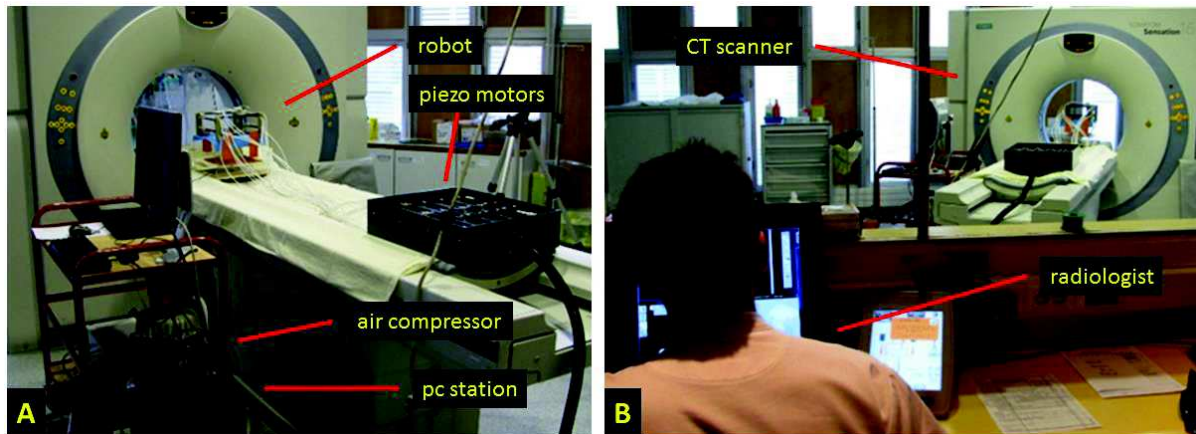


Figure 3.5 - Scenario setup using the CT scanner. A. imaging room. B. control room. Progressive images of the system were taken during needle insertion.

The robotic-driven needle interaction was performed under the constant pressure of nearly 4.5 bar. The 3D images were acquired under voxel resolution of $0.6 \times 0.3 \times 0.3$ mm and an image database with 36 CT images sequences was created (each sequence having more than 200 slices). The sequences were related to eight insertions (six in PVC and two in pork), scanned progressively by the CT scanner during insertion. The acquisition time for each sequence took nearly 4s to 5s considering images of dimension (512x512). In this pilot study, a long (20 cm) and thin (semi-rigid), 18-gauge Stainless (316), 17 degrees bevel-tip spinal needle was inserted several times without interferences in the needle trajectory. The needle was inserted vertically and also tilting 10° in different directions while interacting with elastic medium.

After the experiments, 3D reconstruction of the CT images was performed. The position of the needle tip and main points of the needle shaft were cropped manually by using the open source software 3D slicer (BWH, 2015). Fiducials of 3D needle position were manually extracted from the images along to the several needle insertion steps. Such needle position data were associated to their respective images and loaded into a database that provided major importance for the model design.

In order to better observe the forces actuating in the system, a 6-DoF force-torque sensor (nano43 / SI-36-0.5 / ATI Industrial Automation) was mounted below the phantom and was used to track the resulting forces and torques on the phantom body (Fig. 3.6.B).

A framework support was built to fix the robot using two rigid plastic walls attached to a wood base (Figure 3.6.A). The force sensor was fixed in this base, while an additional wood base was attached on the force sensor using screws (Figure 3.6.B). The tissues were placed on this rigid surface, while a surgical drape was installed in the level of the tissue surface (Fig. 3.6.C). The sheet was installed using screws in the robot's base. It was proposed to reduce the damages in the tissue surface supposing lateral movements to steer the needle tip. It will be discussed in detail further. The Fig. 3.6.D shows the robot's grippers (G1 and G2) holding the needle.

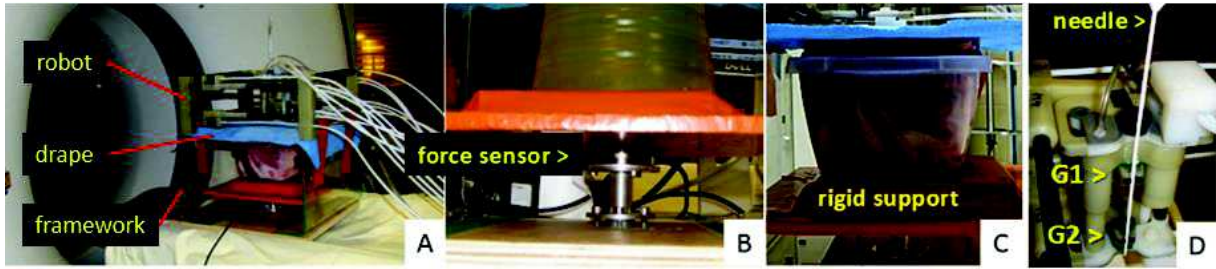


Figure 3.6 - Experiment setup. A. Customized support framework, robot and surgical drape. B. Force sensor C. Ex-vivo tissue pork. D. LPR's grippers (G1 and G2) and needle.

Two types of tissues were used as a replacement of human flesh. The first one was a homogeneous synthetic soft PVC (100x100x130mm - 100% soft plastisol) (Fig. 3.6.B) and the second was a non-homogeneous ex-vivo fresh porcine tissue (~80x80x100mm) of nearly 1.5 kg supported by a plastic canister (Fig. 3.6.C). The PVC phantom was fabricated by cooking the plastisol in low heat. In order to observe internal tissue deformation due to needle-tissue interaction, glasses seeds were added in the solution. A centrifuge was used to keep the seeds dispersed and away from the bottom of the pan while the solution was cooled in the room temperature.

3.2.1 Qualitative tissue properties measurements

The qualitative properties of the tissue (stiffness) at surface level are estimated using adaptation based on the experiment described in (Glozman and Shoham, 2007). It will be described below.

For the experiments, long (20 cm), Stainless (316) steel, 18-gauge, 17 degrees bevel-tip needle was used having an outer diameter (do) of 1.27 mm. The inner diameter (di) was set to zero because the needle actually looks like a hollow tube (cannula) inserted with the aid of a trocar (Fig. 3.7). It also avoids tissue being filled into the needle. It exhibits 193-GPa Young modulus (E) (Glozman and Shoham, 2007) and moment of inertia $I = \pi/64 * (do^4 - di^4) = 0.13 \text{ mm}^4$. As mentioned above, the needle stiffness is given by $Kn = 3EI/L^3$, L being the needle length.

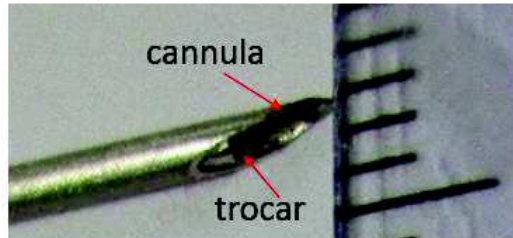


Figure 3.7 - Stainless steel bevel-tip needle composed by cannula and trocar.

The stiffness coefficient at the tissue's surface level has been estimated by measuring force and axial displacement of the needle tip for short insertions ($\delta y = 5 \text{ mm}$ depth) while touching the tissue (Fig. 3.8). Robot's encoders were used to obtain δy .

According to (Glozman and Shoham, 2007), the local stiffness parameter is an important spring coefficient that expresses the force of the tissue on the needle as a function of local displacement. As the shape of the tissue's surface changes, the location and orientation of this virtual spring change accordingly. Therefore, the force F applied by a virtual spring is proportional to the displacement of the spring from its initial position $\delta y = (y - y_0)$:

$$Kt = F / (y - y_0). \quad (3.10)$$

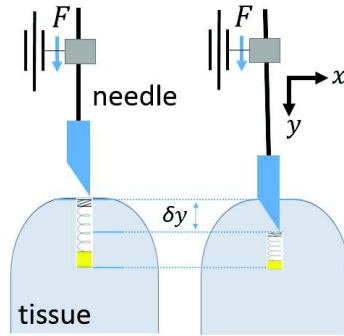


Figure 3.8 - Qualitative tissue stiffness measurement.

3.3. Results

We conducted percutaneous insertions of a semi-rigid needle into elastic tissues. Insertion depth average was nearly 51 mm and the experiments were observed under two different sets. A first set of experiments considered free insertions of the needle into PVC and pork. Vertical insertions as well as insertions inclined by 10 degrees in various directions were performed to test the robot steering capabilities and study their effect on needle deviation. A second set of experiments were performed only into PVC. It consisted of applying lateral movements in the base of the needle in order to observe its impact over needle tip trajectory, as well as system's potential to steer the needle. It will be presented in details below.

3.3.1.a. Free insertions

Image and fiducials data

The Fig. 3.9 shows three-dimensional reconstructions of CT images obtained during the insertions using LPR. The images show the results of different filtering using the software Paraview (Kitware, 2015). Fig. 3.9.A-B shows the needle interacting with tissues surface and Fig. 3.9.B-D provide information about needle behavior inside the tissue. The glass seeds embedded into the phantom are visualized into the images.

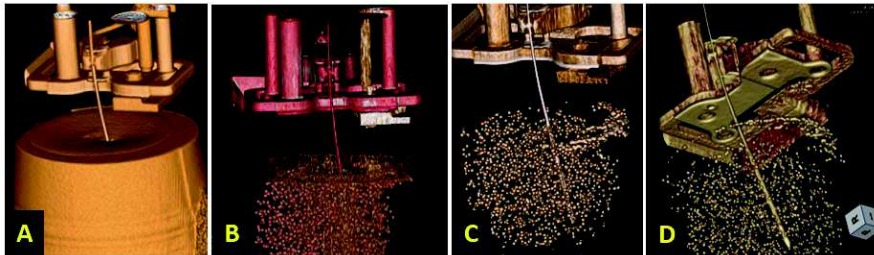


Figure 3.9 - Three-dimensional reconstructions of percutaneous insertions using LPR.

Reconstructions of the insertion experiments allowed observations of external (Fig. 3.10) and internal (Fig. 3.11) tissue deformations as well as needle deflections orthogonal to the insertion direction (Fig. 3.12.B). The Fig 3.10 shows axial tissue's deformation of around 2.4 mm due to the interaction with the needle. Such deformations were used associated to force data in order to obtain qualitative measurements of tissue's properties.

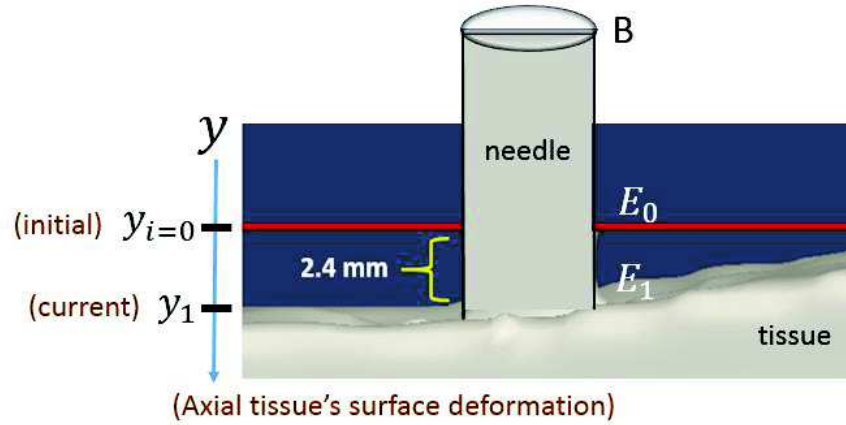


Figure 3.10 - External tissue's deformation (axial direction) at surface level. Three-dimensional reconstruction obtained from CT images

The internal tissues deformations were observed by measuring the displacement of the glass seeds before and after the insertion. The center of coordinate of each seed is determined by projecting each seed to the three main planes (xz , xy , yz). Applying a minimal distance algorithm that cluster the center coordinates of the same seed before and after needle insertion allows the visualization of the particle displacement as illustrated in Fig. 3.11.

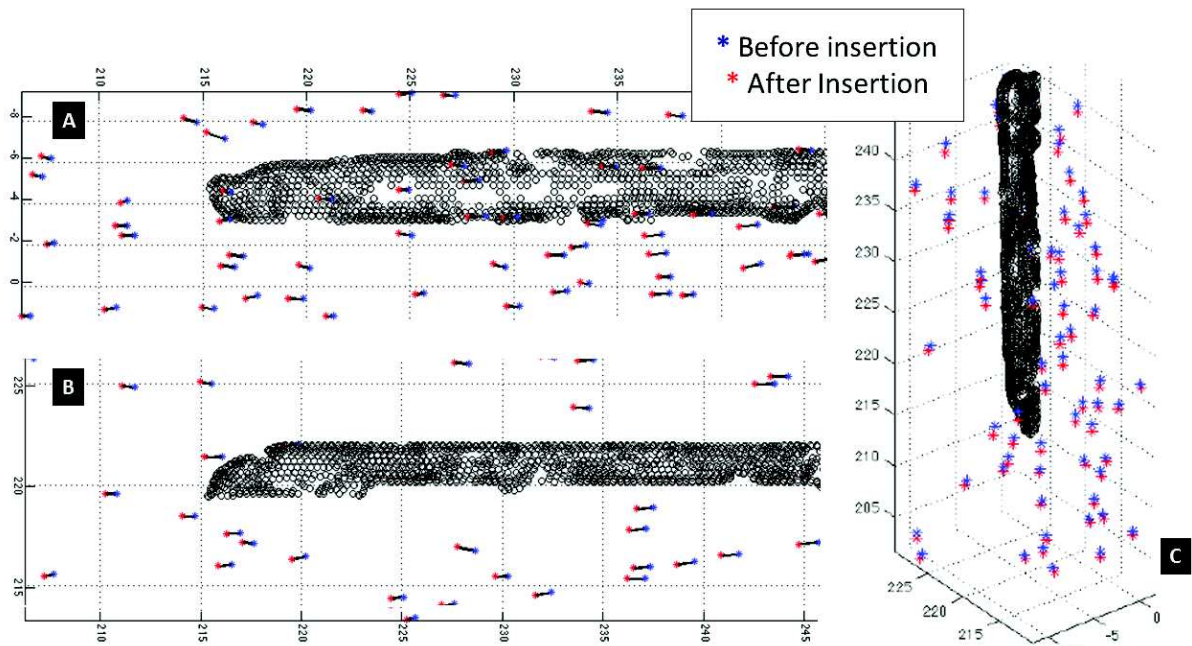


Figure 3.11 - Displacement of glass seeds embedded into the PVC phantom tissue. A. xy plane. B. zy plane. C. 3D volume. Units in mm.

It is important to notice that the seeds displacements were observed only in PVC. The mechanical properties of PVC differ significantly from those of human tissue. Therefore, the results only give a rough approximation of the deformation of biological tissues common into clinical scenario. In addition, the friction between needle and living tissue will be much lower than between a needle and PVC.

It was observed that the particles are mainly displaced in axial direction along the needle shaft. Additionally, the displacement seems to be depth dependent, because major amplitude of displacement was observed closer to the tissue surface. Minor displacements were observed along the needle shaft. Such observations gave an idea about what could be target movement due to needle-tissue interaction. In future works, modeling of such displacement could provide prediction's compensation regarding to target displacement. This observation supports initial assumption, supposing neglectable displacement of the target, during experiments using PVC.

The tracking of the needle tip position was performed by manual cropping of the fiducial points along the position of the robot grippers, tissue surface and needle tip (Fig. 3.12.A). For each insertion step, the position points and their respective images were manually co-registered and indexed into a database. The 3D points were used to develop the models for needle deflection. Such data were used as ground truth in the insertion simulations, according to presented further.

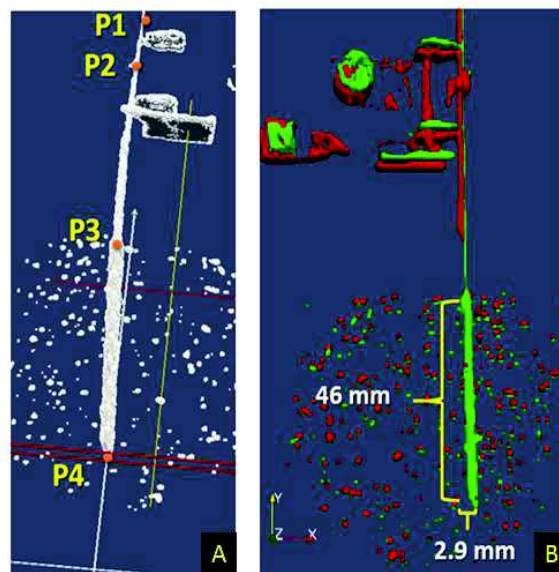


Figure 3.12 - Left: Manual crop of fiducial points used as needle position ground truth - P1 and P2 indicate LPR grippers positions, P3 points to the tissues surface position and P4 reveals the 3D needle tip position. Right: Needle tip deflection orthogonal to the insertion direction.

Force measurements

The observation of the force measurements reveals characteristics that describe needle insertion according to the setup designed to this pilot experiment. Fig. 3.13 shows the axial (z) and transversal (x,y) components of the force actuating in the needle insertion sample. The time of the insertion step is irregular (without defined frequency) and performed iteratively (*store&forward*).

As seen, the axial force is not constant and its intensity is directly related to the insertion depth. It can be confirmed by the observation of the three main peaks, which concerns to the sequential insertion steps of 10 mm depth. Intermediate peaks of lower intensities are noises concerned to the displacement of the grippers when loading pressure before to trigger the insertion. The maximum axial force measured on this sample was of 4N, having the final insertion depth equal to 30 mm. In other tests, the range of this force reached until 8N for the case in which the needle was tilted 10 degrees before start the insertion. The nominal difference in the force measured in the second case, concerns to the depth of insertion that was nearly of 46 mm and shows that the interaction force increases with the insertion depth.

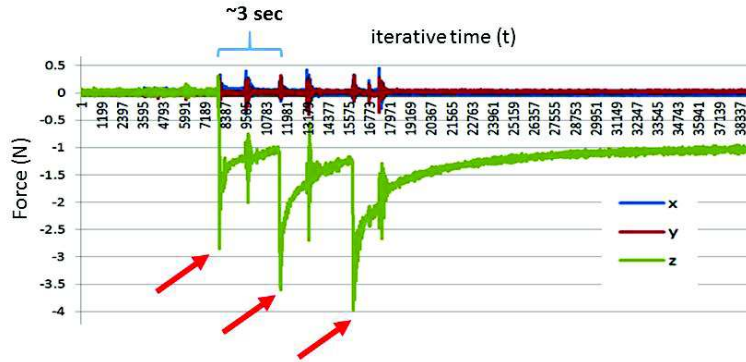


Figure 3.13 - Force data sample for needle vertically inserted into PVC. The three peaks (narrows) indicate insertion step performed under iterative time.

As seen, the axial force pattern concerned to each insertion step reveals peaks (narrows) followed by reduction of the intensity with logarithmic pattern. It happens because of the tissue relaxation. For this sample, the system reaches the stability at nearly 1N, after nearly 5 seconds of resting. Comparatively, this time is much less than the usual time to acquire 3D images from CT or MR machines, which is dependent of factors as volume of the workspace and voxel resolution.

The transversal forces were observed to have a behavior nearly constant in this sample, when compared to the axial force. It may suggest energy conservation and absence of extra interference, considering the insertion depth of this experiment. Moreover, the intensity of the axial force (z) is observed to be much more significant than the transversal forces (x and y) actuating into the needle. It obviously explains why the needle moves more in the axial direction than into the transversal one. The analysis of the transversal forces and their impact over needle deflection will be discussed in details in the next chapter.

3.3.1.b. Lateral motions in the needle's base

Lateral movements in the base of the needle were applied in order to observe the behavior of the needle through the tissue interaction. Such motions are proposed to be used in the future into needle steering applications. We observed the feasibility of LPR to perform these motions and their impact over the original needle path. The Fig. 3.14 shows 3D reconstruction of an experimental sample.

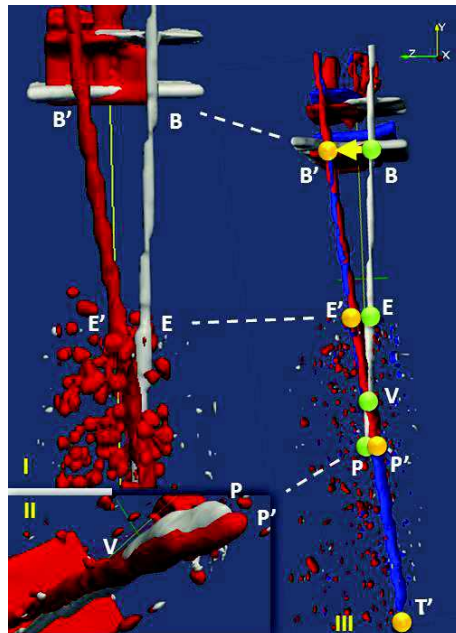


Figure 3.14 - Three-dimensional reconstruction of the system under submillimeter resolution. Image shows insertion sample with lateral motion in the needle base (B-B'). I. Displacement of the needle shaft

in the tissue entry point (E'-E); II. Displacement of the tip (P-P') after pivoting in V; III. General view of the system for the three moments, showing main fiducial points.

The needle tip is placed nearly 30 mm depth into the soft tissue (BEP points). Lateral movement in the needle base is applied in the point B towards to B' point (~10mm). It is possible to observe the needle pivot around the point V. Then, new insertion (~30mm) is performed (T').

From the image, it is possible to observe the displacement of the needle's shaft (~2mm) in the tissue entry point (E-E') and the needle tip pivoting around the point V. The distance between V and P is of nearly 9mm. In despite of this, small displacement is observed in P-P' (~0.4mm). The model presented in the next chapter doesn't take into account such displacements (E'-E and P-P') and considers the needle pivoting around the point E. However, in the future, it could be source of modeling and novel estimation strategies could be developed in order to evaluate the impact of this input over model accuracy.

Fig. 3.15 shows two-dimensional CT slices of the two insertions approaches. The images show qualitatively the impact of the lateral motions while changing the needle path and by consequence, the mechanical potential of LPR to perform needle steering.

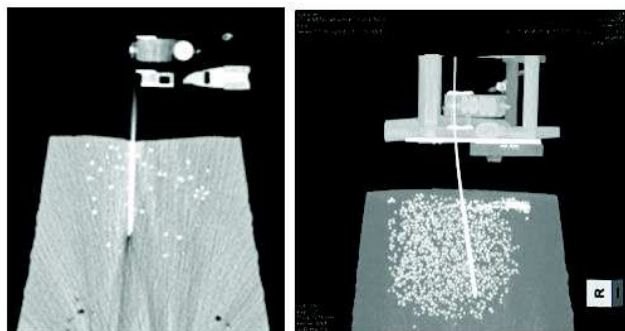


Figure 3.15 - Two-dimensional CT slices of free insertion (left) and insertion followed by lateral motion (right).

Force measurements for insertions into PVC followed by lateral motions is illustrate in the Fig. 3.16. Intensity of the forces orthogonal to the insertion direction reached nearly 1.8N when displacing the needle base around 10 mm. Narrows indicate the insertion steps. As mentioned previously the insertion depth (z-axis concerning to the force sensor frame) was of around 60 mm. It is possible to observe from the graphic that two insertion shots were needed to insert 30 mm. Then, after the lateral motion, three insertion shots were needed to insert the remaining 30 mm. It happens because of the difference of the nominative input forces involved in the two parts of this experiment.

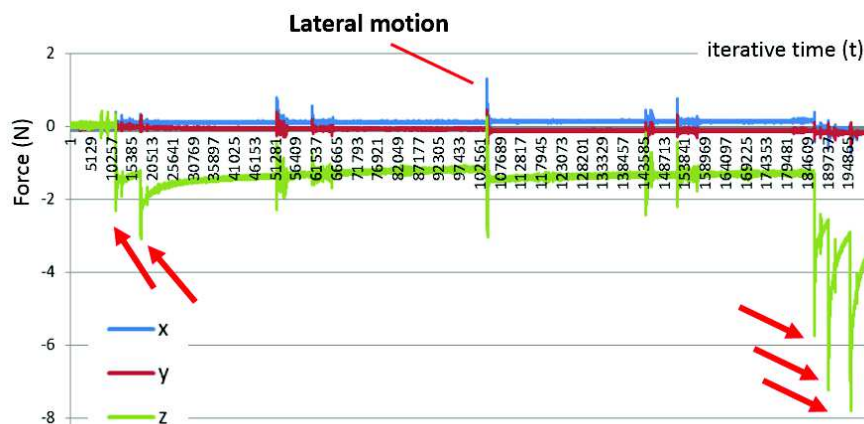


Figure 3.16 - Force data pattern for needle insertion with lateral motion using LPR. Narrows indicate insertion steps.

3.3.1.c. Surgical drape

The results presented in this section are observed considering the setup in which a surgical drape (100% polypropylene) was attached to the LPR robot using screws (Fig. 3.17). The sheet had several small holes making easier to the needle passing through. It was used as extra layer during the experiments.

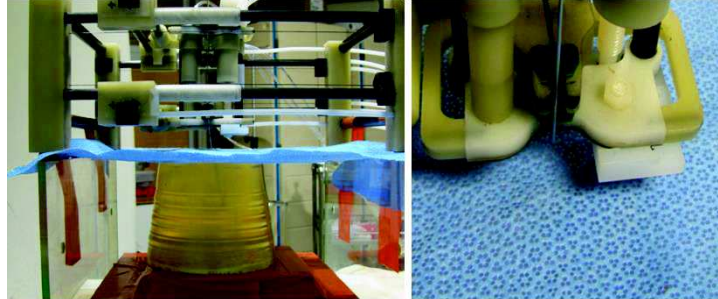


Figure 3.17 - Left: Surgical drape is attached to the LPR using screws. Right: Zoom showing small holes in to the sheet.

The purpose of using the surgical drape was of avoiding patient tissue indentation or tearing by reducing the force applied over the tissue surface, especially when the movements in the base of the needle is applied. Moreover, it can increase desired needle deflection effect when the transversal movement is applied in the needle base.

During the experiments, its function was mainly associated to the reduction of entry point displacements during needle steering. We observed that the displacement was nearly constant and around 2mm for both tissues used. It was expected, since such motion is constrained by the drape. Displacement without using the surgical drape was not measured. However, we understand that it would be highly sensible to the needle stiffness. Furthermore, the needle displacement is expected to be so large as needle stiffness can vary at the tissue's entry point.

The tests showed that the surgical sheet could aid deflection the semi-rigid needle until 7 mm nearly when it is manipulated in the base. Using the LPR robot, the lateral movement was applied in the needle moving its base 3 mm, followed by insertion of 60 mm depth. The needle-sheet interaction produced the effect of deflecting the needle even when no interaction with elastic phantom tissue is present (*i.e.*, without tissue interaction) (Fig. 3.18). Obviously, even more significant deflections were comparatively verified when the needle base moved of 5 mm, reached 6 mm of deviation, considering 30 mm of insertion depth into PVC.

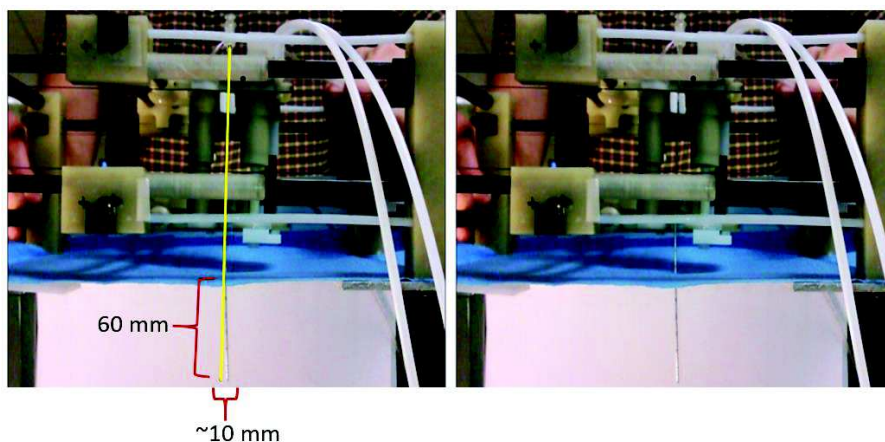


Figure 3.18 - The surgical drape works as extra-layer and can help the needle to deflect. In this example, the needle was bended nearly 10 mm even without interaction with elastic medium.

Tests performed under same conditions showed that the needle-drape interaction can pre-bend the needle increasing the deflection effects until 16% more when compared to the case in which the needle is inserted without the transversal movement. Moreover, the surgical drape decreases the entry point motion while needle steering is performed. This is in accordance with our model assumption of neglected entry point motion during needle manipulation.

3.3.1.d. Pilot simulation

The needle position fiducials, data force and parameters of needle and tissues were carefully stored and used as ground-truth to validate the adaptive slope model. Therefore, given preoperative (offline) inputs, it was possible to estimate needle deviation orthogonal to the insertion direction, according to the insertion depth of each insertion sample. For this pilot study, simulations results were obtained only for samples based on free insertion experiments.

The amount of needle deflection was obtained after matching the deflected path with the initial straight-line path. Fig. 3.19 shows measured deflections at various depths for two experimental insertion samples (PVC and pork). The measurements are compared to the simulated deflections obtained using the proposed model.

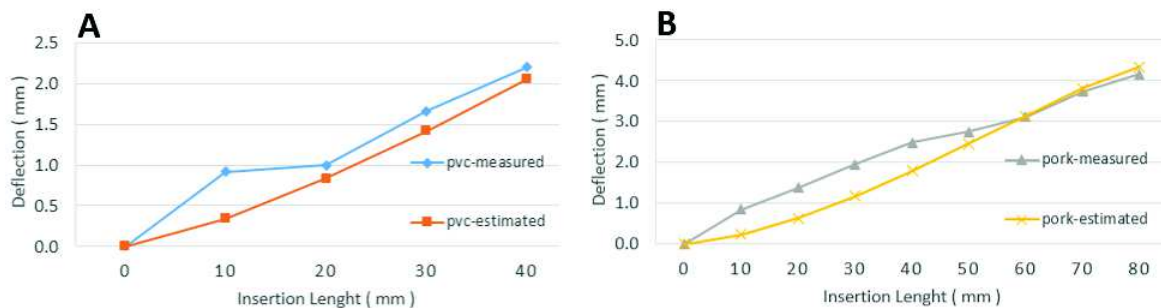


Figure 3.19 - Deflection samples of two needle insertions using PVC (A) and pork (B).

The figure shows simulations and experimental results compared under the same conditions. The first sample refers to a 40 mm insertion into PVC, with a final tip deflection of around 2.0 mm. Simulation results followed the same trend as the measured experimental results at all measured insertion depths. Along the insertion, the errors between the measured and simulated results were observed to be less than 1 mm, regardless the insertion depth. It is possible to observe that the error decreased with increasing insertion depth.

Simulation results showed an average error of 0.46 ± 0.48 mm for PVC and 0.68 ± 0.27 mm for insertions into *ex-vivo* pork. Moreover, the data forces collected into this study allowed to compare our results with other needle deflection models, such as cantilever beam with free end load (Abolhassani and Patel, 2006), using the same experimental conditions.

The Fig. 3.20 shows a comparative illustration of the simulation errors obtained using the adaptive slope model and cantilever beam, compared to a linear referential.

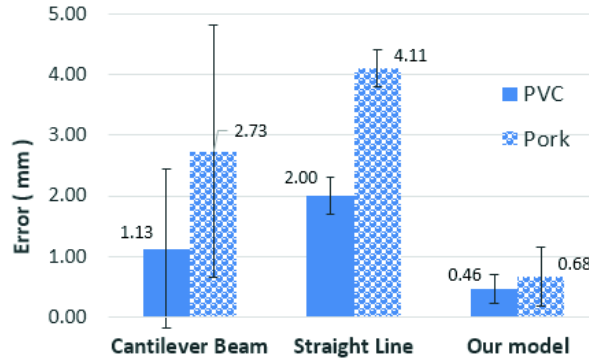


Figure 3.20 - Average error of the needle deflection predictions for insertions into pork and synthetic soft PVC. Errors were calculated comparing the simulations results with deflections obtained in the experiments.

The simulation errors of the proposed model were stable for inter-tissue stiffness variations (PVC to pork) and for intra-tissue stiffness variations (nonhomogeneous pork). It was not observed, for example in the predictions provided by the cantilever beam model. Such results showed the potential of our needle deflection estimation approach and evinced the need to evaluate the model behavior under a more extended validation, using experimental data extracted online from experiments. It will be presented in details into the next chapter.

3.3.1.e. Heuristic analysis

Observations of the preliminary experiments, such as described above, supported application of heuristic technique to define H_0 : Such experiments were considered as a training phase for offline predictions. Therefore, the measured δx in percutaneous insertions of the 17 degrees bevel tip semi-rigid needle interacting with PVC and ex-vivo pork tissues were used for the model's fitting regarding to the initial H 's value (H_0). Using (3.6), H_0 was found to be nearly constant into the empiric data samples obtained for the used needle, presenting an average value of 0.06 and a standard deviation of 0.004. Such finding was important to preliminary evidence the strongness of the parametrical set used in (3.5). Additionally, even if this study was performed with one needle type, we understand that such constancy of H_0 reveals its potential while characterizing the appropriate slope concerning to the set of system's parameters related in the model. The low standard deviation and error values observed during the training also reveal the potential of such initial value to provide pre-operative needle deviation predictions.

As expected, H_0 was found to be smaller than 1. It happens because the transversal force (R_x) in (3.4) tends to be much smaller than the axial force (R_y). This is due to the fact that the needle moves more axially than transversally. Both factors are considered to contain the parametric abstractions assumed to influence needle deflection: needle tip asymmetry, tissue and needle stiffness, insertion depth and resultant forces (virtual springs). Therefore, if the most important parameters provoking needle deflection are contained in the model's factors, the approximations with less significant meaning - represented by H - should express little variation under short insertions. It can be confirmed by the very low pattern deviation of H_0 . Such observation is also in accord with the observations of (Misra et al., 2009), in which pure needle bending energy is showed to be the only energy with significant value in the system for the initial insertion depths (<40 mm).

3.4. Conclusion

This chapter presented in detail the observations derived from the preliminary insertions experiments using LPR under CT-guided scenario. The adaptive slope model presented here will be used as core of the solutions developed in the rest of this thesis.

During the robotic-driven needle insertion experiments, a surgical drape was used as extra-surface layer in order to reduce tissue indentation and orthogonal forces applied into the tissue surface when applying lateral movements in the base of the needle. It contributed to lead the needle to perform a desirable pre-bending and maximizing deflection effects. Tests results suggest that this technique could support the needle path correction. The observations performed during experiments show that the use of surgical drape during lateral motions in the needle base has potential to maximize needle steering effects and reducing damages into the tissue surface.

Studies presented in the next chapter are concerned to the development of a robot-assisted needle insertion system. The needle deflection model presented in this study is integrated into an adaptive needle insertion planning with needle steering assistance. Its design was motivated by the constraints of ARCS scenario, in accord to the challenges imposed by the clinical potential of the LPR robot platform.

Chapter 4. Teleoperated Robot-Assisted Needle Insertion and Steering

Robot-driven percutaneous interventions have been proposed in order to assist needle insertion procedures into soft tissues. Basic requirements for such robotic systems involve needle insertion planning with steering algorithms and needle deflection modeling that could improve insertions performance. This chapter provides a detailed and comprehensive description of the teleoperation platform (Section 4.1) proposed to perform a full range of robot-driven applications into IR such as, needle translation, orientation and insertion. As previously mentioned, our approach was designed in order to face scenario challenges concerned to bore space, ferromagnetic compatibility and radiation avoidance. Next, in Section 4.2, we provide validation results for the adaptive slope model in order to explore its behavior under an unknown context such as a different robotic platform. Moreover, we present concept, design and validation experiments for the adaptive needle insertion planner, designed to offer preoperative planning assistance as well as intraoperative decision-making support. Finally, Section 4.3 presents the feasibility and advantages of merging steering assistance, offline deflection prediction and online adaptive corrections based on the needle-tissue properties, tip asymmetry and needle tip position updates.

4.1. From surgery to remote therapeutic systems

The therapeutic activity practiced by the means of the “hands” was defined by Hippocrates (480-390 B.C) as *surgery*. At the time, the figure of the ancient surgeon was surrounded by a kind of mysticism because they touched the inside of the sacred human body with naked hands. It is attributed to Halsted, pioneering the use of the surgical glove in 1894, separating the surgeon a little further from the patient (Wall and Marescaux, 2013). Advances along the last century moved surgeon’s hand outside the body to reduce surgical trauma in fields such as laparoscopy surgery. Finally, considering IR-based therapies, even the tools used in the minimally invasive surgery have their size decreased (e.g., by using needles and catheters) in order to improve patient outcomes. Surgical robotics has produced the technology to disrupt even more the paradigm of surgeon-patient proximity.

The introduction of Robotic and Computer Assisted Technologies in the late 1970s and early 1980s made possible using a robot as surgeon’s hands and eyes at a distance. Indeed, extend the physical reachability of a surgeon when treating a patient in another locality was one of the promises that headed to some of the major grants from DARPA (Defense Advanced Research Projects Agency), NASA (National Aeronautics and Space Administration) and NIH (National Institutes of Health). Such investments led to the development of the prototypes of the da Vinci (da Vinci Surgery, Intuitive Surgical Inc., CA) and the Zeus (Zeus TS, Computer Motion, CA) systems that were originally

developed to provide emergency surgical care to the remote operatives. It revolutionized the practice in the robotic surgical field in the late 1990s (Anvari, 2011).

4.1.1 Early experiences

Early experience of teleoperated therapeutics has been associated for decades with the practice of telemedicine - defined in (Senapati and Advincula, 2005) as “*the use of medical information exchanged from one site to another via electronic communications for the health and education of the patient or healthcare provider and for the purpose of improving health patient care*”. However, recent advances in telecommunications and computer technology have allowed for the development of more efficient complex applications. While the first employment of telemedicine was registered in 1950s (Anvari, 2011) to support patient care in remote areas (using closed circuit television), only in the 1990s, telemedicine infiltrated main stream medicine pushed by the development and commercialization of remotely controlled robotic surgical devices at which time telesurgery became widespread (Anvari, 2007).

The first FDA approved procedure specific robotic surgical system was the AESOP (Automated Endoscopic System for Optical Positioning). It was used in 1994, when Dr Louis Kavoussi successfully performed three telementored surgeries in which the instructing surgeon was in the adjacent room (Kavoussi et al., 1994). The system has been demonstrated to effectively replace a human assistant without effecting surgical outcomes or significantly increasing operating time. According to (Anvari, 2011), AESOP served as the foundation for the development of many other robotic surgical systems.

The first successful demonstration of two-handed telesurgery was performed by Prof. Jacques Marescaux and his team from IRCAD in September, 2001 (Fig. 4.1).



Figure 4.1 - Teleoperated surgery using Zeus system, demonstrated by Dr. Jacques Marescaux in New York on the patient in Strasbourg, France. Source: (Marescaux et al., 2001).

The one-hour demonstration was named Lindburgh operation. Using a teleoperable Zeus system, he successfully performed a laparoscopic cholecystectomy from New York on a patient located in Strasbourg, France (Anvari, 2007). The operation used ATM (Automated Teller Machine) connectivity and a high speed fiber-optic network throughput with virtual connections dedicated per customer. Such connection presented average transport delay of 155 ms and low packet loss ratio with 99.9% of reliability in terms of network outage. A backup line was available in case of line congestion. For this operation, there was no report for unexpected telecommunication or robotic mishaps (Marescaux et al., 2001). Further works have demonstrated the benefits of using clinical telesurgery service in the assistance of patients in hospitals of rural communities. In the work described in (Anvari, McKinley and Stein, 2005) they used regular commercially available IP/VPN (Virtual Private Network based on Internet Protocol) telecommunication lines, which operated at a bandwidth of 15 Mbps, using highest priority of QoS, security and privacy to assure the most rapid rate possible and an active backup that could be used.

IP protocols are highly recommended, since the protocol remains always the same, whatever the communication links used. Transmission Control Protocol (TCP/IP) can be used for basic connection (*i.e.*, control data to ensure the device connections), however it is not suitable for images or video transmission (Slama et al., 2008; Xiaohui, Zhijiang and Lining, 2003). Such protocol has the intrinsic characteristic of reducing the network rate when the transmission reaches the speed limitation of one of the link of the network chain due to the repetition of packet loss. In opposition to that, User Data Protocol (UDP) is connectionless protocol, more adapted for images or videos. They are not sensitive to the problem of communication link overload due to lost packet repetition. The drawback is exactly the fact that UDP doesn't assure repetition of lost packages and, therefore, no guaranty of information delivery is provided. The best choice between the protocols depends on the application on hand: for real-time transmissions using images, it could be better to lose one image than to overload and block a communication link (Vieyres et al., 2013). According to (Anvari, 2011), the most effective mode of telecommunication between the surgeon console and the robotic slave arms by side of patient is broad band IP (VPN) connectivity with Quality of Service (QoS) assuring rapid transit of information between the two sites. At latencies of less than 150 ms, the surgeon is able to complete the most complex of surgical tasks without significant error and in reasonable time. Earlier research has shown that once the latency rises above 200 ms, the surgeon has to slow down significantly to complete the task. Finally, once latency rises above 500 ms, it becomes difficult to accomplish the difficult surgical tasks (Anvari, 2007b). During NEEMO 9 (NASA Extreme Environment Mission Operations) - (NASA, 2011), planned surgeries at 2 seconds time delay (mocking the latency experienced between earth and moon base) didn't allow completing the most rudimentary surgical tasks. At such high latency connections, procedures using navigation-based or semi-autonomous robotic platform should be more appropriate.

4.1.2 Navigation for IR gestures

Robot-driven teleoperated interventional therapies have often relied on real-time imaging to monitor anatomic position during procedures. It is usually accomplished with 2D fluoroscopy, ultrasound (US) or CT/MR imaging. However, it doesn't make optimal use of spatial data from tissues, organs, targets and interventional tools available from the imaged scenario. For the case in which 3D imaging modalities are used, it is often followed by losses in temporal resolution, which can lead to important latencies during the insertion procedure. The physician conventionally makes use of this information by mentally registering the anatomic information from offline modalities to the modality used for guiding the actual procedure.

Navigation-based teleoperation platforms can provide important assistance to planning trajectory and steering of the needle performed at a distance under latent communication scenarios. Moreover, modeling of kinematics and biomechanical interactions involved in the system could provide more autonomy to the platform, while guiding the user during the teleoperated procedure.

In this work, we devised an IR navigation system and a teleoperation platform to assist robot-driven percutaneous procedures. The system assumes insertion procedures performed under iterative (asynchronous) time, respecting delays imposed by the 3D imaging acquisition modalities. The system combines hardware and virtual reality software to enable the surgeon to benefit from CT/MRI data during interventional procedures. The data is used for both targeting and guidance. The hardware is composed by a haptic master device and a slave robot, in which the interventional tool (needle) is mounted. The software usually consists of a preoperative interface (that allows patient registration and data loading) and an intraoperative (navigation) interface, which provides 3D overview display, illustrating position of the needle relative to the dataset. Slice view and additional information such as current depth of insertion and the distance of the needle tip to the target region. The image data is interpolated over the scanned volume, so that the 3D virtual representation on the GUI allows the user to visualize in the slices view the orthogonal planes classically used in the surgical routine.

In the most general sense, before the biopsy, navigation platforms can provides the surgeon with the ability to simulate the intervention at distance. During the biopsy, master device can be used to first help the surgeon to find the target and to define optimal trajectory, then to physically guide the

surgical (IR) gesture along the chosen path. Specifically speaking about ARCS, most of the previously mentioned robot platforms have reported some kind of teleoperated control system. Despite of this, so far, very little discussion has been proposed in the literature to devise navigation systems with potential to provide appropriated planning assistance, considering delays often found in teleoperated procedures compatible to ARCS.

Additionally, the teleoperation platform presented in this work is the only multimodal CT/MRI-guided that fully control needle translation, orientation and insertion. In the future, the approach aims supporting a clinical scenario as pictured in Fig. 4.2: the lightweight LPR robot is placed on the abdominal region of the patient in the imaging room (*e.g.*, CT scanner). Far from the radiation source, the physician controls at a distance the movements of the robot, using a haptic device and guided by a GUI (Graphical User Interface) of the navigation system, accessible from the imaging console.

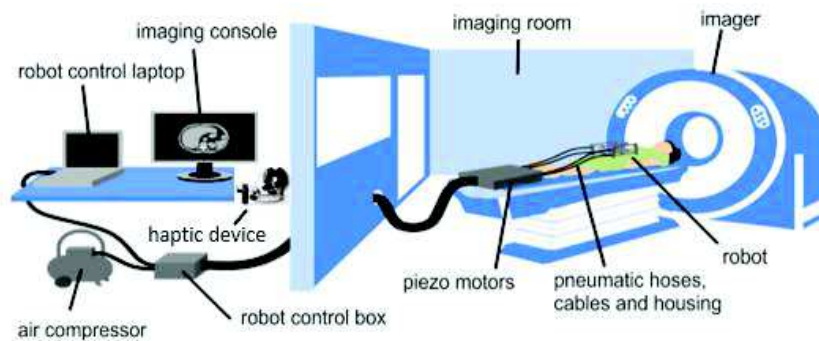


Figure 4.2 - Clinical scenario. Adapted from: (Dorileo et al., 2014).

This section presents pilot feasibility proof of this modular teleoperation architecture and provides option of robotic platform that could teleoperate the full range of needle steering during abdominopelvic percutaneous insertions under scenarios such as CT/MRI. Below, we describe in detail how we design a navigation system integrated in a teleoperation platform, proposed to assist robot-driven needle insertion into CT/MRI-guided abdominopelvic interventional procedures. Along this chapter, we also describe how we devise the improvement of targeting accuracy of the system and planning of needle trajectory and steering, guided by the predictions of the adaptive slope model presented above.

4.1.3 Teleoperated navigation platform

4.1.3.a. Teleoperation Architecture

A teleoperation platform was conceived to control the LPR robot. The developed modular architecture consists of a set of CamiTK (Computer Assisted Medical Intervention Toolkit) extensions. CamiTK (Fouard et al., 2012) is an open source toolkit devoted to help researchers and clinicians to easily and rapidly collaborate in order to prototype CAMI applications that feature medical images, surgical navigation and biomechanical simulations. Therefore, considering the modularity principles encouraged by this toolkit, we proposed an architecture that allows the various components of the teleoperated robotic system to be plugged or unplugged separately, making modifications and further developments easier to handle, without the need to affect the entire system.

The teleoperation architecture was defined following the master-slave model, as shown in Fig. 4.3.

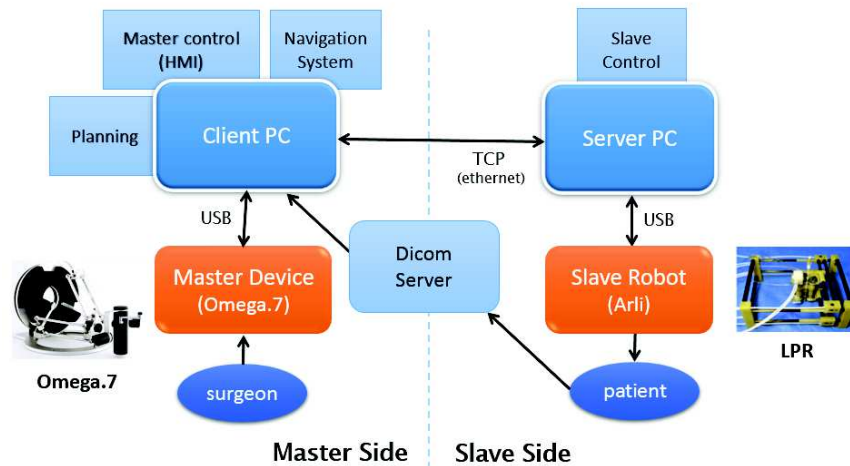


Figure 4.3 - Teleoperation architecture.

LPR is used in the slave side while a haptic device is used in the master side in order to command the robot. Omega.7 is a desktop haptic interface, commercially developed by Force Dimension (Dimension, 2001). This device has 7-DOF (three translations and grasping with force feedback and three rotations). Omega is used as the hardware that allows the control of the virtual needle in the navigation system. It provides more realistic understanding of the virtual world as well as active security constraint to the user (physical lock). For example, in our application, the haptic device allows physically blocking the needle's translational motions while defining the needle's orientation.

Two PC's are required as controllers. The first is placed on the master side and the second on the slave side. The client-server architecture model allows their communication through the Ethernet under TCP protocol. We chose this protocol because the iterative time of the experiment is not sensitive to delays in sending packages. The master-side PC acts as a client and receives the images coming from the remote scanner. The user interacts using the Omega.7 master device, through a GUI and sends action requests to the slave robot. The slave-side PC acts as a server and receives the control requests from the client PC. It translates these requests into robot control commands that are then, sent to the slave robot.

The client and server PCs had the following configurations: the server PC consisted of an Intel Core i7, 2.8 GHz, 8GB RAM, running Windows 7 64bits. The client PC consisted of an Intel Xeon, 2.4GHz, 12GB RAM, Windows 7 64bits.

4.1.3.b. Navigation system

The software components that compose the core of the navigation system are the GUI and the state machine. The system's interfaces were designed to facilitate and organize the required steps during preoperative planning and intraoperative assistance during the percutaneous insertion.

The GUI was developed to allow the user to navigate through the workspace provided by the 3D imaging. It improves the perception of the needle position and trajectory during its insertion. The GUI displays the three standard orthogonal slices that clinicians are used to seeing (transverse, sagittal, coronal) as well as a 3D reconstruction of these slices. The latter displays the position of the desired needle trajectory and target (which we will refer to as the virtual needle henceforth), the actual needle position, the LPR robot's workspace and the fiducials used to register the robot's workspace to the images. All these components were registered together in the image space and could be visualized together or separately, according to the user configuration.

For the teleoperation of the LPR robot, we proposed a scenario composed of phases and states. There were three phases: Initial, Planning and Execution. The states related to each phase are summarized in the Table 4.1.

We devised an application scenario consisting of an initial phase where the robot is registered to the first image. The planning phase consists of an exploration state, in which the user manipulates the Omega master device in order to explore the image volume and verifies that the image is correct and shows all the necessary elements. Omega.7 is used to actuate as a (7-DoF) 3D mouse. The position of the center of the Omega’s coordinate frame is used to scroll through the transverse, sagittal and coronal slices of the 3D image. Next, in the target state, the user can do the same exploration of the image, but with the specific purpose of choosing a target to which he/she desired the needle to be inserted to. The target location is set as the intersection point between the three orthogonal imaging planes and it is displayed by a virtual needle whose point moved with this intersection point. Next, an orientation definition state is used in which Omega.7 locks its x-y-z translations, allowing the user only to orient the handle. In the image feedback available at GUI, the intersection point of the three orthogonal planes, centered on the chosen target point, is also locked, and instead, the transverse and coronal planes are oriented based on the rotational motion of the user. It allows the user to define the orientation of the needle insertion trajectory in the image without change the virtual needle tip position.

Once a target and insertion direction were chosen and validated by the user, the execution phase is entered. It first consists in a move slave robot state. In this state, the user sends a command via TCP to the server PC which in turn orders the LPR robot to move the needle into the requested position/orientation above the phantom. In the next state, the second image is loaded and registered, showing the needle in its position above the phantom. By exploring through the image with the Omega.7 device, the user is able to see when the needle is not exactly aligned with the desired trajectory. Therefore, a new and more accurate trajectory could be chosen by returning to the previous planning phase.

Table 4.1 - Table of phases and states of the system.

Phase	State
Initial	First image + registration
Planning	Image Exploration
	Target definition
	Orientation definition
Execution	Move slave robot
	New image + registration
	Insert needle

After a second motion of the needle, the third image is loaded, showing the needle accurately aligned with the desired needle trajectory and target. The next state is therefore insertion of the needle, in which the user sends the insertion command to the server PC and the robot inserts the needle to the requested depth inside the phantom. Then, the final image is displayed, revealing how the needle hit its target.

4.1.3.c. Qualitative results

Modular software architecture

The modular platform was developed on top of the CamiTK core, as a set of CamiTK extensions (Fig. 4.4). Therefore, the slave robot and the master device were controlled through their own respective extensions. A generic connection interface extension was created for each to which the specific master and slave control classes could be plugged. The goal of these generic interfaces was to

allow any kind of slave robot or master device to be plugged into the architecture, without having to reprogram the core or the other extensions.

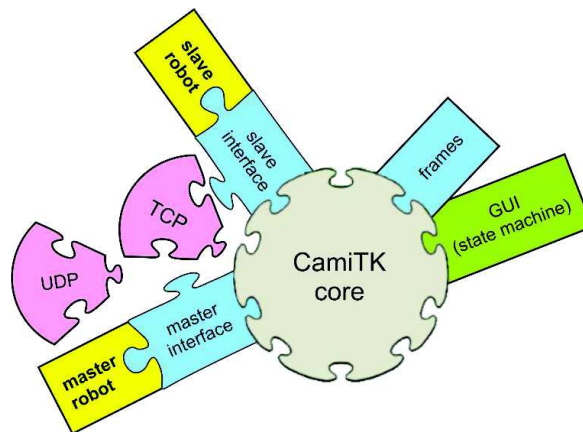


Figure 4.4 - General abstraction of the module integration proposed for the platform.
Source: (Dorileo et al., 2014).

Indeed, it also allowed each of the two PC's to run the exact same architecture without needing to install the other device's drivers. The communication protocols were also programmed as extensions that could be plugged into the CamiTK core. Although TCP communication was used in this experiment, it would be very simple to change to a different type of communication in the future.

Two auxiliary extensions were integrated to the core: the first one is committed to handling all the system's reference frames (images, virtual needle, real needle, robot workspaces, etc.). The second extension is related to the navigation system (GUI + state machine).

The assembling of GUI and state machine (Fig. 4.5) in the design of the navigation system, guides the clinician throughout the procedure by allowing him/her to progress back and forward through the protocol using next and back buttons. Considering each step, the system automatically loads all the necessary components and updated the 2D and 3D images with the appropriate elements necessary for the current step. This step-by-step procedure made it possible for any user, even if totally unfamiliar with the procedure, to use the system. It will be described in details following.

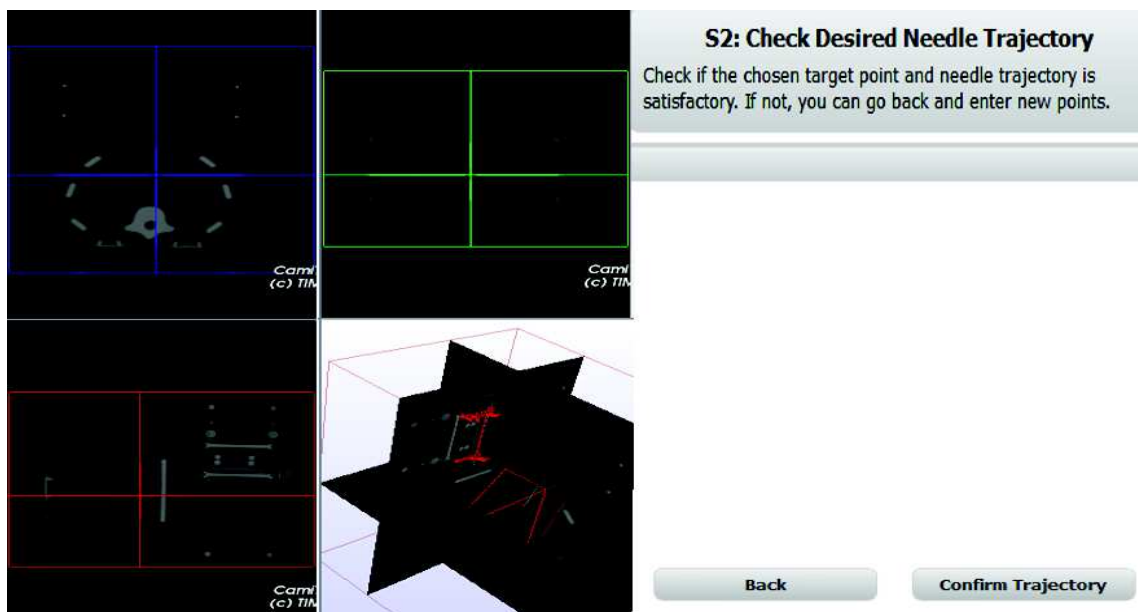


Figure 4.5 - The state machine was proposed to improve the usability and decrease the user learning time. During the procedure, the system guides the clinician through all the phases and states.

Public demonstration

Feasibility of the teleoperation robot-driven needle insertion platform was demonstrated during the Academy of Surgery in Grenoble, France on 22th May, 2013. For the demonstration, a radiologist in the city of Montpellier, France, was invited to perform a teleoperated insertion on a phantom located into another city (Grenoble, France). The LPR robot was placed on a synthetic phantom (Fig. 4.6) and the radiologist having the goal of reaching a target within the phantom.

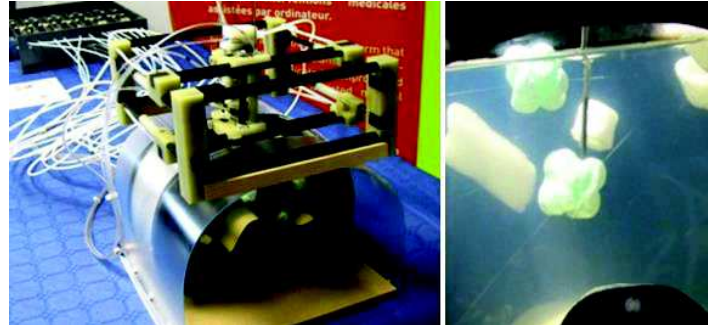


Figure 4.6 - Robot setup on the slave side in Grenoble. The robot was placed over a gelatine phantom with 15mm Styrofoam targets.

The experiment was done as a public demonstration for which we did not have access to a CT or MRI scanner. Therefore, we hypothesized the clinical scenario in which the clinician would plan an insertion in a first image, have to readjust the position in a second image and finally insert the needle to the chosen target in a third image. The three images were taken beforehand in a CT scanner in the same setup as during the demonstration (Fig. 4.7). Therefore, we used a “mocked” registration of the robot, since the image was taken prior to the test. The registration allowed the model of the robot to be displayed in the 3D image in the corrected location. Then, all the re-planning and corrections were performed guided by the navigation system and with the user controlling the haptic device in Montpellier.

Guided by the GUI (Fig 4.7-B) and following the steps devised in the state machine, the radiologist executed a predefined workflow under a hypothesized clinical scenario with several tasks while positioning and inserting the needle. The radiologist, who was unfamiliar with the system, was successfully able to guide the needle using the Omega device and insert the needle to reach the chosen target in nearly 13 minutes (Fig 4.7-D).

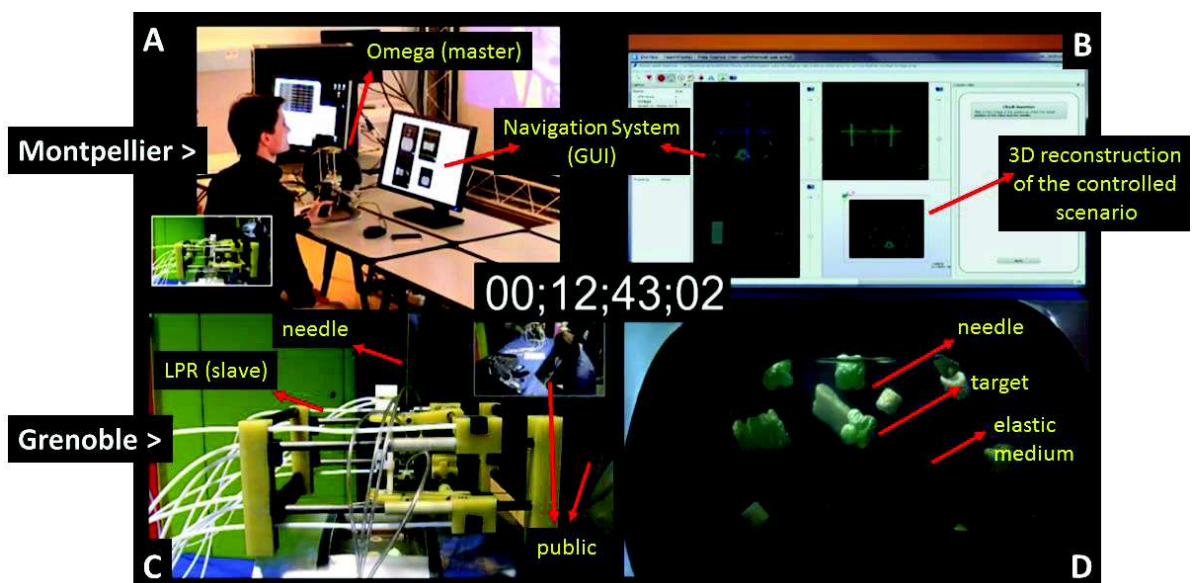


Figure 4.7 - Public demonstration. The radiologist, in Montpellier (A), commands the robot’s movements in Grenoble (C). The navigation system (B) provided user guidance during the needle positioning, orientation and insertion in order to reach the target in the phantom (D).

The communications protocols were stable during the procedures and showed to be compatible to the sequential insertions performed under iterative time. Connections' latency between Montpellier and Grenoble were stable and around 10 ms, using the high throughput network (10Mbits/s), available by using the RENATER (National research and education network in France) infrastructure.

4.1.4 Discussion

In this section, we presented a modular teleoperation architecture for CT/MRI-guided robot-assisted percutaneous insertions. The teleoperation platform allowed the LPR robot to perform translation, orientation and insertion at a distance, while qualitative experiments demonstrated its operational feasibility targeting (pre/intraoperative) planning of needle insertion, guided by an interactive navigation system. Quantitative study to measure and evaluate the accuracy of needle insertion into soft tissues using LPR robot, will be provided through the work developed along this thesis.

Connection and communication protocols as well as the controllers used by the navigation system of the modular architecture were stable during the experimental procedures. The implementation of the navigation interface (GUI) with a state machine was very important to improve the user's perception and orientation through the several phases of the experiment protocol, performed under iterative time.

The robot platform presented in this work provided tools with the aim of support planning of percutaneous procedures with teleoperation command of translation, rotation and insertion of the needle. Its feasibility has potential to provides benefits such as, radiation avoidance (CT), feasibility of needle insertion control into workspaces limited by physical access (CT/MRI bores) and safety improvement (Pacchierotti et al., 2014).

In the future, additional work could include assembling extension modules focused on tasks as automatic needle detection and target segmentation. These tasks are already being developed in parallel by studies of partners, according to the ROBACUS project definitions. Such modules will improve the usability and performance of the GUI, while providing assistance to the user during the insertion procedures. Finally, quantitative analysis of the teleoperation platform could help to measure the impact of the current solution and compare it with future improvements. It will be discussed below.

4.2. Adaptive needle insertion planner

We will present now, the development of a needle insertion planning approach to evaluate the feasibility of merging needle-tissue kinematical and biomechanical properties to assist needle placement. Needle deflection model is validated under a different robotic platform, considering uncertainties of a different scenario. In addition, conceptual basis, design and validation of the needle insertion planning algorithm is provided. We also discuss about potential of the system while offering preoperative planning assistance and intraoperative decision making support.

4.2.1 Conceptual basis

Although the subject of motion planning spans a broad of models and problems into a number of fields, there are several basic ingredients that arise throughout virtually all of the topics covered as part of planning (LaValle, 2006):

- I. **State:** Motion planning problems involve a *state space* that captures all possible situations that could arise. The *state* could, for example, represent the position and orientation of the needle tip, or the position and velocity of a robot's end-effector. Both, discrete (finite, or countable infinite) and continuous (uncountable infinite) state spaces may be allowed. In most applications, the size of the state space (in terms of number of

states of combinatorial complexity) is much too large to be explicitly represented. Nevertheless, the definition of the state space is an important component in the formulation of a planning problem and in the design and analysis of algorithms that solve it. A planning problem usually involves starting in some initial state and trying to arrive at a specified goal state or any state in a set of goal states. Actions are selected in a way that tries to make this happen.

- II. **Actions:** A plan defines *actions* (or system's inputs) that manipulate the state. Somewhere in the planning formulation, it must be specified how the state changes when actions are applied. This may be expressed as a state-valued model for the case of discrete time or as an ordinary differential equation for continuous time. Such paths could be obtained as the integral of differential equations, but this is not necessary. For some problems, actions could be chosen by *nature* (e.g., nondeterministic or probabilistic), which interfere with the outcome and are not under the control of the decision maker. This enables uncertainty in predictability to be introduced into the planning problem.
- III. **Time:** All planning problems involve a sequence of decisions that must be applied over time. Time might be explicitly modeled, as in a problem such as driving a car as quickly as possible through an obstacle course. Alternatively, time may be implicit, by simply reflecting the fact that actions must follow in succession (*i.e.*, store-forward). The particular time is unimportant, but the proper sequence must be maintained. As in the case of state spaces, time may be either discrete or continuous. In the latter case, imagine that a continuum of decisions is being made by a plan.
- IV. **Plan:** According to (LaValle, 2006), in general, a plan imposes a specific strategy or behavior on a decision maker. It may simply specify a sequence of actions to be taken; however, it could be more complicated. It can predict future states, while enabling *feedback* or *reactive* plans. It might even be the case that the state cannot be measured. In this case, the appropriate action must be determined from whatever information is available up to the current time. This will generally be referred to as an *information state*, on which the actions of a plan are conditioned.
- V. **Criterion:** There are generally two different kinds of planning concerns based on the type of criterion.
 - a) *Feasibility: Find a plan that causes arrival at a goal state, regardless of its efficiency;*
 - b) *Optimality: Find a feasible plan that optimizes performance in some carefully specified manner, in addition to arriving in a goal state.*

The criterion (b) is very close to the definition of *adaptive* planner; meaning the ability of the algorithm to modify its own operation in order to achieve the best possible mode of operation. It is a very useful ability to face uncertainties of the medium.

4.2.1.a. Application context

Motion planning algorithms can compute feasible trajectories for systems, with some additional coverage of feedback and optimality. According to the presented previously, LaValle (LaValle, 2006), proposed some basic components that arise throughout virtually all of the topics covered as part of planning: I) Time; II) Actions; III) Plan; IV) Criterion and V) State. The link of our work with these basic components will be discussed in this subsection in the aim of supporting the characterization of our approach under the theoretic context of the adaptive needle insertion planning.

- I. **Time:** For this study, we consider that the system can work under iterative (asynchronous) time or under synchronous time. For the first case, each decision can be taken only after the previous process is over. It usually happens in ARCS, in which the

CT/MRI machine can take around 4s to update and reconstruct the workspace under 3D imaging. For the second case, the synchronous time occurs, for example, when regular insertion intervals are defined before start the insertion. It is the case for the experiments setup designed for this validation study.

- II. **Actions:** Actions are generated by the plan and can manipulate the state. The main actions specified to the planner developed in this work are:
 - *estimateEntryPoint()*
 - *simplifiedPlanning()*
 - *adaptiveReplanning()*They are discussed in details following, as well as, how the state changes when actions are applied.
- III. **Plan:** The predictor's strategy imposed to the planner is the following up of the needle tip deflection behavior, modeled by the prediction model. It can predict future states of the insertion procedure, while allowing to the planner performing intraoperative replanning assistance. Considering the clinical demands of ARCS scenario, for each insertion step, intraoperative decision-making support can guide the user in order to avoid future predicted damages. Therefore, two main reactive plans are possible:
 - a) *perform needle insertion (authorize next insertion step); or*
 - b) *withdraw the needle - procedure aborting followed by insertion retrial - in case of the planner indicates that continuing the needle insertion could be unsafe to the patient or compromising the success of the procedure.*
 - c) *steer the needle to correct its trajectory and improve targeting precision (detailed in the next section).*
- IV. **Criterion:** The algorithm's design works under the concept of optimality. Shortly, as described above, in addition to arriving at the goal state, the planner is able to modify its own operation in order to achieve the best possible mode of operation. It is a very useful skill when facing uncertainties of the medium.
- V. **State:** We proposed a state machine composed of an initial and a goal state, having as intermediate states: the pre-insertion planning, the intra-insertion replanning and the idle state. We will describe bellow how the planner goes through these states considering the main actions required by the clinical scenario in ARCS. The Fig. 4.9 shows how the planner goes through these states considering the main actions required by the devised clinical scenario. It is described as follows.

The procedure starts when the user defines the target position. At this moment, we start the pre-insertion planning state, which is defined as the moment before the needle touching the tissue. A sequence of actions allows the system to switch to idle state and back again. Idle is the state in which the planner is basically waiting for user's decision or robot-driven needle movement. For example, as soon as the target is defined, the system can estimate the optimal needle entry point (*estimateEntryPoint()*) for the current procedure. Once the robot places the needle in the proposed tissue's entry point and it is ready to start the insertion, the user can confirm manually (using a mouse's click) the position of the needle tip (manual needle's registration). This step is necessary to assure that the user is correctly following the assistance provided by the system, or else, if there is some inconsistency between what the system suggested and what the user actually did. It is important to reduce source of errors in the planning. Next, the system runs the *simplifiedPlanning* algorithm, meaning the initial planning that will be performed preoperatively. As soon as the robot starts the needle insertion, the planner starts the intra-insertion (online) replanning state, in which a loop of actions runs until that the system reaches the goal state. In short, as mentioned before, for each insertion step, the user/system manually updates the needle tip position. Then, the system replans the

path previously planned (*adaptiveReplanning*). The main algorithms mentioned here, as well as, how the Simplified model (*calcDeflection*) was embedded in the planner, are presented in detail in the Algorithm 1, detailed in the Appendix B.

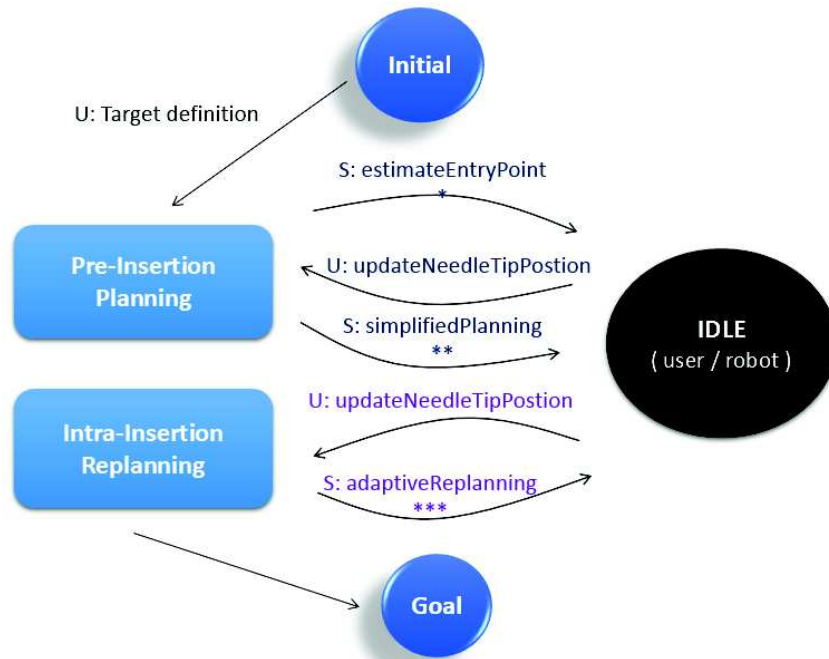


Figure 4.8 - Phases of needle insertion planning.

4.2.2 Methods

We present in this section, a new planning method for percutaneous insertions. It uses the needle's deflection prediction model presented in Chapter 3 in order to minimize the reinsertion trials or other errors that could compromise the intervention's success. The adaptive needle insertion planner uses the needle deflection model as predictor's strategy.

The planner provides preoperative (offline) assistance in order to assist the definition of the needle's entry point. Moreover, an intraoperative (online) adaptive planning provides decision-making support considering changes in the path due to the environments' uncertainties. Indeed, the adaptive algorithm allows the planner to improve its own performance under uncertainties conditions, such as tissue deformation, tissue inhomogeneity, topological changes of the tissue and other modeling approximations. The simplified adaptive needle insertion planning has the quality of absorbing the advantages of the model, such as simplicity and ARCS compatibility.

4.2.2.a. Problem definition and formulation

The main goal of this section is the validation of the adaptive slope model. References about preoperative (P) computing is related to the moment before the needle is inserted through the tissue; while online (O), refers to the intraoperative time, when the insertion procedure is in-operation and the needle tip is inside the tissue.

In this subsection, we discuss how each one of these orientation problems was formulated and how they guided the experiments design and the result analysis.

Analysis of Modeling Errors (Pb)

The goal defined by this analysis is stated according to the following problem:

- **Problem (Pb):** “What is the model’s error while predicting needle **tip** deflection regarding to a **linear** path and the **measured** needle tip?”

The model validation is analyzed according to the total (final observed and predicted) needle deflections ($\Delta x, \widehat{\Delta x}$) orthogonal to the initial insertion direction, defined by the segment (\overline{BE}). The simulation is performed preoperatively (P) and online (O). This problem formulation leads us to explore the relationship between the needle tip position observed from the image (N) and the segment (\overline{BEL}), concerning to the linear insertion direction. Therefore, the validation proposed under this analysis, takes into account the preoperative (\widehat{N}_p) and the online (\widehat{N}_o) estimations of (N), having as reference the linear direction (L). The straight-line path is an important reference, since it is often considered by clinicians when no other needle deflection model is available. Finally, in order to obtain the desired error according to Pb definition, the needle itself (N) might to be taken as reference in the analysis. The scheme presented in the Fig. 4.9, illustrates errors and deflections (Δx) analysis according to Pb.

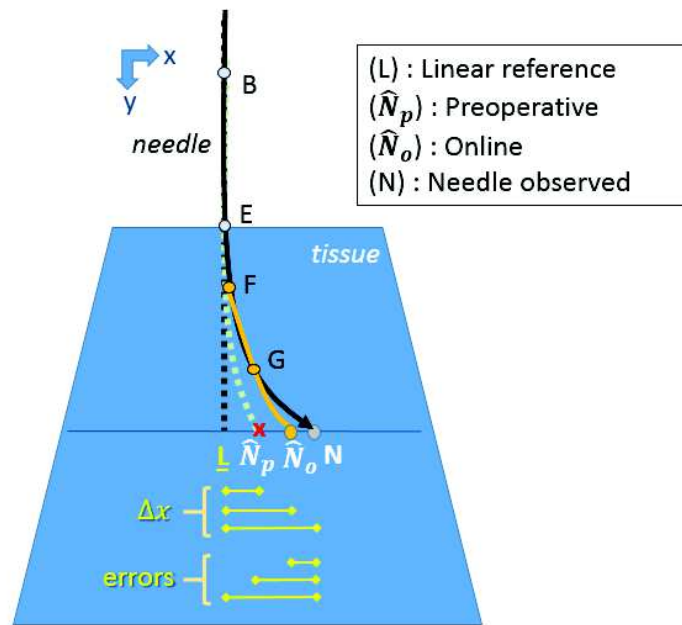


Figure 4.9 - Out of scale illustration scheme, according to the deflection model analysis (Pb).

From the analysis describe above, the errors of the deflection model regarding to L, P and O are respectively defined, for the same insertion depth (Δy), as follows.

$$error(L) = |N - L| \quad (4.1)$$

$$error(P) = |N - \widehat{N}_p| \quad (4.2)$$

$$error(O) = |N - \widehat{N}_o| \quad (4.3)$$

We will present in the next sections experiments performed to validate needle deflection model under needle insertion planning applications. For simplicity’s sake, we used Raven II platform instead of the preconized LPR, during the experiments. It prevented us to compete for the access of scarce clinical resources, such as CT/MRI machines. It also allowed us to evaluate platform independence of our approach. Therefore, its robustness is showed under the uncertainties of an unknown scenario, facing conditions not previously conceived in the model’s confection (*e.g.*, LPR platform-based modeling considers that the needle doesn’t present significant bending outside the tissue – since the LPR’s grippers were designed to be close to the tissue’s insertion point. Example of uncertainties

added to the system occurs when needle bending outside the tissue are observed as result of the use of insertion's mechanism design for different robot platforms, such as Raven II).

Insertion point assistance analysis

The aim of this part is to explain how the planner will assist in the definition of the entry point assistance when a target has been defined by the RI (Fig. 4.10).

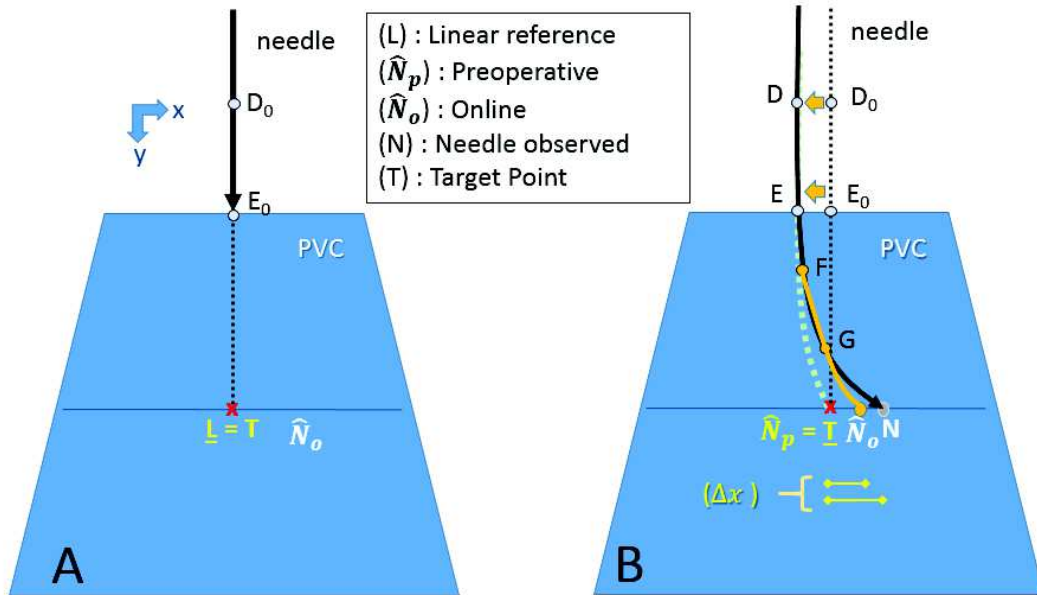


Figure 4.10 - Out of scale illustration of deflections and errors according to the problem formulated to the analysis of the tissue's entry point assistance.

In order to support this analysis, let's see the model application for tissue's entry point assistance, devised under the context of needle path planning. The Fig. 4.10 shows a (out of scale) scheme for the scenario in which the user takes the linear path (L) as reference and places the needle at the tissue's entry point (E_0), targeting the (fixed) virtual point (T). The preoperative planning gives the initial predicted path of the needle (\widehat{N}_p), considering the full insertion through the soft tissue. It could be useful to warn the user about expected errors for such procedure. Hypothesizing that the user decides following classical linear-based planning approach, we would see intermediate online replanning of needle path (\widehat{N}_o) represented in the figure by the points (F) and (G). As mentioned previously, it aims to increase accuracy of predictions concerning the actual needle path and needle tip final position (N) in the end of the insertion procedure.

However, if we take into account the reverse needle deflection estimation provided by the adaptive slope model, assistance to define needle insertion point (E) could be obtained (Fig. 4.10.B).

Indeed, knowing the position (T), we can obtain (Δy) in order to calculate $(\widehat{\Delta x})$. Then, (E) can be obtained in a such a way that makes (\widehat{N}_p) and (T) superposed, according to:

$$E(x, y) = (Tx - \widehat{\Delta x}, 0). \quad (4.4)$$

From now on, the pre-insertion (\widehat{N}_p) prediction has the meaning of target point (T) (and the associated path to reach it). It means that, if the needle is inserted in the predicted entry point (E), then ($\widehat{N}_p = T$); and the needle should reach the target as illustrated in the Fig. 4.10.B. The motion planner also considers that due to the uncertainties of the medium, the actual path of the needle could deviate of the initially planned path. Then, during the insertion, the online (O) algorithm replans the previously planned path (P) to be as fit as possible of the actual needle path. The performance quality in this fitting strategy will allow to the user the best decision making during the insertion, enhancing the procedure safety and avoiding future (predict) damages.

Consequently, if we compare the targeting errors with and without entry point assistance, we will obviously have an error reduction of (E_0E) distance when the needle is inserted from (E) .

4.2.2.b. Experiments Setup

The experiments were performed using the cable-driven (6 DOF + grasp) Raven II robot platform, developed by the University of Washington (Surgical Robotics) (King et al., 2013). It is a state-of-art open architecture (software & hardware) surgical robotic system for surgery research. Its Linux-based operating system allows modifications and improvements of the original code, creating a way for researchers to experiment and collaborate.

For the needle insertion experiments, the robot tools were removed and a customized adaptor was built in order to fix the base of the needle and a force sensor device in the robot's arm (Fig. 4.11).

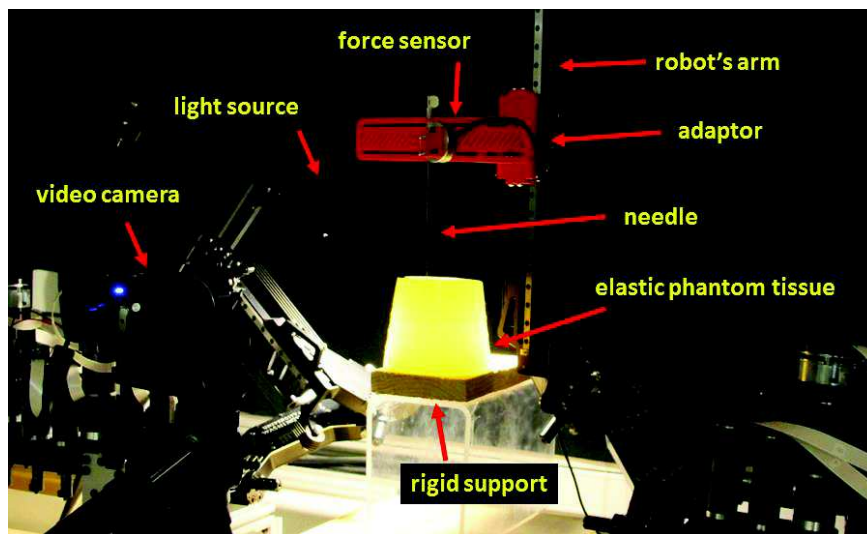


Figure 4.11 - Customized Raven II platform setup.

A long (20 cm), 17 degrees bevel-tip spinal needle was inserted in three different types of synthetic phantom tissues: a) homogenous 100% soft PVC phantom; b) two-layers phantom: extra soft PVC (80% soft PVC + 20% plastic softener) + medium density PVC (70% soft + 30% hard PVC); c) four-layers phantom: (synthetic leather, sponge, soft and hard PVC). This last one intended synthetically reproducing the multi-layer medium usually found in the clinical procedures, such as: skin, fat, mussels and organ.

Video images (1920 x 1080 px) were acquired using a digital video camera Toshiba Camileo Z100 and measurements of the scenario were recovered thanks to accurate camera calibration using planar fiducials markers (Daftry et al., 2013). The needle was visually detectable because the used tissues were translucent. The track of the needle's position was performed manually. It was done by using a single mouse's click in the interactive GUI (4px/mm resolution, more digital zoom (5x)). Manual tracking is classically considered as ground truth to evaluate automatic trackers. Therefore, the tracking accuracy is mainly dependent on the image resolution, as mentioned above. Updates of needle tip position were performed for each insertion step (~30mm depth each one).

The insertions were performed progressively, with regular intervals defined preoperatively. The velocity was of 30 mm/s and, for each insertion step, pauses of 7s were defined in order to wait for tissue relaxation (Fig. 4.12), followed by manual needle tip position update.

For homogeneous tissue, we also observed the system's behavior under insertion velocity of 60 mm/s. In general, for each experiment, there were two pauses, considering insertion depths between 6 and 10 cm. For issue of this validation study, 44 insertion samples at different insertion depths were performed using a digital 12Mpx video camera. A 6-DoF force-torque sensor (nano43 / SI-36-0.5 /

ATI Industrial Automation) was attached to the robot's arm and it was used to record the resulting forces and torques of the system. The force data were used as ground truth and also to enrich the system's study and observations. They were not considered as input in the modeling.

Preoperative parameters were obtained once, without further online updates. They were obtained as described previously (section 3.2.1), Being that the tissues properties (Kt) were found to be $Kt_{(\text{Homog})} = 490 \text{ N/m}$, $Kt_{(2\text{Layers})} = 115 \text{ N/m}$ and $Kt_{(4\text{Layers})} = 130 \text{ N/m}$.

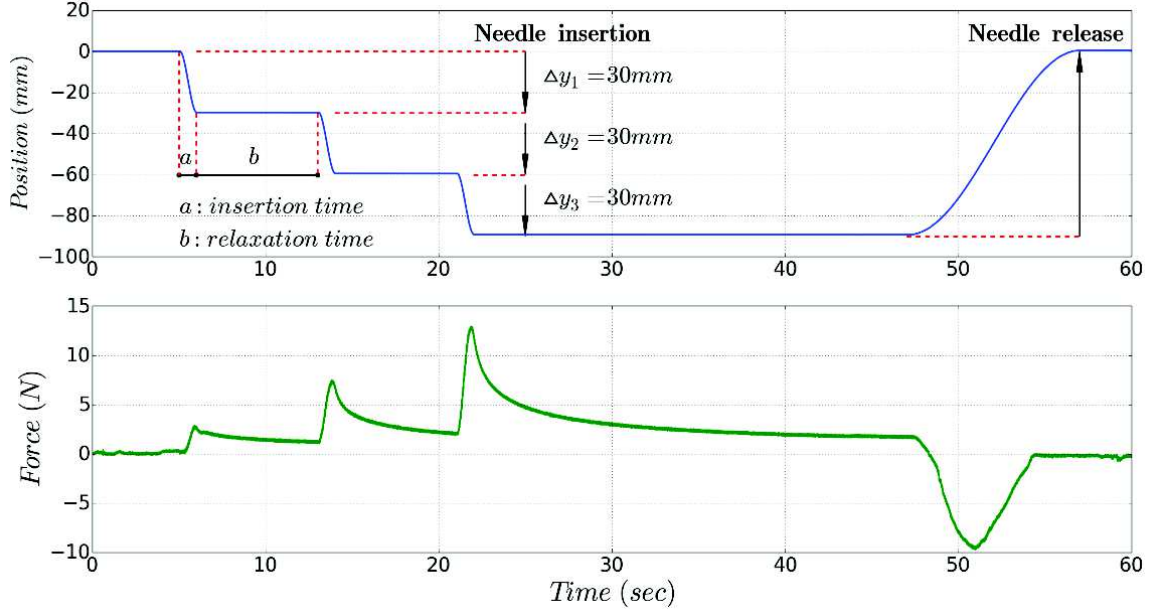


Figure 4.12 - Position and axial force recorded during the percutaneous insertion procedure under homogeneous tissue ($V=30\text{mm/s}$).

4.2.3 Results

We now present the validation results obtained for our simplified adaptive path planning approach, using the definitions and setup presented above.

First, we analyzed the needle's deflection prediction model in the deviations orthogonal to the insertion direction (linear reference), according to the Pb formulation (4.2.2.a). The Fig. 4.13 presents the deviations of (\widehat{N}_p) , (\widehat{N}_o) and (N) , relating them to the insertion depth, considering the set of experiments.

From the linear regression, we observe that for small depth of insertions, (\widehat{N}_o) is closer to the actual needle observations (N) , while (\widehat{N}_p) has its performance quickly improved with the needle insertion depth increasing. This observation reveals that the prediction model has its intra-operation simulation ability (\widehat{N}_o) very dependent to the insertion depth. Besides (\widehat{N}_p) shows excellent results for deeper insertion predictions, (\widehat{N}_o) seems to be very robust with mean errors smaller than 1 mm along all the needle insertion samples.

The reason that (\widehat{N}_p) seems to be more accurate than (\widehat{N}_o) for deep insertion could be explained by the fact the approach defining (\widehat{N}_p) and (\widehat{N}_o) are different. Indeed, (\widehat{N}_p) is calculated offline using only the total insertion depth (Δy) , the initial value of (H) and needle/tissue parameters. However, for calculating (\widehat{N}_o) the algorithm needs more inputs from the user (mouse clicks for instance) to define the intermediate needle position (N_i) allowing parameters update and introducing thus accumulated errors into the estimation. Deeper is the insertion, more updates are needed, bigger is the error.

Additionally, it's possible to see in the cloud of points the definition of two clusters thresholded by the point where (\widehat{N}_p) cross (\widehat{N}_o) , around 70 mm of insertion depth. The presence of these clusters suggests the importance to use (\widehat{N}_o) and (\widehat{N}_p) simulations concomitantly, since the results show that they are very complementary in their performances. For example, the performance analysis of (\widehat{N}_p) for deeper insertions reveals the importance of getting high accuracy in the insertion point definition. It could part of a very efficient strategy to enhance the safety of percutaneous insertions procedures by avoiding damages caused by reinsertions trials or by excessive intraoperative corrections interventions.

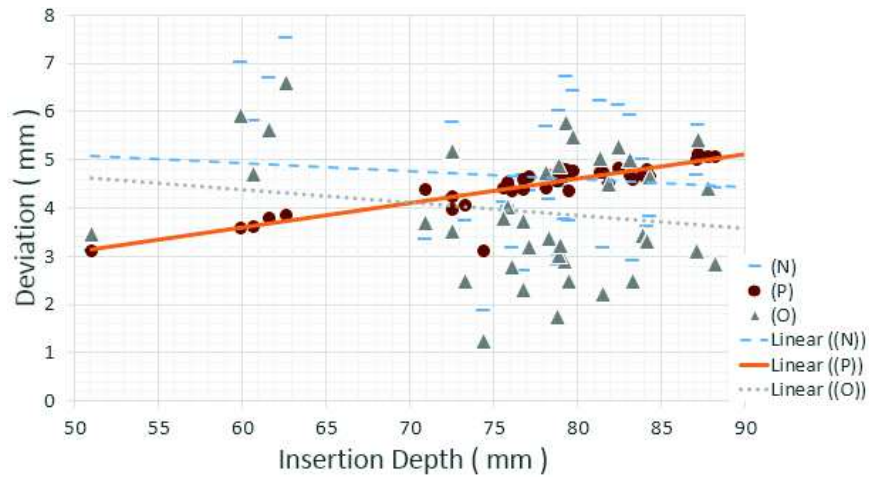


Figure 4.13 - Simplified model validation analysis. Deviations observations under linear referential, according to Pb formulation for several soft mediums.

The errors according to Pb formulation are presented in the Fig. 4.14.

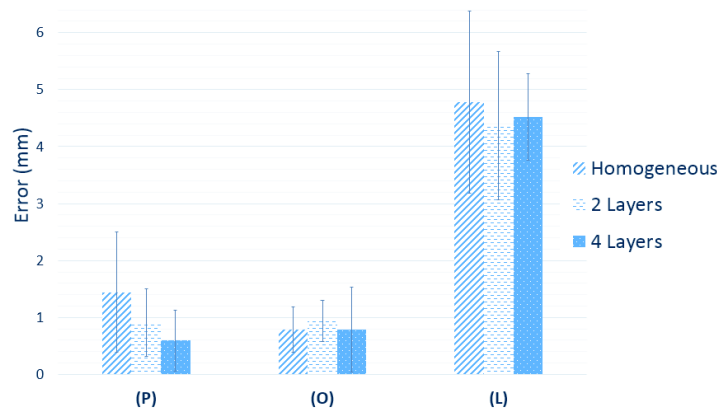


Figure 4.14 - Modeling errors according to Pb formulation, for the several mediums.

The graphs show the analysis taking as reference the actual position of the needle tip. The errors quantification is summarized in the Table 4.2.

Table 4.2 - Summary of the quantified errors according to (Pb).

	(P)	(O)	(L)
Homogeneous	1.44 ± 1.05	0.78 ± 0.40	4.78 ± 1.60
2 Layers	0.90 ± 0.59	0.94 ± 0.36	4.37 ± 1.3
4 Layers	0.59 ± 0.55	0.79 ± 0.55	4.52 ± 0.92

Insertion depths average for homogeneous, two-layers and four-layers phantoms were nearly: 73 mm, 78 mm and 86 mm. The preoperative path planning algorithm (P) had the average error around

1mm and showed good performance for deeper insertions, even under complex mediums insertions (e.g. four-layer tissues). The online replanning approach (O) showed to be very efficient to correct itself, overcoming the scenario’s uncertainties and model’s approximations during the procedure.

The Fig. 4.15 shows insertion sample under homogeneous tissue, after insertion point assistance.

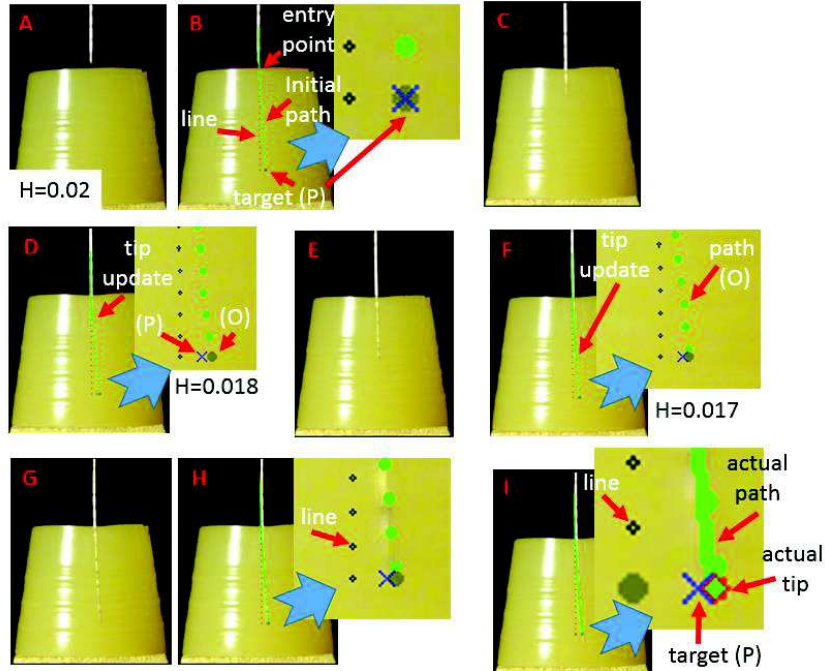


Figure 4.15 - Insertion sequence showing preoperative planning (P) and intraoperative (online) replanning. The adaptive factor (H) updates the expected path and position of the needle (O) for each insertion step.

The insertion sequence illustrates initial needle tip prediction performed preoperatively (P) (Fig. 4.15.B). A sequence of intraoperative (O) path updates (Fig. 4.15.D-F) is performed during the insertion. Then, the Fig. 4.15.H-I show how the system can adapt itself in order to provide a better estimation of the final needle tip position.

The system’s behavior for insertions, for different velocities and similar insertion depths was registered as illustrated in the Fig. 4.16.

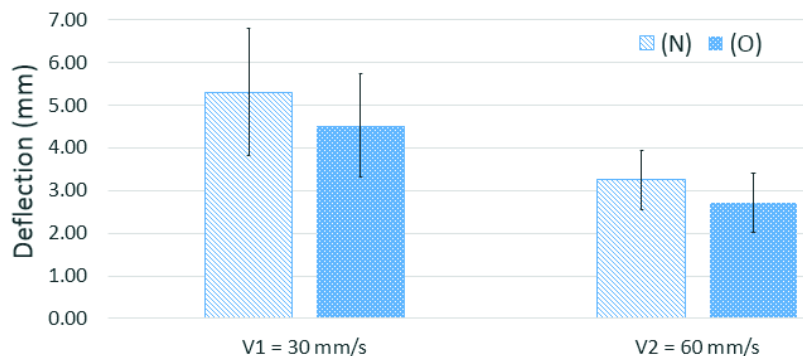


Figure 4.16 - Online adaptive path planning validation analysis. Distance study motivated by Pb2 formulation.

For this experiment, we observed that the bigger is the velocity, less the needle deviates from the (linear) insertion direction. *I.e.*, the needle deflection presented an inverse relationship regarding to the velocity of insertion. However, even considering this important change in the system’s behavior the

insertion planning was robust and stable enough to predict the final needle deviation under submillimetric precision. It was expected during the model's designing, since the model includes kinematical-based parameters, such as needle tip position for each interactive insertion time. That is why, it can compensate for such kinematic variations.

The Fig. 4.17 shows a comparative evaluation of the deflection model through the training and test experiments for estimate offline (preoperative) needle deflection during percutaneous insertion (without needle steering).

As mentioned above, the results are concerning to offline needle deflection predictions, in which no intermediate online adaptive correction is performed (H_0 is kept constant). For training and test experiments, mean insertions depths were 51 mm and 81 mm, respectively. Intra-tissue observations showed a mean difference of nearly 1 mm into homogeneous PVC. In the heterogeneous tissues, the most significant differences were observed in the pattern deviation. The offline results observed in the validation tests reveal the potential of the adaptive slope model to predict needle tip deflections preoperatively considering soft tissue changes.

The differences between results of train and tests were expected due to the intrinsic meaning of the training experiments: In the training experiments, the parameters are tuned according to the experimental samples and it is generally more reduced in number than the test setup. Therefore, it is expected that the results have lower error in this case. In addition, the effects of uncertainties in the test experiments cannot be neglected. As mentioned previously, we observed, for example, that the needle had an important bending outside the tissue during the test experiment due to the way the needle was attached to the robot.

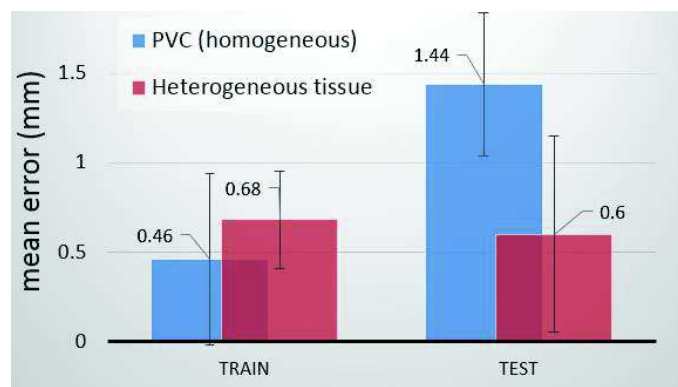


Figure 4.17 - Comparative cross-platform evaluation of the adaptive slope deflection model into the training (LPR, 6 samples) and test experiments (Raven II, 44 samples). Results concern needle deflection for offline predictions (without adaptive corrections).

The Fig. 4.18 shows mechanical differences in the robot's end effectors. LPR's grippers hold the needle very close to the insertion point, while, Raven II robot, the needle fixation point is close to its base.

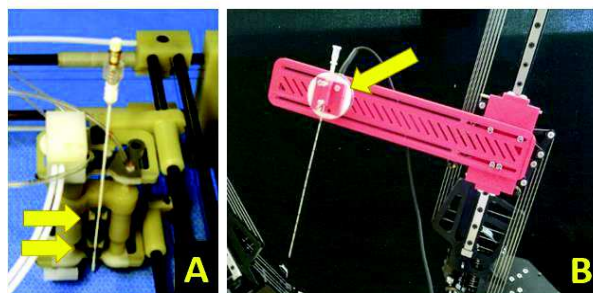


Figure 4.18 - Mechanical differences of the end effectors. A. LPR and B. Raven robot.

Homogeneous soft tissue was observed to provide better results than heterogeneous one, under LPR (Fig. 4.17.Train). The observed inversion in such situation was not expected for the validation tests under Raven II (Fig. 4.17.Test). However, we understand that because the homogeneous tissue was actually stiffer than the heterogeneous, (especially in the tissue entry point), the forces actuating to bend the needle outside the tissue were much more significant. It could influence the original needle trajectory. Such noise was not observed under LPR because the actuators design reduces substantially the impact of such interference.

4.2.4 Discussion

In this section, we presented the development and validation of a simplified adaptive needle insertion planning that uses predictions provided by the needle deflection model as predictor's strategy. Its design was motivated by the constraints of ARCS scenario. The planning algorithm uses the simplified needle prediction deflection model embedded in its strategy and can provide preoperative planning assistance, as well as, intraoperative (online) decision-making support. The prediction model and motion planner algorithm were validated according to the Pb formulation that guided the experiments design and result's analysis.

The deviation analysis of the model showed good performance for the preoperative simulations, especially for deeper insertions. The error analysis showed accuracy smaller than 1 mm for motion planner under intraoperative replanning. Its robustness and consistence were observed when comparing the errors obtained for the several tissues used in the experiments, as well as, when comparing the results considering similar tissues. The approach showed to be very robust when facing the unknown scenario and when adapting itself regarding to the environment's uncertainties, such as a different robot platform and needle's shaft bending outside the tissue.

Our approach has the advantage to be simple and compatible to ARCS. Moreover, it allows appropriated user's action during the procedure, even for the cases where the needle tip is not visible or not available. *E.g.*, RT 3D CT/MR imaging scenarios. It provides useful information at the appropriate moment in order to aid decision-making and enhancing safety in ARCS procedures. For example, in the cases where the needle tip is not visible or not available in RT (e.g. 3D CT/MRI), our planning strategy could enable the appropriated clinical action by supplying simulated feedback of the current needle tip position.

4.3. Needle steering assistance

The previous section presented the development and validation experiments of the adaptive needle insertion planner that uses the adaptive slope model as predictor's strategy. The approach provided preoperative planning to assist tissue's entry point definition as well as, intraoperative decision-making support. In this section, we demonstrate how needle steering assistance and needle tip deflection modeling could improve insertions performance into robot-driven percutaneous interventions. The proposed steering approach is performed by moving the base of the needle perpendicular to the insertion axis, as usually performed by physicians under interventional therapies routine.

We aim to demonstrate the feasibility of merging steering assistance, offline deflection prediction and online adaptive corrections based on the needle-tissue properties, tip asymmetry and needle tip position updates. Experiments protocols were designed taking into account the pilot experiments using LPR. Cross-platform validation tests showed the potential of the needle deflection prediction when submitted to unknown experimental conditions into different scenarios, including different robots, tissues and needles.

4.3.1 Conceptual basis

Now, we present how the needle steering algorithm was devised in order to assist robot-driven percutaneous needle insertion. The core of the algorithm's design is based on the adaptive needle deflection modeling, which was merged in the needle steering approach.

The practical consequence of this enrollment is that inverse and direct application of the adaptive slope model (Eq. 3.9) - with the appropriated play of inputs - was enough to support most of the demands required to develop the needle steering method (Fig. 4.19).

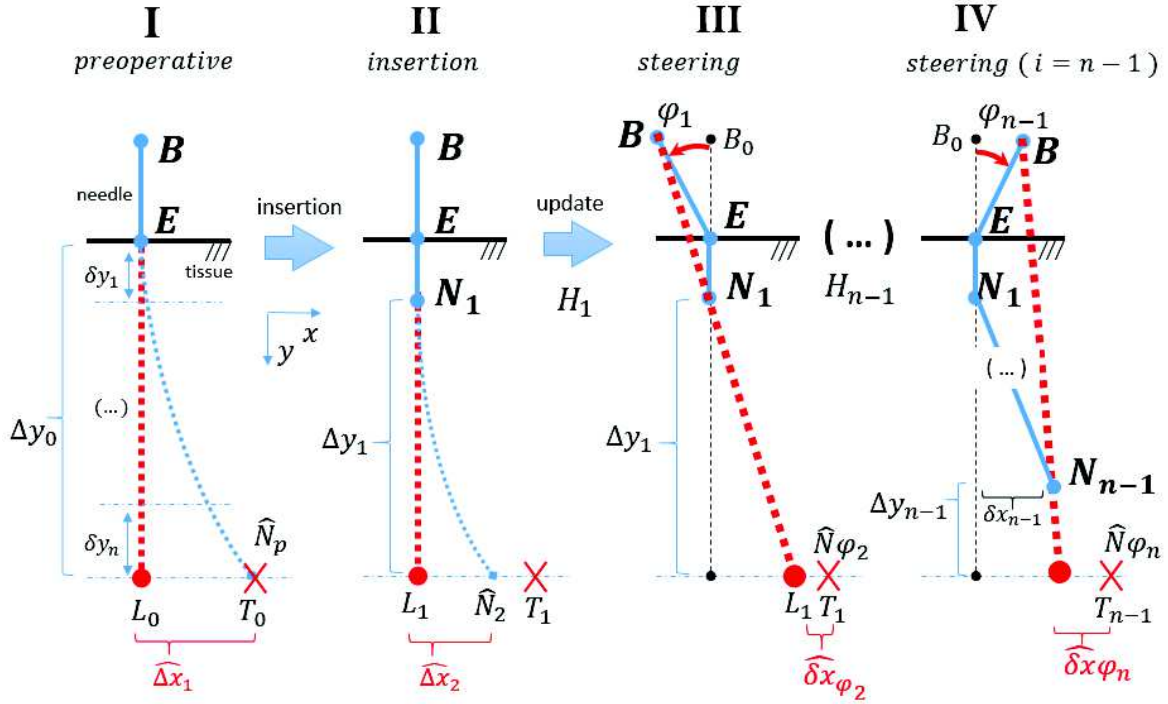


Figure 4.19 - Extended presentation of the adaptive slope model to support needle steering, including the steering angle $\varphi(B, E, B_0)$ as system's input. Inverse and direct model's application, with appropriated play of inputs, supports needle position prediction ($\hat{N}\varphi$), as well as, sequential updates of the adaptive parameter (H_i).

The main difference between the steering algorithm and the standard needle deflection prediction (3.8) is the play of input for online estimation. The steering considers the current (updated) H_i , needle base position ($B\varphi_i$) and needle tip (N_i) to perform the steering prediction, rather than the two last positions regarding to the needle tip (N_{i-1} and N_i). In short, it runs a full depth estimation (Δy_{φ_i}), such as in offline, using the current H_i and needle base position ($B\varphi_i$) and needle tip N_i , rather than H_0 and E. It will be explain in detail as follow.

We explain bellow how needle deflection predictions followed by sequential updates of the adaptive parameter (H) were performed under the context of needle steering. Moreover, we include extended explanation of the adaptive slope model to support the steering angle (φ), related to the lateral movements in the needle base. Finally, we explain how such input affects prediction of needle tip position ($\hat{N}\varphi$), regarding to the previous predictions without using steering (\hat{N}). We assume in the next that, from the moment when the needle is inserted into the tissue, the needle entry point motion under needle-base steering is neglectable. We assume also that the target (T) could move and its position is given by (T_i) at step i .

For the needle steering experiments, the standard needle deflection model is used to assist tissue's entry point definition (E), while providing initial planning of the needle tip position (\hat{N}_0), targeting (T_0) and considering the full insertion depth (Δy) in accord to the scenario base (Fig. 4.19-I).

Classically, considering the needle is inserted at step i , the definition of the full (remaining) deflection estimation ($\widehat{\Delta x}_i$), with respect to the line defined by the needle base (B) and the entry point (E), is related to a points-based linear reference (L_i) regarding to the two last needle tip positions (N_{i-1} and N_i). This method is kept for the steering algorithm. However, for sake of convenience, the representation of linear segment for the deflection prediction parameters related to steering, will be given by the steering angle φ . According to Fig. 4.19.IV, the deflection (Δx_{φ_i}) associated to the full remaining depth insertion (Δy_i) is evaluated using (L_i) as reference. Where the point (L_i) refers to the linear projection concerning to the segment \overline{BN}_i , whose inclination is related to the steering angle φ .

Defining B_0 as the initial base position before steering, the steering angle $\varphi(BEB_0)$ is devised as the space between the differential positions of the needle base (B, B_0), concerning to the lines intersecting in the tissue's entry point (E). The general case, considers a loop of interactions involving needle insertion (i), followed by sequential update of needle tip position.

Fig 4.18-III shows the case where \widehat{N}_i is not correctly superimposed on the position of the T_{i+1} , considered dynamic, due to needle-tissue interactions. For such cases, the steering algorithm, proposes to find a steering angle (φ_{i+1}) in order to provide the appropriated needle path correction ($\widehat{N}\varphi_{i+1}$). It is done using the same H_i , as previously calculated by the update of the last needle tip position.

The new value of the estimated deflection ($\widehat{\Delta x}_{\varphi_i}$), is computed by the deflection model for different values of the steering angle, taking into account an iterative technique that considers several small and incremental pass of steering (φ_k) as candidates to (φ_{i+1}). Considering steering at the time ($i + 1$), the iterative algorithm is implemented to minimize the distance function:

$$\Lambda_{\varphi_k, i+1} = (T_{i+1} - \widehat{N}_{\varphi_k, i+1}), \quad (4.5)$$

where $\widehat{N}_{\varphi_k, i+1}$ is the needle tip position prediction at step ($i + 1$), using the candidate pass of steering (φ_k). Therefore, for each iterative φ_k , a new estimation is performed and, consequently, a new path is predicted (replanning). The loop of the iterative trials is repeated while the estimated error is decreasing or equal to zero. Therefore, the desired steering angle (φ_{i+1}), is given as follows.

$$\varphi_{i+1} \equiv \varphi_{k, i+1} = \begin{cases} k + 1, & \Lambda_{\varphi_{k+1}, i+1} < \Lambda_{\varphi_k, i+1} \\ k, & \Lambda_{\varphi_{k+1}, i+1} \geq \Lambda_{\varphi_k, i+1} \\ k, & \Lambda_{\varphi_k, i+1} = 0 \end{cases} \quad (4.6)$$

The resolution of the iterative steering angle ($\Delta\varphi_k = \varphi_{k+1} - \varphi_k$) is defined by the user in accordance with the capabilities of the experimental platform and to the required targeting error. In our case, $\Delta\varphi$ was set to 1° .

The convergence criterion of the algorithm is achieved when the next steering angle candidate (φ_{k+1}) results in prediction of the needle-target error ($\Lambda_{\varphi_{k+1}, i+1}$) greater than the estimation found in the current iteration k . This means that the predicted deviation ($\widehat{\Delta x}_{\varphi_i}$) is in such a way that the predicted needle position (\widehat{N}_{i+1}) should coincides with the target position (T_i). For such case, the steering angle found in the iteration k is chosen as the best candidate. In general the convergence was obtained after four or five iterative trials, which released very fast results. Moreover, such reduced number of trials (k) stimulate the use of iterative (linear) search technique rather than other more complex approaches (e.g. golden search, random trees, hashes...), since it is well known that they have higher computational cost for limited and reduced problem size (k). The needle insertion approach with needle steering assistance is summarized using the flowchart of the pseudo-algorithm, as available in Appendix C.

Fig. 4.20 shows a sample of real scene of needle steering obtained from 3D reconstruction. The images of the sequential insertions and lateral motion were superimposed to provide sense of motion to the image. The illustrative actions are related to the movements of three sequential moments: a) initial insertion (B_0N_i), with prediction \widehat{N}_{i+1} , after model parameter update ($H_i, Kn_i, \delta y_i$); b) steering

φ_i , concerning to the motion at needle base (B_0B) and update the prediction $\widehat{N}_{\varphi_{k,i+1}}$; and c) final insertion, targeting a virtual T_i .

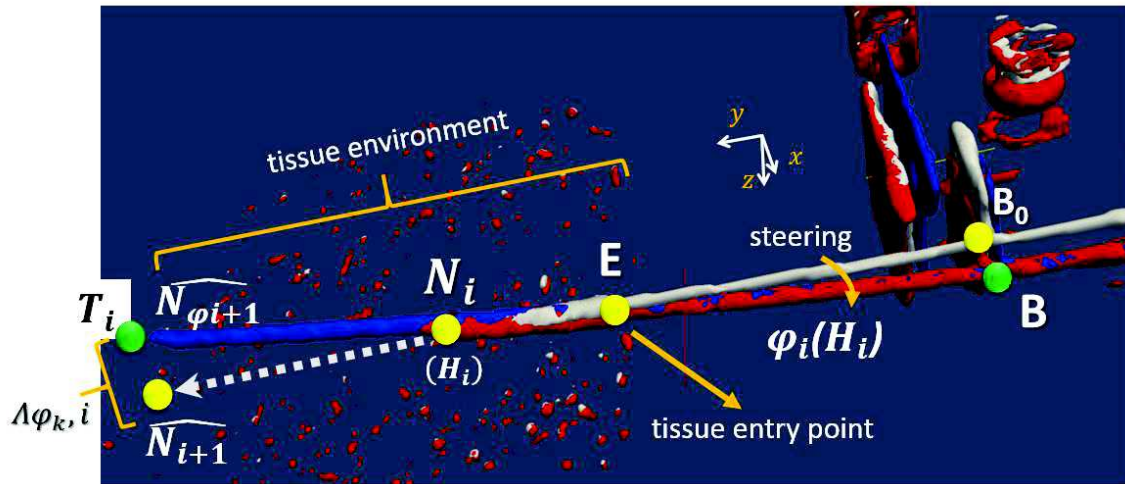


Figure 4.20 - Sample of real scene of needle steering. Sequential motions were superimposed to provide sense of motion to the illustrative image. Movements are related to the sequence of three sequential moments. The steering algorithm computes the steering angle φ_i , in order to minimize $\Delta\varphi_{k,i}$, while targeting the virtual point T_i .

4.3.2 Experimental validation of the steering

The experiments were validated using 39 insertion samples performed using Raven II platform. The robot was commanded by a teleoperation platform (UDP protocol), having the 7-Dof Sigma.7 (ForceDimension) working as haptic master device (Fig. 4.21.B). A Graphical User Interface (GUI) was developed in order to supply online image feedback and procedure data, such as target's depth, current needle-target's distance and needle path, including its estimated error. The Appendix D shows the modifications performed in the DH parameters of the geometric table, in order to control properly the movements of the base of the needle.

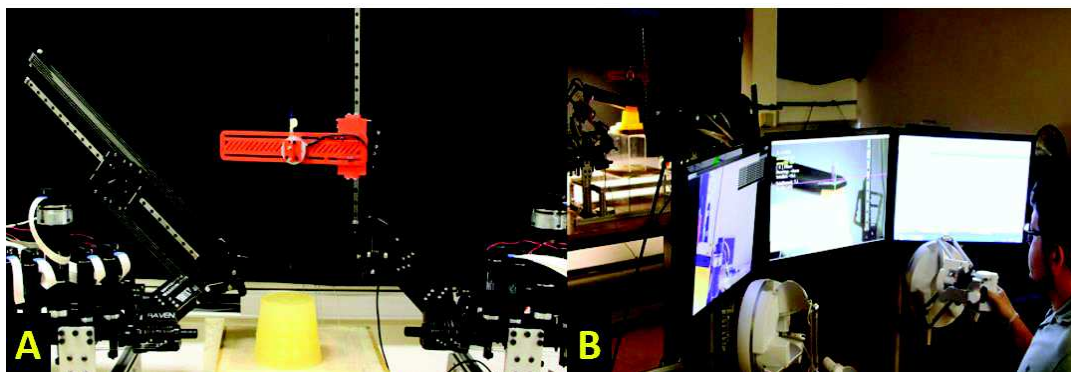


Figure 4.21 - Raven II teleoperation platform customized to perform needle insertion procedures.

As described in previous experiments, images were acquired using a digital video camera Toshiba Camileo Z100, having resolution of (1920 x 1080 px). Measurements of the scenario were recovered thanks to accurate camera calibration using planar fiducials markers (Daftry et al., 2013). The needle was visually detectable because the tissues used were translucent. The track of the needle's position was performed manually. It was done by using a single mouse's click on the interactive GUI. We defined the target as being a virtual point defined by the user with a single mouse's click in the interactive screen. In practice, one can expect target motion due to needle-tissue interaction. However, for sake of simplicity, we considered a virtual target for this first steering validation.

The long (20 cm) spinal needle was inserted in different types of synthetic phantom tissues, such as: a) homogenous 100% soft PVC phantom; b) multi-layer phantom: synthetic leather; sponge; extra soft PVC (80% soft PVC + 20% softener); 100% soft PVC; and 100% hard PVC. The multi-layer phantom tissue intended synthetically reproducing the multi-layer medium usually found in the clinical procedures, such as skin, fat, muscles and organ.

The insertions were performed under iterative-time (Cowan et al., 2011) i.e., progressively, with regular intervals after insertion steps. Each insertion step was around 3 cm of depth. During the intervals (approximately 5 seconds allowing also tissues relaxation), the user could update the current needle tip. The needle tip position updates were used to provide adaptive corrections to the previous needle deflection prediction. The needle steering actions were performed by moving the base of the needle, according to the angle and visual suggestions (based on Augmented Reality resources) indicated in the GUI.

The needle insertion velocity was of 60 mm/s and the depth range between 50 and 100 mm. The 6-DoF force-torque sensor (nano43 / SI-36-0.5 / ATI Industrial Automation) was used for the surface compression tests only once and before start the experiment (preoperatively). The insertion experiments were performed without considering the force sensor data input during the insertions (intraoperatively).

Preoperative parameters were obtained once, without further online updates. They were obtained as described in previous experiments. The tissues properties (Kt) were preoperatively estimated by axial compression test at tissue surface level as in ref (Glozman and Shoham, 2007), having the coefficients $Kt_{(\text{Homog})} = 490 \text{ N/m}$ and $Kt_{(\text{multilayer})} = 130 \text{ N/m}$.

4.3.3 Steering Results

We now present the results of robot-assisted needle steering obtained using the method presented above. The Fig. 4.22 shows images of a real sample of insertion with needle steering assistance into PVC homogeneous tissue.

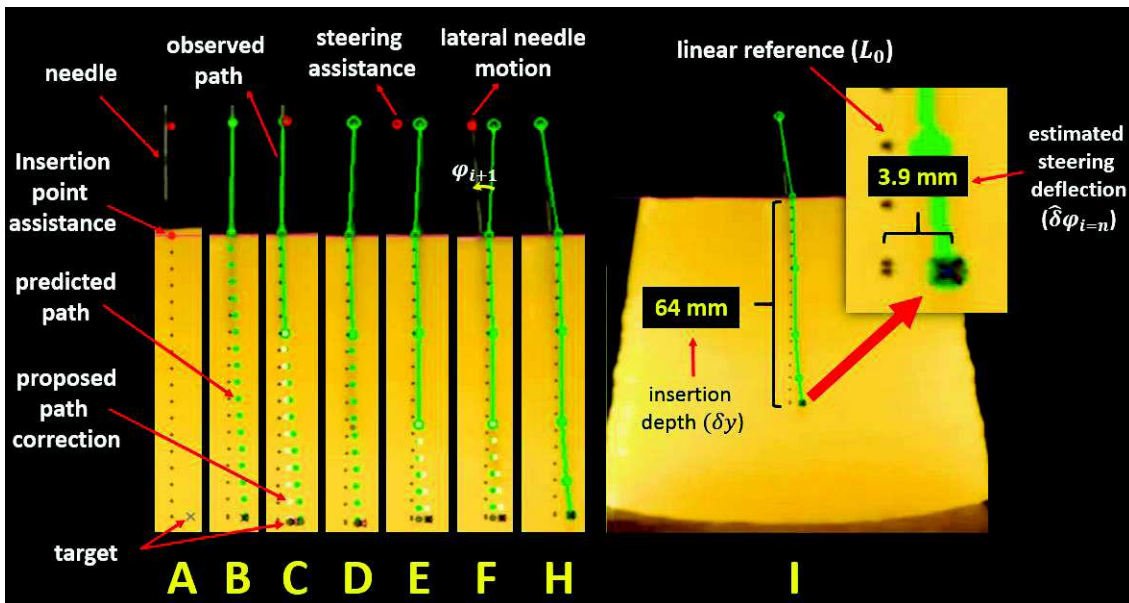


Figure 4.22 - Needle steering assistance with lateral needle motions. Zoom shows in detail visual feedback of the needle path in direction to the target.

Once the virtual target is defined (Fig. 4.22.A), tissue's entry point assistance is provided, followed of offline prediction provides preliminary path prediction (Fig. 4.22.B). Then, a loop of insertion and needle tip updates (Fig. 4.22.C-D), allow the system providing steering assistance (Fig. 4.22.E). When applicable, the path correction is performed by lateral needle motion (Fig. 4.22.F). The procedure ends when the needle and target are under the same depth (Fig. 4.22.H-I).

The assembling of the deflection prediction model with the needle steering, allowed the steering algorithm to take advantage of the online updates of the model. It released intraoperative steering assistance to the user, while taking into account the uncertainties of the scenario. The robustness of the adaptive slope model integrated into the steering algorithm can be observed in the Fig. 4.23.

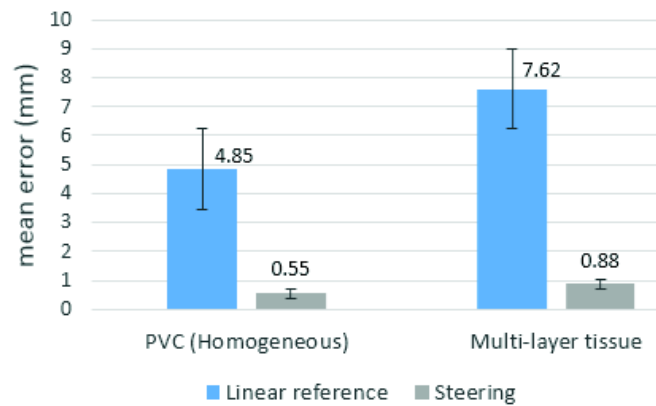


Figure 4.23 - Results of needle steering approach compared with linear-based clinical reference.

The graph shows a mean targeting error of 0.55 ± 0.4 mm and 0.88 ± 0.3 mm for PVC (homogeneous) and heterogeneous phantom tissues, respectively. For the steering experiments, the mean insertion depth was nearly 98 mm, with a tip deviation up to 10 mm regarding to a linear reference. The robustness of the steering approach for the intra-tissue evaluation is also confirmed by the small variations of the pattern deviation. Moreover, it was very stable when comparing inter-tissues errors. Finally, when we compare the targeting errors of offline predictions (without the steering corrections) using Raven II (Fig. 4.17.Test), it is possible to observe the efficacy of the steering algorithm in reducing errors to submillimetric levels (Fig. 4.23).

The results presented in this section showed the accuracy and the targeting robustness of the adaptive slope model when combined to the needle steering algorithm and using Raven II platform. These experimental results encouraged us to program and perform ex-vivo validations with the LPR robot under CT guidance. Bellow, we will discuss in detail system's behavior under CT-guided LPR-driven needle insertion scenario.

4.3.3.a. 3D Needle Steering using LPR

The needle steering algorithm has been tested using LPR (Arli prototype) into ex-vivo pork tissue. The experiment setup was identical to the one described into the preliminary experiments (Section 2.3) using CT scanner. However, beyond to test needle steering under non-homogenous tissue, we designed the experiment considering changes under four other aspects: a) use of LASTIC device; b) use of physical target; c) use of different needles; d) needle steering performed under 3D scenario. They will be presented below.

LASTIC: LASTIC (Schiavone, Promayon and Payan, 2010) is a light aspiration device for *in vivo* soft tissue characterization. It operates by applying a range of negative pressure in the lower compartment while measuring the resulting aspirated tissue deformations with a miniature digital camera. Suction is modelled using FEM that uses the measurements to estimate tissue elasticity parameters. It was used rather than force sensor in order to estimate tissue properties at the surface level (Fig. 4.24).

Therefore, it was possible to observe the behaviour of the system when submitted to a force sensorless scenario that could be compatible with MRI context. Measurement of tissue deformation concerned to the quasi-static negative pressure applied over the tissue surface was made before to start the experiment (preoperatively). It allowed us to find the value of 0.21 GPa for Kt , close to the 0.3 GPa previously found using force sensor using a different *ex-vivo* tissue sample (3.1.1.a).

Physical target: A screw-nut (5 mm of diameter) was inserted inside the pork through a path orthogonal to the insertion direction. It was used as physical target during the experiments and it was distant nearly 87 mm from the tissue surface.

Needles: Two different needles were tested. The first needle was the standard one (18G) as described in all the previous experiments. The second needle was a (20G) stainless needle with 38 degrees of bevel tip and outer diameter of 0.9 mm. Because the needle was compact, inner diameter was set to zero.

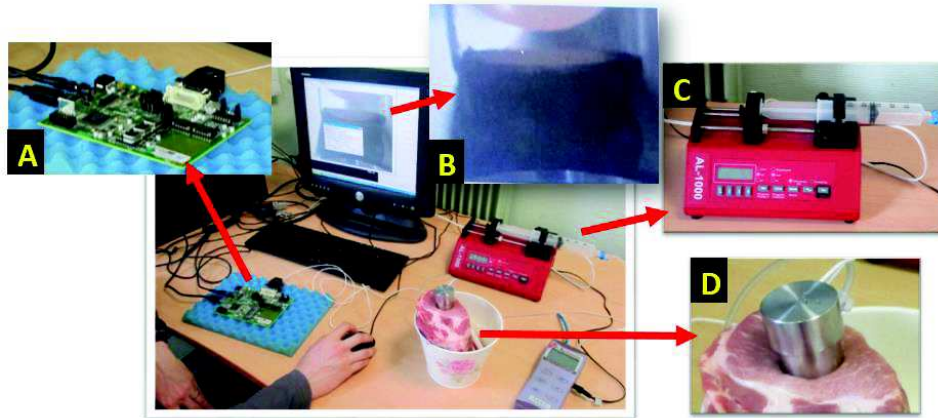


Figure 4.24 - LASTIC device used for preoperative measurement of stiffness at tissue surface level. A. Control and communication card. B. Visual feedback of tissue deformation due to the quasi-static suction forces. C. Negative pressure control and measurement mechanism. D. Suction device with camera and ex-vivo pork tissue.

Three samples of full needle insertions using adaptive insertion planning with steering and tissue's entry point assistance were performed using *ex-vivo* pork tissue. Additionally, one free (open loop) insertion was done in order to observe needle deflection compared to a linear referential. One insertion was performed using the standard needle (18G) and two insertions were done using the thinner and more flexible (20G) needle.

3D Scenario: The robot-driven insertion experiment was performed under CT-guided scenario. CT image data is interpolated over the scanned workspace volume. Slices view of the orthogonal axial and sagittal planes provides 3D feedback of the scenario (Fig. 4.25).

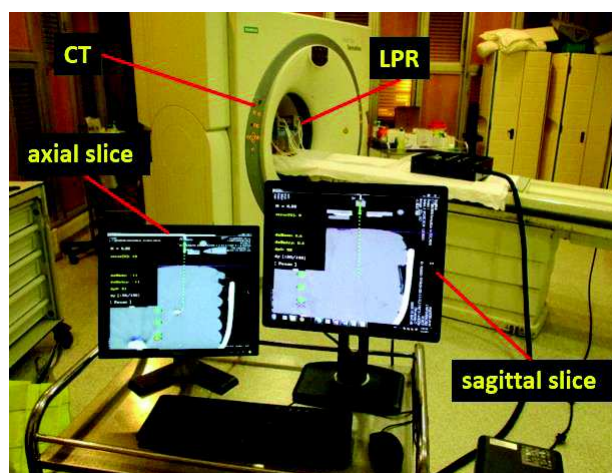


Figure 4.25 - Experiment setup for 3D needle steering using LPR and CT scanner. Axial and sagittal images slices were used to provide needle position feedback and online needle steering assistance during the insertion procedure.

The final 3D error (\mathcal{E}) was obtained using Euclidean distance between needle-targeting errors observed for either, axial and sagittal 2D slices.

$$\mathcal{E} = \sqrt{(Nx_{axial} - Tx_{axial})^2 + (Ny - Ty)^2 + (Nz_{sagittal} - Tz_{sagittal})^2} \quad (4.7)$$

Where $N = (Nx, Ty, Nz)$ is the actual needle position at the same insertion depth (same y -axis) of the target point T , chosen by the user in the center of the target surface. Because relative needle-tip position are observed under the same insertion depth, we assume $|Ny - Ty| = 0$.

The steering system used the (pixel/voxel) resolution obtained from the DICOM images in order to estimate dimensions of the objects in the scene, while providing steering assistance to the user. Since the needle and tissue were present in the same image, the system was able to provide steering assistance using movements relative to the current position of the needle, observed for each slice in the GUI.

Because we worked under 3D scenario, often we could not see the full set of the needle fiducials in every slice. In order to solve this problem and being able to identify the main objects in the scene, the GUI used resources based on Augmented Reality (AR). Then, the steering system could identify the position of the fiducials for each 2D plane even if they are not being sliced in the current GUI windows with the visual feedback. The Fig. 4.26 shows several axial slices providing fiducials such as needle base (B), needle entry point (E), intermediate and current positions of needle tip (N_1, N_2) and physical target (T).

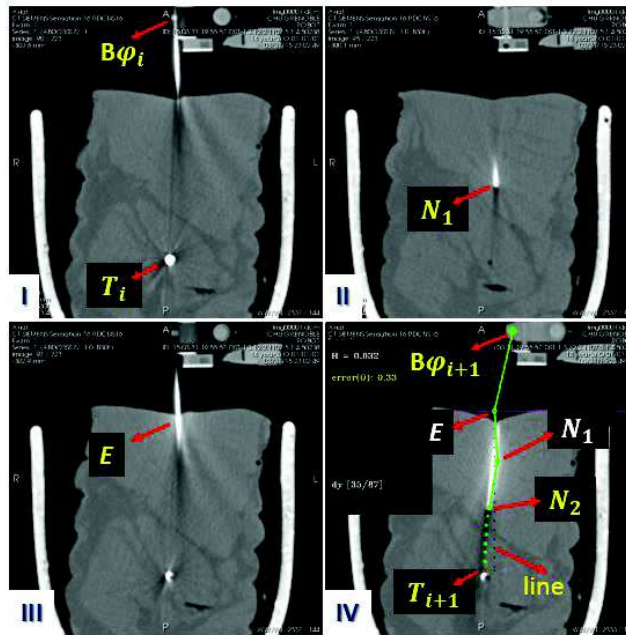


Figure 4.26 - Interactive GUI with AR-based resources. Often, the full set of the needle's fiducials were not entirely visible in every slice (I-III). AR-based resource (IV) improved visual feedback to the user by assembling all the fiducials into a same visual plane. GUI also provided feedback of system's parameters, such as $H, \hat{\epsilon}_i, \delta y(\delta y_i/\delta y_0)$ and ϵ_{n+1} .

Figures 4.26.I-III show main fiducials regarding to the time (i), presented in different planes. Fig. 4.26.IV refers to the time ($i + 1$) and shows GUI with main steering parameters ($H, \hat{\epsilon}_i, \delta y(\delta y_i/\delta y_0), \epsilon_{n+1}$) and AR resources being used in order to plot all of them in the same plane, regardless of the 2D image slice in the background. $\hat{\mathcal{E}}$ is the error estimated by the system, concerning to the predicted needle position \hat{N}_{i+1} and the current target position T_i .

The Table 4.3 shows the errors obtained during the experiments using LPR and 3D CT images.

Table 4.3 - Example of targeting errors obtained during experiments using the needle steering approach (S) with LPR and 3D CT images. Last row (L) refers to the needle deflection regarding to the linear reference, during free (open-loop) insertion.

Sample	needle	error (mm) (axial plane)	error (mm) (sagittal plane)	3D error (mm)
1 (S)	18G	0.3	0.30	0.42
2 (S)	20G	0.3	0.67	0.73
3 (S)	20G	0	0.3	0.30
4 (L)	20G	2	11	11.18

The average of the 3D errors for the three samples was 0.49 mm. The last sample showed in the table (L), refers to the observed needle deflection regarding to a linear referential, considering a free insertion (without steering or targeting goal) as could be performed manually without assistance. We performed such experiment in order to obtain a linear referential for the current needle-tissue setup, considering the same insertion depth (87 mm). By using the 20G/20cm biopsy needle interacting with *ex-vivo* pork, we observed needle deflection regarding to the linear referential in the order of 11.18 mm. Compared to the three previous robotized steering assisted experiments, we have obtained more than 95% of error reduction. In addition, it is important to mention that the experiment was run in the limit of the constraint condition ($\delta x/L < 0.1$). Even though, it was able to converge the predictions to provide errors bellow 1 mm.

4.3.4 Discussion

This section presented a novel semi-rigid needle steering method combining steering angle in the needle base, offline prediction and online adaptive correction. The method was based on the needle-tissue properties, tip asymmetry and needle tip position updates. Its design was motivated by the constraints of ARCS scenario, in accord to the challenges imposed by the clinical potential of the LPR robot platform.

The protocols proposed to the present study were influenced by preliminary observations made from 3D CT images of the needle-tissue interactions using LPR robot. The needle deflection model was based on the study of an adaptive slope parameter and can perform offline and online needle deflection predictions. Its robustness was evaluated into an extended cross-platform robot-assisted experiment, facing challenges not previously conceived in its design, such as needle bending outside the tissue. Training and test experiments results were compared regarding to offline needle deflection predictions. The offline results reveal the potential of the adaptive slope model to predict needle tip deflections preoperatively, even considering tissue changes. Lastly, the model was integrated into an adaptive needle insertion planning approach with online needle steering and offline tissue's entry point assistance. The needle steering algorithm reduced the errors of the offline predictions. The overall performance and robustness showed in such experiments serve to validate the potential of the proposed steering approach. Offline predictions followed the trends of experimental data observations.

The steering approach took into account the needle-tissue properties and provided online adaptive improvements. During the validation tests, the algorithm was able to adapt itself automatically regarding to the scenarios in the different platforms, i.e., without needing any further experiment for (re)training or (re)tuning. The use of the needle steering assistance reduced the error of the needle insertion in the order of 95% when compared to the insertions using the classical linear reference.

For simplicity's sake, experiments used devices such as force sensor or LASTIC in order to obtain the tissues' parameters offline. Optionally, Kt could be measured by using others tools, such as MRI elastography or Acoustic Radiation Force Impulse (ARFI) (Moreira and Misra, 2014). Moreover, the results obtained in this study are related to the measurement of Kt in the tissue's surface. For each used tissue, such preoperative parameter was measured only once and before starting the procedure (offline). After that, no input force measurements or updates of Kt are performed and all the predictions and further adaptive compensations are based on the online position updates of the needle tip. The design of the approach as it is, suggests its potential compatibility with constraints of MRI scenario (i.e., measurements of tissue's parameters could be performed immediately before the patient go inside the MR room).

Although it is very difficult to compare methods proposed for different experimental conditions, it is interesting to notice the range of context, needle type, feedback approaches, targeting errors and their potential compatibility with actuators of current ARCS robot platforms. The Table 4.4 shows the main approaches available in the literature proposed to assist robot insertions. These works have been present previously in this thesis, however it is a non-extensive reference.

Table 4.4 - Needle steering and deflection prediction approaches proposed for different experimental conditions. Some information in the table may be not directly available from the study. Therefore, when applicable, it was deduced (*). For the case in which the information is not applicable or not clearly available in the article, it was set as (n/a).

Model	Target context	Needle type	Tissue	depth (mm)	steering approach	feedback approach	Prediction		ARCS	adaptive failure contingency	online force input	claimed mean error (mm)
							pre	intra				
Wan, 2005	brachytherapy	rigid rod (stainless steel)	ex-vivo (chicken)	60	axial/spin rotation	US		X			sensor	2.8
Rucker, 2013	abdomino-pelvic (liver*)	flexible (nitinol)	a) deformable phantom; b) ex-vivo bovino liver	a) 85 b) 100	axial/spin rotation	magnetic tracking		X			sensor	a) 0.5 b) 0.4
Moreira, 2014	neurosurg. brachytherapy (*)	flexible (nitinol)	a) 2-layer gelatin; b) ex-vivo (chicken); c) ex-vivo + target mov	90	axial/spin rotation	US	X	X			sensor	a) 0.42 b) 1.56 c) 1.63
DiMaio, 2005	brachytherapy*	semi-rigid (stainless steel)	soft PVC stiffness variations: a) 15% b) 50%	n/a	lateral movement	video		X	X		sensor	a) 1.0 b) 2.5
Kobayashi 2009	abdomino-pelvic (liver)	rigid rod* (stainless steel)	deformable liver model	60*	n/a	US	X	X	X		n/a	1.5
Glozzman 2007	laparoscopy	semi-rigid (stainless steel)	a) ex-vivo (turkey); b) ex-vivo (beef);	40	lateral movement	fluoroscopy	X	X	X		sensor	0.5
Our model	abdomino-pelvic (kidney)	semi-rigid (stainless steel)	a) soft PVC (homog); b) multi-layer phantom; c) ex-vivo pork	50-100	lateral movement	CT; video	X	X	X	X	free	a) 0.55 b) 0.88 c) 0.49

The table classifies the works according to the target context, types of needle and tissues, depth of insertion during the experiments, needle steering methodology, modality of imaging feedback, type of deflection prediction: *i.e.*, preoperative (offline) x intraoperative (online), promising approach's compatibility with currently existent ARCS-based robot platforms (*e.g.*, compatibility with CT/MR imaging and semi-rigid needles classically used in the clinical routine), failure-contingency mechanism: adaptive compensations of the model to improve online its own performance due to scenario uncertainties; required demand for online data force input and claimed mean error.

According to (Rucker et al., 2013), 2–3 mm errors could be tolerated by most surgical needle placement procedures, being that the human manual placement error is approximately 3–5 mm (Boctor et al., 2008). Therefore, overall, the submillimeter targeting error results from most of these experiments serve to validate their proposed control approaches. However, as seen in the table, the main challenges for the use of robot-assisted needle steering approaches go beyond the targeting error quantifications.

The choice of using of flexible (nitinol) or semi-rigid needles can restrict the feasibility of the applications to the robot platforms existent into a given scenario. Similarly, choosing a model over another may condition online deflection predictions to the previous integration of non-metallic force sensors compatible with MRI-guided context. The issues mentioned above limit or make difficult the use of many of these models under ARCS. The experimental results presented in this thesis reveal the potential of our approach to fill this blank.

The current implementation of the needle steering system does not include active target motion compensation. Even though, the results were very accurate regarding to the use of real target. Two main factors may be contributed to that: a) According to the observation presented in the preliminary experiments, movement of the tissue due to needle's interactions are reduced for greater insertion depths. Therefore, the target motion seems to be much reduced at such regions; b) The sequential updates of needle tip and target positions work in the practice as a passive compensation mechanism for target's displacement, regardless of the insertion depths. It means that such intermediate inputs allows the model incorporating the current target displacement to the replanning, which now, will steer the needle in accord to the new target position.

Future works could investigate how online updates of Kt would impact the performance of the model. Techniques as elastography could support the preoperative build of a 3D stiffness map that could be used as online input source of Kt parameter, according to the current needle tip position updates. Moreover, assisted-guidance provided by haptic feedback could be explored in order to investigate the advantages of human-in-the-loop steering systems and their accuracy impact compared to automatic robot steering.

Our study has demonstrated the feasibility and advantages of merging online and offline deflection estimation to perform semi-rigid needle steering with promising ARCS compatibility.

4.4. Conclusion

This Chapter provided comprehensive description of the ARCS-compatible teleoperation robot platform proposed to perform the full range of percutaneous applications (*i.e.*, translation, orientation and insertion). In addition, we presented in detail the conception, development and evaluation of a robot-driven needle insertion system that can provide intraoperative adaptive insertion planning with needle steering and preoperative tissue's entry point assistance.

The main contribution of this chapter is the design and validation tests for a robot-assisted needle steering system truly based on the needle adaptive slope model presented previously in this thesis to support needle deflection prediction during its insertion into soft mediums. We applied perpendicular motions in the base of the needle to steer the needle. A novel algorithm was designed in order to support the user providing visual assistance feedback.

We have proposed the use of a phenomenological approach based on position of the needle tip and target, but also into biomechanical properties of the needle and tissue. Design of experimental validations provided offline and online adaptive needle insertion planning and needle steering assistance during percutaneous procedures.

The adaptive parameter H has been preliminary studied and identified for a 17° bevel tip needle. However, as shown in Section 4.3.3.a, we used a 38° bevel tip needle and got interesting results thanks to the adaptive approach of our model.

The advantage of using this approach is its potential to be used into clinical ARCS scenario and it is compatible to the mechanical constraints of LPR. Obtained results from experimental validations reveal its adaptive ability to overcome challenges imposed by scenario's uncertainties and model's approximations, while improving online its own performance. Finally, experiments have showed potential of the approach to be extended to other robot platforms.

Chapter 5.

General Conclusion

5.1. Thesis' summary

The introduction of teleoperation robot-driven systems into IR procedures can significantly improve the effectiveness and safety of medical interventions. The recent advances in CT and MRI-compatible robotic platforms release promising opportunities to reduce the procedure time, avoiding radiation to the clinician and promoting more comfort to the patient. As a consequence, performance and consistency of needle insertion assistance - especially in terms of needle deflection prediction, needle insertion planning and steering - are mainly dependent on the platform and scenario at hand.

We have discussed the design and validation of image-guided robotic-driven percutaneous interventions. A number of aspects were discussed, including basics of IR, its concepts and advantages, limitations of current procedures used under the conventional routine, ARCS constraints, main ARCS-compatible state-of-art robot platforms, state-of-art studies and observations on needle insertions, background on needle deflection modeling and its main applications, such as tissue's entry point assistance, adaptive needle insertion planning and needle steering.

Development and feasibility experiment of a teleoperation platform for LPR was presented, including main aspects of its modular architecture, and navigation system (including GUI and state machine). The platform was proposed according to the modularity principles encouraged by CamiTK. A Montpellier-Grenoble online demonstration was designed in order to provide assistance for insertion planning emulating the constraints of a CT-guided teleoperated scenario. A radiologist was able to easily advance through all the phases of the system guided by the interactive interface. The coupling GUI + state-machine showed to be promising to improve system's usability.

Two robots, LPR and Raven II were used into applications involving insertion of semi-rigid needles through soft mediums. Their particular kinematics led to different experiments' settings. They each present their own challenges that covered the large spectrum of design and evaluation constraints outlined in Chapter 3 and 4.

The use of lateral movements in the needle base are recovered, as previously proposed in the robotic-assisted needle insertion literature and it is proposed to steer the needle path. Such movement follows the patterns of established procedures already used in the clinical scenario (manual insertions). It increases the potential of using this approach into the clinical context. Experiments observations showed that the use of the surgical drape during the procedures promises to reduce the force applied over the tissue surface, reducing risks of tissue tearing. Moreover, since tissue's entry point was

General Conclusion

considered fixed during the modeling, the use of surgical drape during LPR insertions may have contributed to reduction of model's approximation.

Needle fixation was explored differently in both systems, with LPR grippers fixing needle close to the tissue's entry point and the Raven holding the base of the needle. However, we have to emphasize that the proposed model was developed independently from any robot design. Indeed, even if the model was initially developed under the constraints of the LPR robot environment, it was then tested, without any parametric retuning between experiments under the novelties of the second scenario (Raven-II platform). This, including needle deflection outside the tissue, and differences in the visual resolution with consequent input resolution of needle tip position feedbacks provided by the user.

Finally, beyond of the different robot platforms and image modalities, the system was also evaluated in an experiment setting on different synthetic and ex-vivo phantoms, in particular with respect to their targeting assistance accuracies. Online and offline error of each application of the system was analyzed, including needle deflection prediction, tissue's entry point insertion assistance, adaptive needle insertion planning and steering. The system accuracies showed for both robot platforms fell within the technical goals set at the onset of the project.

5.2. Final discussion

Preliminary experiments under LPR have proved crucial contribution to understand the main constraints involved into the conception of the ARCS-compatible needle deflection model. Complexity of the scenario (*e.g.*, MRI's ferromagnetic issues) and possible limitations expected in the clinical routine (*e.g.*, lack of compatible force sensor, while online force data is often required by classical needle deflection modeling), were included as part of the input assumptions in the study's design.

Beyond kinematics-based (*i.e.*, insertion depth, needle tip and target positions) and biomechanics-based parameters (*i.e.*, needle tip asymmetry and needle/tissue stiffness), modeling design has included an adaptive factor (H), that works as a failure-contingency mechanism, allowing to the model improving online its own performance regarding to the environment uncertainties. Such advantage was exploited to maximize robustness of online model's applications such as intraoperative needle insertion planning and needle steering assistance.

Simulation results supported model's training against empiric data (open-loop insertions), obtained from preliminary LPR experiments. Such offline approach led to the practical meaning concerned with the estimation of the initial value (H_0), supported by heuristic technique. During the training tasks of the same needle insertion into different tissues, the adaptive value successfully converged to a constant value when the empirically measured needle tip deflection was provided preoperatively as model's input. Results showed very low standard deviation, which confirmed the potential of the parametrical set used in the modeling. Such finding was a preliminary evidence of the modeling's ability to predict offline needle deflection along percutaneous procedures using LPR. Task concerned to the definition of the initial H 's value (H_0) was strictly necessary to provide the sought offline predictions, which in turn have been involved into the design of applications as preoperative needle insertion planning and tissue's entry point assistance.

Although H_0 was fitted during training using LPR platform, results of empirical tests validated the approach, considering intrinsic mechanical differences of Raven II. Actually, we observed, for both platforms, that the deeper was the insertion, more the offline predictions converged to more accurate results (Fig. 3.19 and 4.13). We did not expect so. Therefore, for the purpose of better understanding such behavior, a couple of hypothesis was identified, as presented in the Table 5.1.

Although the exact cause of such behavior is difficult to be accurately proved, we thread a falsifiability-based discussion (Popper, 1934), which pursues the best hypothesis on disproving less likely candidates, so that we could check out what is left.

Firstly, we have rejected hypothesis I (needle bending outside the tissue), because such behavior was considered not significant under LPR, while the convergence was observed in both experiments.

Table 5.1 - List of hypothesis identified as candidate causes of model's convergence for offline predictions.

#	Hypothesis	Description
I	Needle bending outside the tissue	Needle trajectory under deeper insertions could be less sensitive to noises whose source is outside the tissue. Therefore, it could justify more predictive answer of the model under deeper insertions.
II	Tissue's relaxation	Smaller intensity of tissue's movements were observed for deeper insertions, even for homogenous tissues (section 3.3). Such different elastic behavior along to insertion depth, could impact over the model, whose stiffness is measured only under tissue's surface.
III	Internal tissue's deformation	
IV	Tissue's surface deformation	In the beginning of the insertion, it could produce some (non desired) impact in the needle insertion direction, and the effects would be reduced for deeper insertions.
V	Input noise concerning to needle length (L)	Reason (L_{out}/L_{in}) could be source of input error when estimating needle stiffness (Kn). If so, such error could have more impact in the beginning of the insertion, when such reason is higher ($L_{out} > L_{in}$). Then, it would be relieved along the insertion depth, since ($L_{in} \gg L_{out}$). Where L_{out} is the needle's shaft outside the tissue and L_{in} , the needle's shaft inside the soft medium.

Secondly, hypothesis II and III have been equally discarded by the fact that exclusive measurements in the tissue's surface should affect negatively the model's behavior. I.e., the model should be more accurate in the beginning when the needle tip is close to the region where the tissue stiffness was better defined.

We also have rejected hypothesis IV by the fact that, actually tissue deformation is already included in the modeling. Therefore, we understand that such effects in the tissue's surface should be absorbed by the prediction. Moreover, similarly to the discussed in the previous paragraph, tissue's stiffness measured at tissue's surface, should make the predictions better in the beginning and not the opposite.

Finally, we have the discussion about the hypothesis V. It was proposed based on the fact that the needle deflects in function of the length of the needle's shaft that actually interacts with the soft medium (L_{in}). However, needle's stiffness input $Kn(L)$ must be calculated using ($L = L_{out} + L_{in}$), in order to assure realistic values of Kn . It has the practical meaning of introducing a noise in the system.

The Fig. 5.1 shows analysis of the reason (L_{out}/L_{in}) applied for both robot platforms. Indeed, it supports the description as proposed by the hypothesis V, in which the noise seems to be much more relevant in the beginning of the insertion ($L_{out} > L_{in}$).

Then, as the needle goes through the soft medium, the noise shows its importance be reduced, since ($L_{in} \gg L_{out}$). Although we cannot accurately prove that the hypothesis V is the true, the discussion presented above let us believe that between the identified reasons, it seems to be the most pertinent one.

General Conclusion

In addition to the analysis devised above, we could include another reason that could work in parallel to the reason mentioned above.

Sum of user's input errors: The preoperative predictions are calculated offline without any user input. While for calculating the online prediction the algorithm needs more inputs from the user (mouse clicks for instance) to define the intermediate needle positions allowing parameters update. This introduces and thus accumulates errors into the estimation. Deeper is the insertion, more updates are needed, bigger is the error.

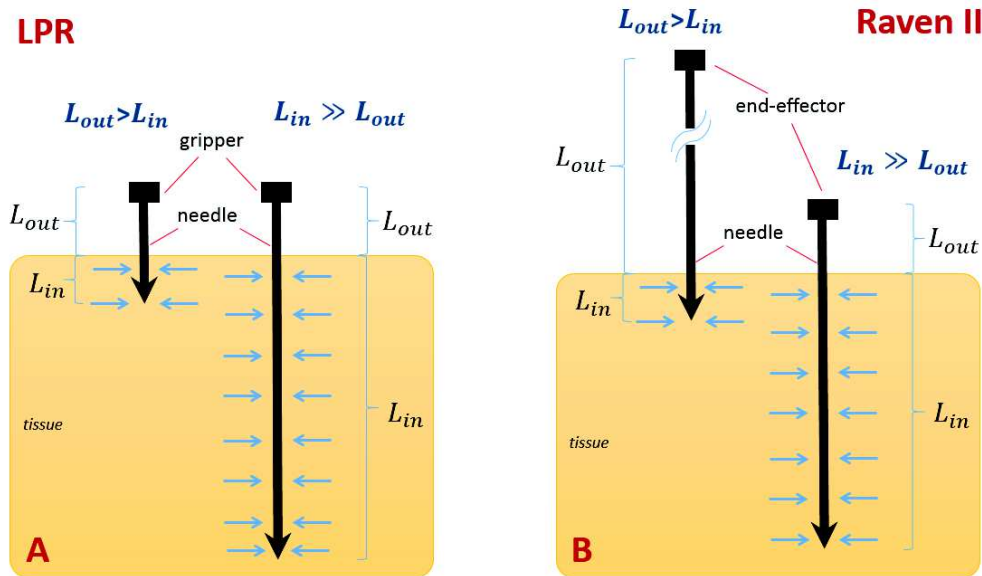


Figure 5.1 - Comparative analysis of L_{out} and L_{in} for LPR (A) and Raven II (B) platforms, taking into account the beginning and final of the needle insertion procedure. Thin narrows indicate the actual region of the needle under effects of clamping forces (actually interacting with the tissue).

5.3. Contributions

This work was developed under the context of the ANR-ROBACUS project that aims to improve the design and development of the teleoperation LPR robot platform. More specifically, this thesis has focused on the development of an image-guided robot-driven system for needle insertion assistance.

The teleoperation architecture and insertion assistance system proposed in this thesis provide various contributions with respect to the conventional IR techniques existing, as well as robotic platform proposed to this context. The Table. 5.2 summarizes the contributions associated to this study and their connection with the context proposed by the ROBACUS project.

The integration of LPR under a teleoperation architecture provides to this platform special status in the literature as the platform that can teleoperate translation, orientation and insertion under CT or MR image-guided abdominopelvic percutaneous procedures. Teleoperation's feasibility is associated to promising benefits in such scenario, including radiation avoidance and safety improvement.

Needle deflection prediction model proposed in this thesis provides contributions with respect to the conventional needle insertion models described in Chapter 2 and summarized in the Table 4.4.

The novel adaptive slope model provides offline and online predictions of needle tip deflections as a function of needle-tissue properties, tip asymmetry and needle insertion depth. The approach is based on an adaptive slope parameter whose updates work as a failure-contingency mechanism and allows online adaptive corrections.

Table 5.2 - Challenges of ARCS scenario and proposals to overcome it. (*) refers to contribution proposed in this thesis.

Challenges		Proposal
Bore space	>	Light Puncture Robot (LPR)
Radiation	>	Teleoperation architecture*
3D imaging acquisition time (~4 seconds)	>	Asynchronous time (store&forward) Prediction modeling*
Ferro-magnetic issues	>	Prediction model*
Needle deflection	>	
Targeting mismatching	>	Planning* + Needle Steering*

The needle deflection model was integrated into an adaptive needle insertion planning system with steering and insertion point assistance. Experiment results showed submillimetric errors. Such promising results obtained during experiments reveal the potential of the approach to overcome uncertainties conditions such as tissue deformation, tissue inhomogeneity, needle-tissue friction, topological changes of the tissue and other modeling approximations.

The approach is compatible to the constraints of the LPR teleoperation platform into needle insertions assistance under ARCS.

5.4. Perspectives

The work developed in this thesis lay on foundations for the development of a teleoperation robot-driven image-guided needle insertion planning platform. Indeed, work is already well under way to develop new version that take into account improvements and further applications, including: automatic tracking of the target (*i.e.*, kidney), movement compensation of the kidney due to needle-tissue interactions, active target compensation due to patient breathing and automatic detection and tracking of the needle tip position into CT and MR images.

Moreover, natural evolution of this work would be advancing model's evaluation over more complex scenario, such as *in-vivo* tissues, followed by evaluation when LPR is ready to go through human applications under clinical scenario. In addition, the model seems to be independent of robot platforms. Therefore, a study could discuss and evaluate its potential of application using different robots, including platforms focused on other domain of applications involving needle insertion (*e.g.*, brachytherapy or intraneural applications). Another study could be the evaluation of the model robustness regarding different needles of different stiffness and tip asymmetries. Finally, the effect of the insertion velocity on the semi-rigid needle deflection has to be studied with attention since this point has already be mentioned in the literature without sharped conclusion.

Study of usability of the system has to be done in order to understand and quantify aspects to be improved, involving the comfort of the user, time and efficacy of the procedure, considering human-in-the-loop aspects when using the teleoperation needle insertion assistance platform.

Overall, the modular teleoperation architecture was stable during the experiments using the described hardware setup. However, we observed some constancy issues when the system was running in lower computational-power machines. It happens because the master pc has to handle very computing-consumer applications, including 3D graphical user interface and real-time master device control. In order to save computational resources, parallel implementation of the real-time master device control algorithm could be implemented. Moreover, one full core of the master computer could be exclusively dedicated to the control task in order to assure priority for its use.

General Conclusion

Moreover, it could be evaluated the impact of more frequent online updates of tissue properties over the system performance. The use of 3D elastography maps could aid to supply such information at the region of the needle tip. Such maps could be obtained after images registration using ARFI, for example.

For simplicity's sake, the needle steering algorithm neglected the small needle displacements observed in the tissue surface and needle tip when applying lateral movements at the needle base. Such displacements were discussed in Section 3.3. Future work could evaluate the impact of such approximations over the systems performance. Moreover, modeling of such small needle displacements or active needle position updates (tracking) could be integrated as input to improve the accuracy of the needle steering assistance.

5.5. Publications

The following works were published during this thesis:

Dorileo, Éderson; Zemiti, N.; P. Poignet. “Needle Deflection Prediction Using Adaptive Slope Model”. IEEE - 17th International Conference on Advanced Robotics (ICAR), 2015 (to appear).

Dorileo, Éderson; Albakri A.; Zemiti, N.; P. Poignet. “Simplified adaptive path planning for percutaneous needle insertions”. In IEEE - International Conference on Robotics and Automation (ICRA). Seattle, EUA, 2015.

Dorileo, Éderson; Hungr, N.; Zemiti, N.; C. Fouard ; P. Poignet. “Observations of Semi-rigid Needle Deflection in 3D CT/MRI”. Surgetica Workshop, Chambéry le Manège, France, 2014.

Dorileo, Éderson; Hungr, N.; Zemiti, N.; Bricault, I.; C. Fouard ; P. Poignet. “A modular CT/MRI-guided Teleoperation Platform for Robot Assisted Punctures Planning”. CARS - Computer Assisted Radiology and Surgery, Fukuoka, Japan, 2014.

Appendix A: LPR workspace

The 6 DoF allows the LPR robot to perform translations (2DoFs), inclinations (2DoFs), insertion and gripper motions.

A and B in the image are respectively associated with the motions of motors 1 and 2 of LPR: translation along z-axis (120 mm) and inclination about x-axis ($+24^\circ$ to -32°).

C and D indicate respectively, the motions of motors 3 and 4: translation along x-axis (135 mm) and inclinations about z-axis ($+10^\circ$ to -20°).

E concerns motion of the motor 5: vertical translation (insertion stroke distance) and F, the gripper's motion.

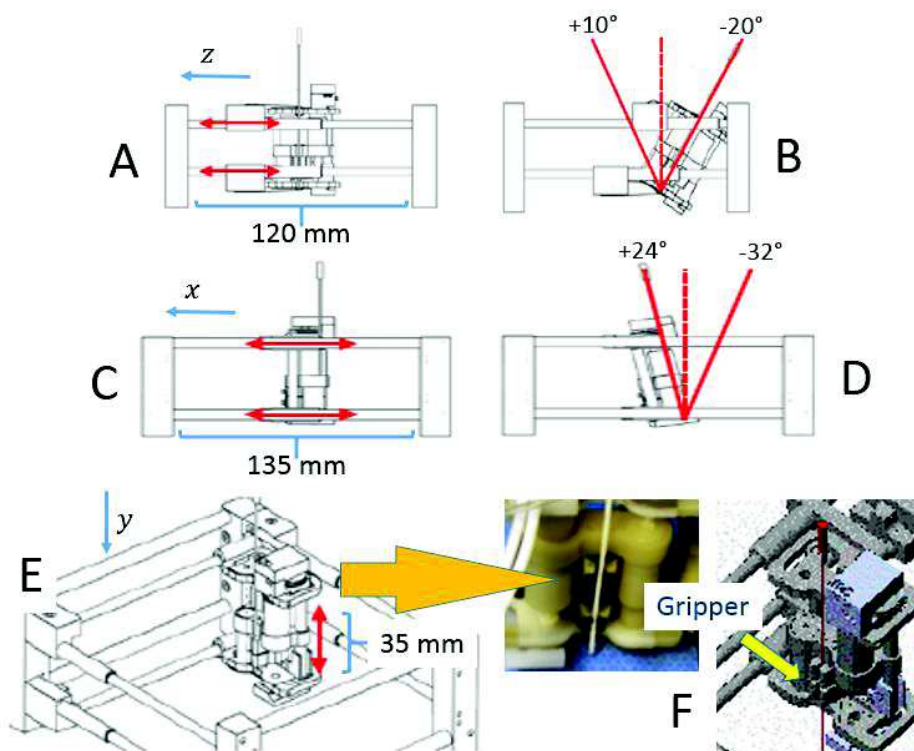
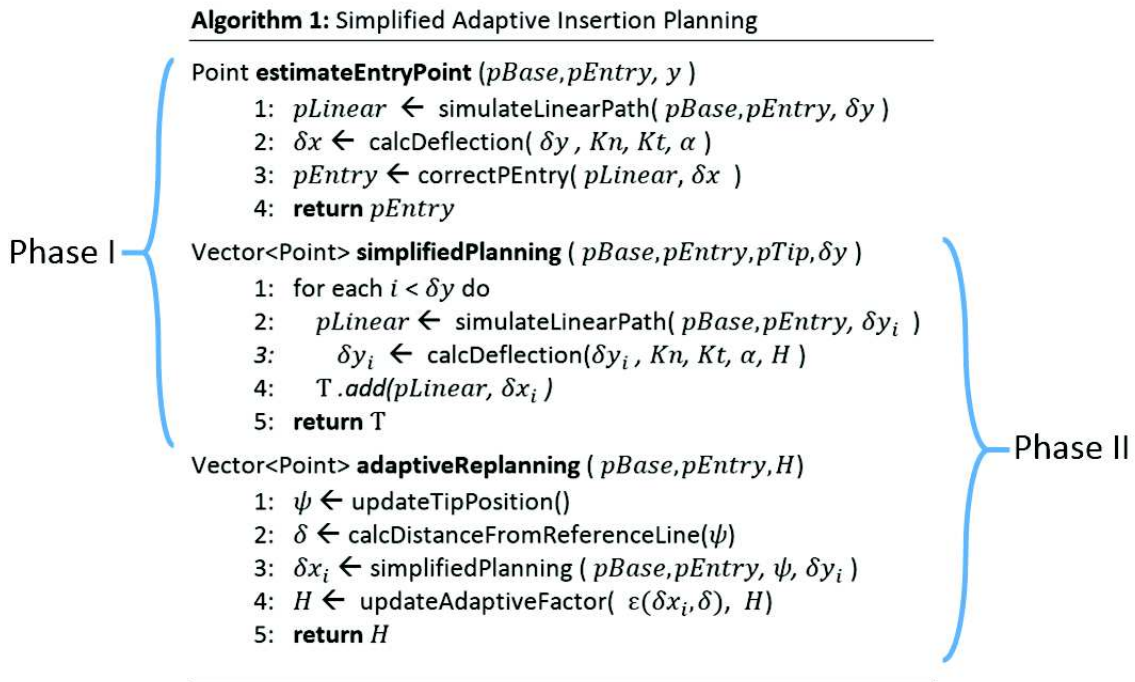


Figure 5.2 - Range of motions and DoFs of LPR pre-clinical prototype. Adapted from (Hung, 2014).

Appendix B:

Planning algorithm

The algorithm proposed for the simplified adaptive needle insertion planning (Algorithm 1) is composed of two phases.



Firstly, tissues' entry point is defined preoperatively by inverting the needle's deflection prediction provided by the model (*estimateEntryPoint*). It is followed by a first (preoperative) planning of the needle insertion in direction to the desired target (*simplifiedPlanning*). Since we cannot steering the needle, the needle is assumed to follow such initial planning along the insertion procedure.

Secondly, the planning approach was also devised to perform an intraoperative prediction of the needle deflection. This step works as a (*sub*)planning task and provides online corrections of the initial planning of the needle insertion and tip position regarding to the full depth of insertion. We called it *sub* because it behaves as a subroutine of the main planning. Indeed, is not recalculating the needle path in order to reach the original target. (At this point, it would be useless, since we are not considering any needle steering strategy for now – such functionality will be include further). Rather, such parallel processing runs the replanning algorithm in order to increase accuracy concerning to the path that the needle is actually following and where the needle tip will actually be in the end of the procedure. Therefore, for each insertion step, the previous path estimation (*simplifiedPlanning*) is adaptively improved taking into account updates of the needle tip position provided by the user's feedbacks through the interactive GUI (*adaptiveReplanning*). This phase can provide intraoperative decision-making support and improve safety of the needle insertion procedure. For example, it allows to anticipate for *abort-insertion* decisions (and withdraw the needle) before the needle passing through some critical biological structure or else, for the case in which the predicted targeting error becomes prohibitive.

Appendix C:

Flowcharts for planning with steering

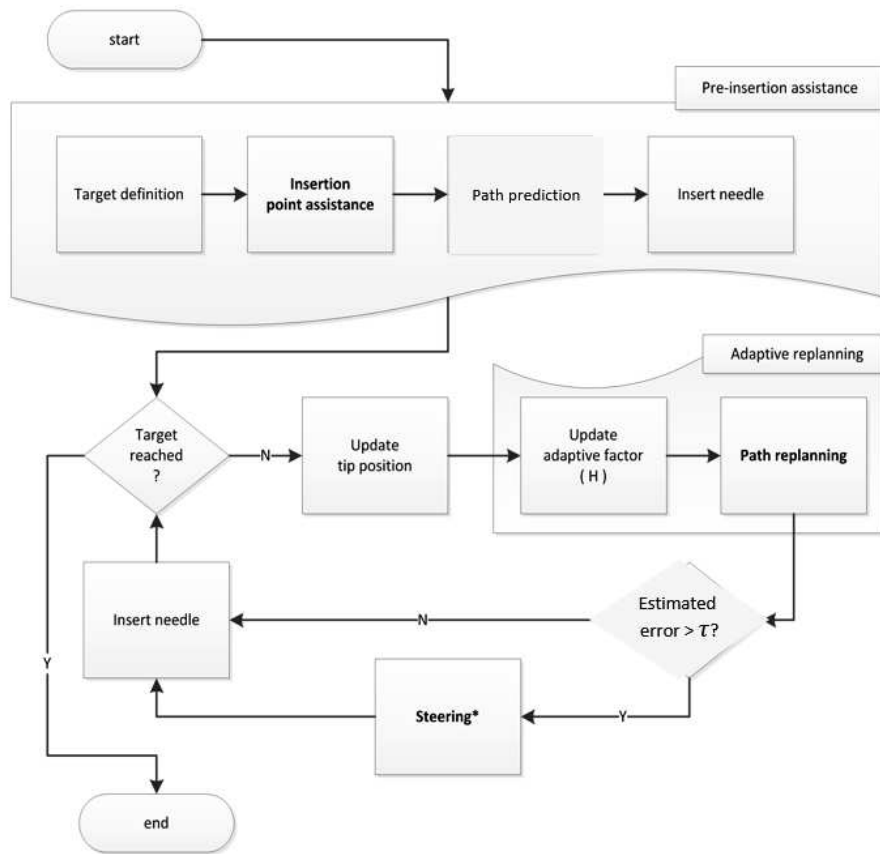


Figure 5.3 - Pseudo-algorithm for adaptive needle insertion planning with steering and tissue's entry point assistance. The steering algorithm (*) is triggered when the predict error is greater than a limit τ , defined according to the maximum error accepted to the procedure. Such variable has the function of avoiding to run unnecessary steering assistance for every loop. For the experiments we set $\tau = 1mm$.

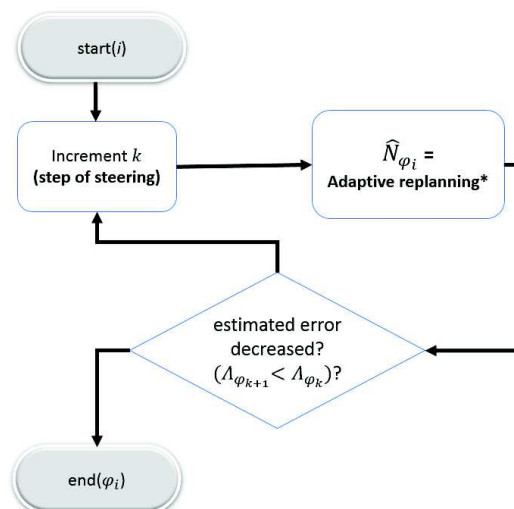


Figure 5.4 - Pseudo-algorithm for semi-rigid needle steering assistance (φ_i) at the insertion time i . The adaptive path replanning algorithm (*) is used to predict effects of incremental changes in the steering angle (φ_k) over targeting accuracy.

Appendix D: Geometric model of Raven-II

This appendix describes geometric model description for the Raven-II surgical platform. Such study was important to customize properly the Davit Harteberg (DH) parameters for the right arms. The description bellow was adapted and extended from the Raven-II documentation. It was useful to install the needle as well as its customized adapter to fix it. It will be described in details as follows.

Robot's design and control require computation of some mathematical models such as transformation models between the joint space (in which the configuration of the robot is defined) and the task space (in which the location of the end-effector is specified). These transformation models are very important since the joint are controlled in the joint space (Dombre and Khalil 2002).

The geometric model of Raven II gives the location of the end-effector as a function of the joint variables. Its geometry is composed of a sequence of two links and three joints. The links are assumed to be perfectly rigid. The Fig. 5.5 shows the angles of the fixed mechanism links ($La_{12} = 75^\circ$ and $La_{23} = 52^\circ$).

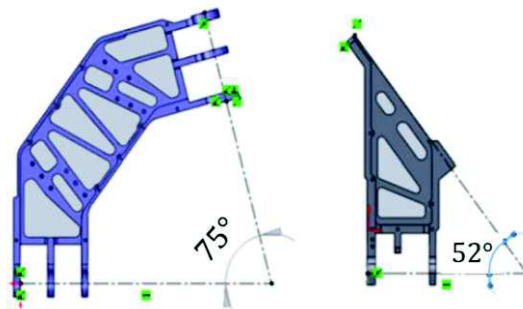


Figure 5.5 - Link angles are designated La_{12} (left, first link) and La_{23} (right, second link). Adapted from (Hannaford, King and Glozman 2013).

The links are numbered such that link 0 constitutes the base of the robot and the link n is the terminal link (Fig. 5.6). There are differences between the left and right arm geometries and link are assigned slightly in left vs. right arm.

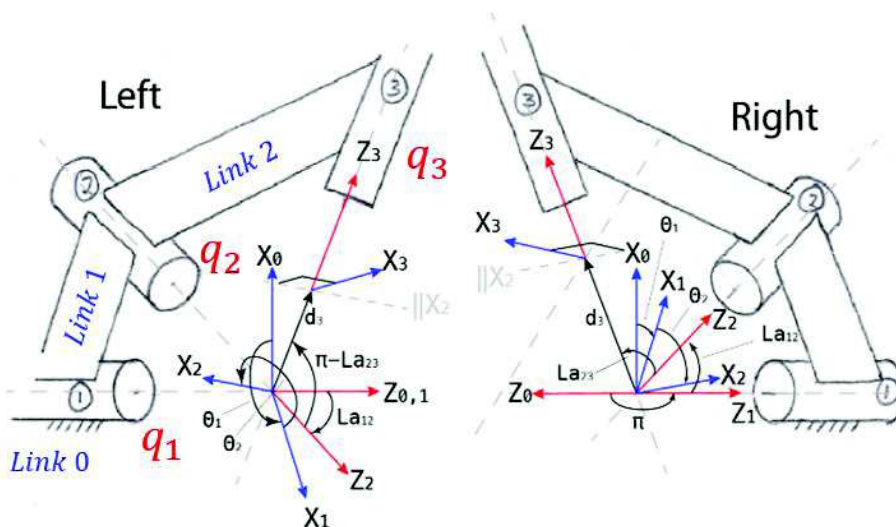


Figure 5.6 - Frame assignments for frames R_0, R_1, R_2 and R_3 . The angles of the fixed mechanism links are expressed as La_{13} and La_{23} . Adapted from (Hannaford, King and Glozman 2013).

The two first joints (q_1 and q_2) are revolute and the third one (q_3) is a prismatic joint. In order to define the relationship between the location of links, a frame R_i is attached to each link i , such that:

- The z_i axis is along the axis of joint i ;
- The x_i axis is aligned with the common normal between z_i and z_{i+1} . If z_i and z_{i+1} intersect, the intersection of x_i and z_i defines the origin of O_i . For the intersecting joint axes, the origin is the point of intersection of the joint axes (Fig. 5.7). When consecutive axes intersect, the common normal x_n is chosen such that $x_n = z_n \cdot z_{n+1}$;
- The y_i axis is formed by the right-hand rule to complete the coordinate system (x_i, y_i, z_i) .

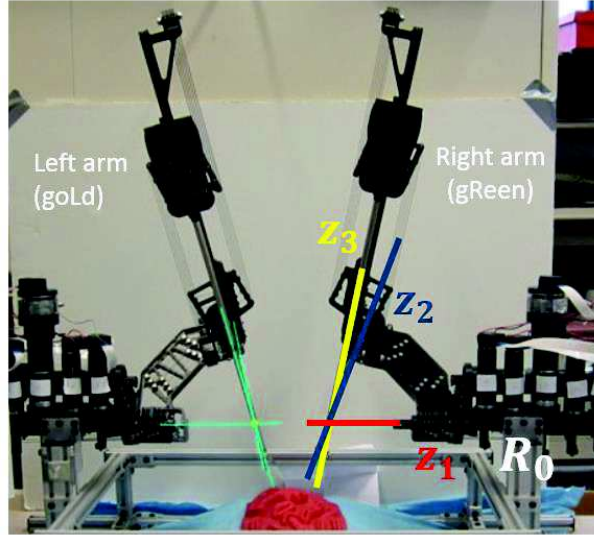


Figure 5.7 - Left (Green) and Right (Gold) Raven-II's arms in the reference pose. Joint axis lines are superimposed showing their intersection at the remote motion center. R_0 indicates the location of the base frame (Link 0) for the right arm. Adapted from (Hannaford, King and Glozman 2013).

The transformation matrix from frame R_{i+1} to frame R_i is expressed as a function of the following geometric parameters.

- α_i : the angle between z_{i-1} and z_i about x_{i-1} ;
- a_i : the distance between z_{i-1} and z_i about x_{i-1} ;
- θ_i : the angle between x_{i-1} and x_i about z_i ;
- d_i : the distance between x_{i-1} and x_i about z_i ;

The variable of joint i , defining the relative orientation or position between links $i - 1$ and i , is either θ_i or d_i , depending on whether the joint is revolute or prismatic, respectively.

The DH parameters for the two arms are given in Tables 5.3 and 5.4.

Table 5.3 - Left (Gold) arm parameters for the positioning joints.

i	α_{i-1}	a_{i-1}	d_i	θ_i
1	0	0	0	θ_1
2	La_{12}	0	0	θ_2
3	$\pi - La_{23}$	0	d_3	$\pi/2$

Table 5.4 - Right (Green) arm parameters for the positioning joints.

i	α_{i-1}	a_{i-1}	d_i	θ_i
1	π	0	0	θ_1
2	La_{12}	0	0	θ_2
3	La_{23}	0	d_3	$-\pi/2$

General Conclusion

In all cases, d_3 is a variable which represents the prismatic joint motion and d_4 is a fixed offset representing the tool length (Fig. 5.8) – the distance from the center point of the four spindles to the origin of frame R_4 ; which is nominally the instrument wrist (King, Kosari and Hannaford, 2014).

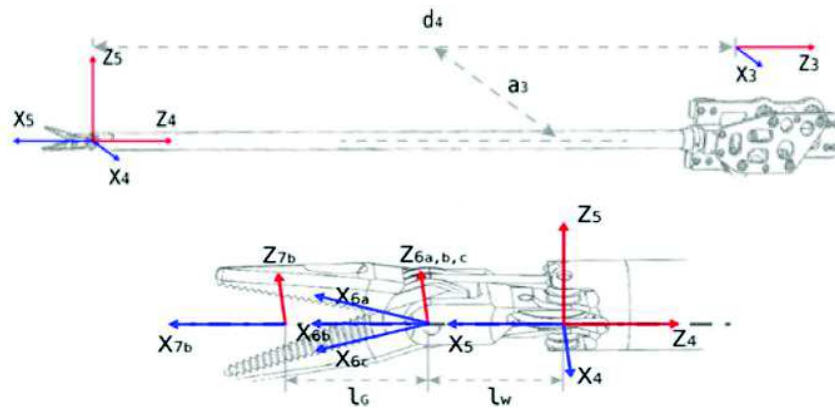


Figure 5.8 - Frame assignments for frames R_4 , R_5 , $R_{6a,b,c}$. Frame R_{6b} indicates a midpoint between the two jaws and R_{7b} frame which can be used when the jaws are open prior to a grasp. Source: (King, Kosari and Hannaford, 2014).

Frame R_3 has its origin at the center of a cross formed between the four spindles and 42.7 mm out from the surface of the sliding rail. Elevation above the rail sets the axis of motion z_3 coincident with the motion center (Fig. 5.9).

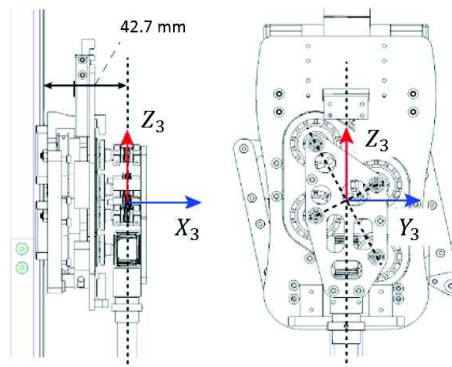


Figure 5.9 - Position of frame R_3 relative to mechanism. Adapted from (King, Kosari and Hannaford, 2014).

Frame assignment and DH parameters are the same for the left and right default instruments and are given in Fig. 5.5.

Table 5.5 - Instrument parameters.

i	α_{i-1}	a_{i-1}	d_i	θ_i
4	0	a_3	d_4	θ_4
5	$\pi/2$	0	0	θ_5
$6_{a,b,c}$	$\pi/2$	l_w	0	$\theta_{6a,b,c}$
7_b	0	l_G	0	0

Note that a_3 may be zero in the case of standard Raven-II instruments. When other instruments are used, there may be an offset between the tool roll axis and the motion center and $a_3 \neq 0$. The length of various tools is represented by parameter d_4 .

The insertion experiments with needle steering required the build of a customized support to fix the needle. It had the impact of change the DH parameters configuration, as defined above. The main modifications in the table was related to the parameters a_3 and d_4 . They were respectively changed to 2.23 cm and 0 cm, as illustrated in Fig. 5.10.

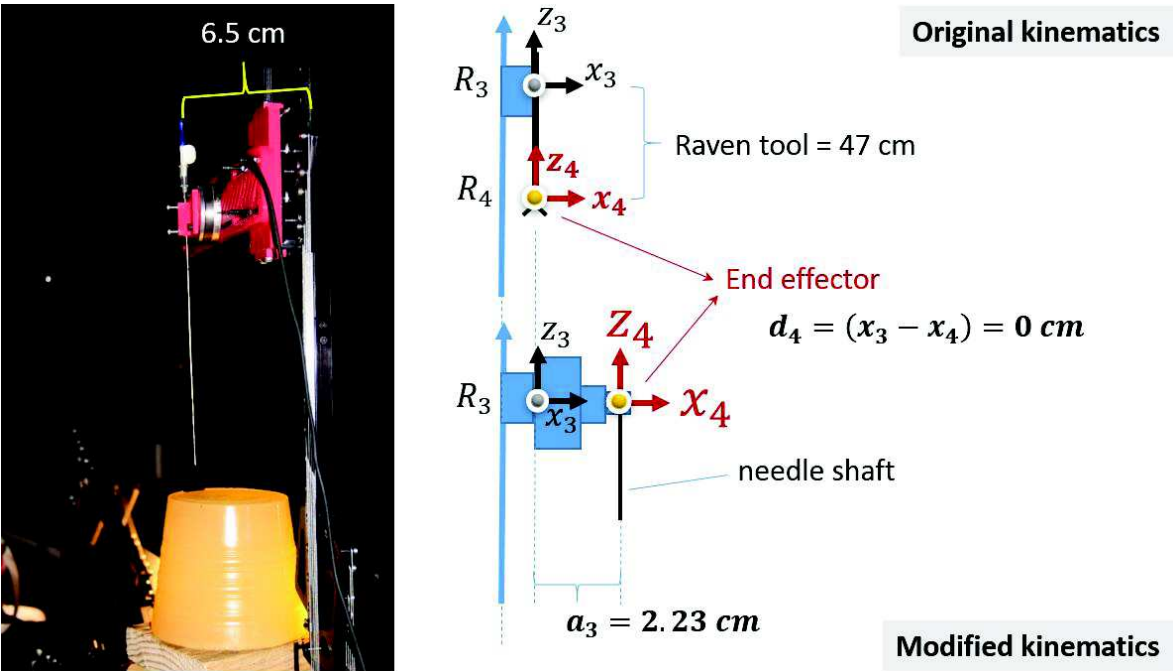


Figure 5.10 - Out of scale analysis of end-effector position when changing Raven tool by the needle supported by the customized adaptor.

References

- Abolhassani, N. and Patel, R.V. (2006) 'Deflection of a Flexible Needle During Insertion into Soft Tissue', Conf Proc IEEE Eng Med Biol Soc, New York City, USA.
- Alterovitz, R., Pouliot, J., Taschereau, R., Hsu, I.-C.J. and Goldberg, K.Y. (2003) 'Needle insertion and radioactive seed implantation in human tissues: simulation and sensitivity analysis', ICRA - International Conference on Robotics and Automation, Taipei, Taiwan.
- Anvari, M. (2007) 'Telementoring and remote telepresence surgery', in Faust, R. *Robotics in surgery: history, current and future applications*, New York: Nova Science.
- Anvari, M. (2007b) 'Remote telepresence surgery: The Canadian experience', *Surg. Endosc.*, vol. 4, no. 21, pp. 537-541.
- Anvari, M. (2011) 'Telesurgery: translation technology to clinical practice', in Rosen, J., Hannaford, B. and Satava, R. *Surgical robotics*, USA: Springer.
- Anvari, M., McKinley, C. and Stein, H. (2005) 'Establishment of the world's first telerobotic remote surgical service for provision of advanced laparoscopic surgery in a rural community', *Ann. Surg.*, vol. 30, no. 241, pp. 460-464.
- Barrett, S., Hanumara, N. and Shepard, R. (2005) 'A Remote Needle Guidance System for Percutaneous Biopsies', ASME, International Design Engineering Technical Conferences, Long Beach, California, USA.
- Bernardes, M.C. (2012) *Robot-assisted steering of flexible needles for percutaneous procedures*, Montpellier: Doctoral dissertation, University of Montpellier.
- Doctor, E.M., Choti, M.A., Burdette, E.C. and Webster III, R.J. (2008) 'Three-dimensional ultrasound-guided robotic needle placement: an experimental validation.', *Int. J. Med. Robot. Comp. Assist. Surg.*, vol. 2, no. 4, pp. 180-191.
- BWH (2015) *3D Slicer*, April, [Online], Available: <http://www.slicer.org/> [04 April 2015].
- Cowan, N.J., Goldberg, K., Chirkjian, G., Fichtinger, G., Alterovitz, R., Reed, K., Kallem, V., Park, W., Misra, S. and Okamura, A. (2011) 'Robotic needle steering: design, modeling, planning and image guidance', in Rosen, J., Hannaford, B. and Satava, R. *Surgical Robotics*, New York: Springer.
- Daftry, S., Maurer, M., Wendel, A. and Bischof, H. (2013) 'Flexible and user-centric camera calibration using planar fiducial markers', Proceedings of the British Machine Vision Conference (BMVC).
- Dehghan, E. and Salcudean, S. (2007) 'Needle Insertion Point and Orientation Optimization in Non-linear Tissue with Application to Brachytherapy', IEEE International Conference on Robotics and Automation (ICRA), Roma, Italy.
- DiMaio, S.P. and Salcudean, S.E. (2002) 'Simulated interactive needle insertion', *Proceedings of the Symposium on Haptic Interfaces for Virtual Environment and Teleoperator Systems*, pp. 344-351.
- DiMaio, S.P. and Salcudean, S.E. (2003) 'Needle insertion modeling and simulation', *IEEE Transactions on Robotics and Automation*, pp. vol 2, pp. 2857-2863.
- DiMaio, S.P. and Salcudean, S.E. (2003) 'Needle steering and model-based trajectory planning', International Conference on Medical Image Computing and Computer-Assisted Intervention, 33-40.
- DiMaio, S.P. and Salcudean, S.E. (2005) 'Interactive simulation of needle insertion models', *IEEE Transactions on Biomedical Engineering*, vol. 7, no. 52, pp. 1167-1179.

- DiMaio, S.P. and Salcudean, S.E. (2005) 'Needle steering and motion planning in soft tissues', *IEEE Transactions on Biomedical Engineering*, vol. 6, no. 52, pp. 965-974.
- Dimension, F. (2001) *Omega 7 - Overview*, [Online], Available: <http://www.forcedimension.com/omega7-overview> [27 Sep 2013].
- Dombre, E. and Khalil, W. (2002) *Modeling, identification & control*, London, UK: Kogan Page Science.
- Dorileo, E., Hungr, N., Zemiti, N., Fouard, C. and Poignet, P. (2014) 'A modular CT/MRI-guided teleoperation platform for robot assisted punctures planning', 28th CARS - Computer Assisted Radiology and Surgery, Fukuoka.
- Duindam, V., Alterovitz, R., Sastry, S. and Goldberg, K.Y. (2008) 'Screw-based motion planning for bevel-tip flexible needles in 3D environments with obstacles', IEEE International Conference on Robotics and Automation, 2483-2488.
- Duriez, C., Guébert, C., Marchal, M., Cotin, S. and Grisoni, L. (2009) 'Interactive simulation of flexible needle insertions based on constraint models', Medical Image Computing and Computer-Assisted Intervention - MICCAI, London, UK, 291-299.
- Engh, J., Podnar, G., Khoo, S. and Riviere, C. (2006) 'Flexible needle steering system for percutaneous access to deep zones of the brain', IEEE Annual Northeast Bioengineering Conference, 103-104.
- Fichtinger, G., Kazanzides, P., Okamura, A., Hager, G., Whitcomb, L. and Taylor, R. (2008) 'Surgical and interventional robotics: Part II'.
- Fouard, C., Deram, A., Keraval, Y. and Promayon, E. (2012) 'CamiTK: A Modular Framework Integrating Visualization, Image Processing and Biomedical Modeling', *Stud Mechanobiol Tissue Eng Biomater*.
- Friedman, S.G. and Dotter, C. (1989) 'Interventional radiologist', *Radiology*, vol. 172, pp. 921-924.
- Glozman, D. and Shoham, M. (2007) 'Image-Guided Robotic Flexible Needle Steering', IEEE Transactions on Robotics, Vol 23, N.03, 459-467.
- Goksel, O., Dehghan, E. and Salcudean, S.E. (2009) 'Modeling and simulation of flexible needles', *Medical Engineering & Physics*, pp. 1069-1078.
- Goksel, O., Salcudean, S., DiMaio, S., Rohling, R. and Morris, J. (2005) '3D needle-tissue interaction simulation for prostate brachytherapy', Medical Image Computing and Conference on Robotics and Automation, Berlin, 827-834.
- Hannaford, B., King, H. and Glozman, D. (2013) 'Raven-II: An open platform for surgical robotics research', *IEEE Transactions on biomedical engineering*, pp. vol.60, n.04.
- Hauser, K., Alterovitz, R., Chentanez, N., Okamura, A. and Goldberg, K. (2009) 'Feedback control for steering needles through 3D deformable tissue using helical paths', *Proceedings of the Robotics: Science and Systems Conference*, vol. 37.
- Hungr, N. (2014) *Conception et évaluation de systèmes robotiques de ponction d'aiguilles percutanées sous contrôle d'imagerie médicale*, Grenoble: Doctoral dissertation. University of Grenoble.
- Hungr, N., Fouard, C., Robert, A., Bricault, I. and Cinquin, P. (2011) 'Interventional Radiology Robot for CT and MRI Guided Percutaneous Interventions', MICCAI, Toronto, 137-144.
- Kataoka, H., Washio, T., Audette, M. and Mizuhara, K. (2001) 'A model for relations between needle deflection, force and thickness on needle penetration', International Conference on Medical Image Computing and Computer-Assisted Intervention, vol 2208, pp. 966-974.
- Kataoka, H., Washio, T. and Chinzei, K. (2002) 'Measurement of the tip and friction force acting on a needle during penetration', International Conference on Medical Image Computing and Computer-Assisted Intervention, vol. 2488, pp. 216-223.

- Kavoussi, L., Moore, R., Partin, A., Bender, J., Zenilman, M. and Satava, R. (1994) 'Telerobotic assisted laparoscopic surgery: initial laboratory and clinical experience', *Urology*, vol. 1, no. 44, pp. 15-19.
- Kazanzides, P., Fichtinger, G., Hager, G., Okamura, A., Whitcomb, L. and Taylor, R. (2008) 'Surgical and Interventional Robotics', *IEEE Robot Autom Mag*, vol. 2, no. 15, pp. 122-130.
- Khadem, M., Fallahi, B., Rossa, C., Sloboda, R., Usmani, N. and Tavakoli, M. (2015) 'A mechanics-based model for simulation and control of flexible needle insertion in soft tissue', IEEE International Conference on Robotics and Automation (ICRA), Seattle, US.
- King, H., Cheng, L., Roan, P., Friedman, D., Kosari, S., Glozman, D., Rosen, J. and Hannaford, B. (2013) 'Raven II: Open platform for surgical robotics research', *IEEE Transactions on Biomedical Engineering*, vol. 60, no. 4, pp. 954-959.
- King, H., Kosari, S.N. and Hannaford, B. (2014) *Kinematic analysis of the Raven-II research surgical robot platform*, Santa Cruz, CA: U. C. Santa Cruz.
- Kitware (2015) *Paraview*, [Online], Available: <http://www.paraview.org/> [21 February 2015].
- Kobayashi, Y., Onishi, A., Watanabe, H., Hoshi, T., Kawamura, K. and Fujie, M.G. (2009) 'Developing a Planning Method for Straight Needle Insertion using Probability-Based Condition where a Puncture Occurs', IEEE International Conference on Robotics and Automation (ICRA), Kobe, Japan.
- Kronreif, G., Furst, M., Kettenbach, J., Figl, M. and Hanel, R. (2003) 'Robotic Guidance for Percutaneous Interventions', *Advanced Robotics*, vol. 17, no. 6, pp. 541-60.
- Krupa, A. (2014) 'A new duty-cycling approach for 3D needle steering allowing the use of the classical visual servoing framework for targeting tasks', IEEE Biorob - Biomedical Robotics and Biomechatronics, Sao Paulo, 301-307.
- LaValle, S.M. (2006) *Planning Algorithms*, University of Illinois: Ed. Cambridge.
- Marescaux, j., Leroy J, Gagner, M., Rubino, F., Mutter, D., Mutter, F., Butner, S. and Smith, M. (2001) 'Transatlantic robot-assisted telesurgery', *Nature*, pp. 413, 379-380.
- Margulis, A.R. (1967) 'Interventional diagnostic radiology - a new subspecialty', *AJR Am J Roentgenol*, pp. 99:761-762.
- Maurel, W. (1999) *3D modeling of the human upper limb including the biomechanics of joints, muscles and soft tissues*, Lausanne: Doctoral dissertation. École Polytechnique Fédérale de Lausanne.
- Maurin, B., Bayle, B., Piccin, O., Gangloff, J., Mathelin, M., Doingnon, C., Zanne, P. and Gangi, A. (2008) 'A patient-mounted robotic platform for ct-scan guided procedures', *IEEE Transactions on Biomedical Engineering*, vol. 10, no. 55, pp. 2417-2425.
- McGraw-Hill (2003) *Dictionary of scientific & technical terms*, 6th edition, The Mc Graw-Hill Companies, Inc.
- Melzer, A., Gutmann, B., Remmele, T., Wolf, R., Lukoscheck, A., Bock, M., Bardenheuer, H. and Fischer, H. (2008) 'Innomotion for Percutaneous Image-Guided Interventions', *Eng in Med and Biol Mag*, vol. 27, no. 3, pp. 66-73.
- Misra, S., Reed, K.B., Douglas, A.S., Ramesh, K.T. and Okamura, A.M. (2008) 'Needle-tissue interaction forces for bevel-tip steerable needles', Proceedings of the Annual International Conference of the IEE Engineering in Medicine and biology Society, 224-231.
- Misra, S., Reed, K.B., Schafer, B.W., Ramesh, K.T. and Okamura, A.M. (2010) 'Mechanics of flexible needles robotically steered through soft tissue', *The International Journal of Robotics Research*, vol. 13, no. 29, pp. 1640-60.

- Misra, S., Reed, K.B., Shafer, B.W., Ramesh, K.T. and Okamura, A.M. (2009) 'Observations and Models for Needle-Tissue Interactions', Conf Proc IEEE Eng Med Biol Soc, Kobe, Japan.
- Moreira, P. and Misra, S. (2014) 'Biomechanics-based curvature estimation for ultrasound-guided flexible needle steering in biological tissue', *Annals of Biomedical Engineering*.
- Moreira, P., Peterlik, I., Herink, M., Duriez, C., Cotin, S. and Misra, S. (2013) 'Modelling Prostate Deformation: SOFA versus Experiments', *Mechanical Engineering Research*, pp. 64-72.
- NASA (2011), 01 Apr, [Online], Available: http://www.nasa.gov/mission_pages/NEEMO/about_neemo.html#.VXf6GUZKXkI [10 Jun 2015].
- Nienhuys, H.-W. and Stappen, A.F.v.D. (2004) 'A computational technique for interactive needle insertions in 3D nonlinear material', IEEE International Conference on Robotics and Automation, 2061-2067.
- OECD, H. (2012) *Frequently requested data*, Organisation for Economic cooperation and Development.
- Okamura, A., Simone, C. and O'Leary, M.D. (2004) 'Force modeling for needle insertion into soft tissue', *IEEE Transactions on Biomedical Engineering*, vol. 10, no. 51, pp. 1707-1716.
- Pacchierotti, C., Abayazid, M., Misra, S. and Prattichizzo, D. (2014) 'Teleoperation of steerable flexible needles by combining kinesthetic and vibratory feedback', *IEEE Trans. Haptics*, vol. 4, no. 7, Oct-Dec, pp. 551-6.
- Park, W., Want, Y. and Chirikjian, G. (2010) 'Path planning for flexible needles using second order error propagation', in Chirkjian, G., Choset, H., Moreales, M. and Murphey, T. *Algorithmic foundations of robotics VIII*, Berlin: Springer.
- Popper, K. (1934) 'The logic of scientific discovery', in *Logik der Forschung*, German: Mohr Siebeck.
- Roesthuis, R.J., van Veen, Y.R.J., Jahya, A. and Misra, S. (2011) 'Mechanics of Needle-tissue Interaction', IEEE - International Conference on Intelligent Robots and Systems (IROS), San Francisco, CA, USA, 2557-2563.
- Rösch, J., Frederick, K. and Kaufman, J. (2003) 'The birth, early years and future of interventional radiology', *J Vasc Interv Radiol*, vol. 14, no. 7, July, pp. 841-853.
- Rucker, D.C., Das, J., Gilbert, H.B., Swaney, P.J., Miga, M., Sarkar, N. and Webster, R.J. (2013) 'Sliding model control of steerable needles', *IEEE Trans on Robotics*, vol. 29, no. 5, pp. 1289-1299.
- Schell, B., Eichler, K., Mack, M.G., Muller, C., Kerl, J.M., Czerny, C., Beeres, M., Thalhammer, A., Vogl, T.J. and Zangos, S. (2012) 'Robot-assisted biopsies in a high-field MRI system - First clinical results', *Fortschr Rontgenstr*, vol. 184, no. 1, pp. 42-47.
- Schiavone, P., Promayon, E. and Payan, Y. (2010) 'LASTIC: a light aspiration device for in vivo soft tissue characterization', *Lecture Notes in Computer Science*, vol. 5958, pp. 1-10.
- Seifabadi, R., Iordachita, I. and Fichtinger, G. (2012) 'Design of a teleoperated needle steering system for MRI-guided prostate interventions', Proc. of the Biomedical Robotics and Biomechanics (BioRob), Rome, 793-798.
- Senapati, S. and Advincula, A. (2005) 'Telemedicine and robotics: paving the way to globalization of surgery', *Int. J. Gynecol. Obstet.*, pp. 91, 210-216.
- Simone, C. and Okamura, A.M. (2002) 'Modeling of needle insertion forces for robot-assisted percutaneous therapy', *Proceedings of the IEEE International Conference on Robotics Automation*, pp. 2085-2091.
- Slama, T., Trevisani, A., Aubry, D., Oboe, R. and Kratz, F. (2008) 'Experimental analysis of an internet-based bilateral teleoperation system with motion and force scaling using a model

- predictive controller', *IEEE Transactions on Industrial Electronics*, vol. 55, no. 9, Sept, pp. 3290-3299.
- Stecker, M., Balter, S., Towbin, R., Miller, D., Vañó, E., Bartal, G., Angle, J., Chao, C. and Cardella, J. (2009) 'Guidelines for patient radiation dose management', *J Vasc Interv Radiol*, vol. 20, no. 7, July, pp. S263-S273.
- Stoianovici, D., Cleary, K., Patriciu, A., Mazilu, D., Stanimir, A., Craciunoiu, N., Watson, V. and Kavoussi, L. (2003) 'AcuBot: A Robot for Radiological Interventions', *IEEE Transactions on Robotics and Automation*, vol. 19, no. 5, pp. 927-930.
- Timoshenko, S. and Gere, J. (1972) *Mechanics of materials*, New York: Van Nostrand Reinhold Co.
- Vajargah, B.F. and Asghari, R. (2014) 'Simulation method for solving stochastic differential equations with constant diffusion coefficients', *Journal of mathematics and computer science*, pp. 28-32.
- Vieyres, P., Sandoval, J., Josserand, L., Novales, C., Chiccoli, M., Morette, N., Fonte, A., Avgousti, S., Voskarides, S. and Kasparis, T. (2013) 'An anticipative control approach and interactive GUI to enhance the rendering of the distal robot interaction with its environment during robotized tele-echography: interactive platform for robotized tele-echography', *International Journal of Monitoring and Surveillance Technologies Research (IJMSTR)*, vol. 3, no. 1, pp. 1-19.
- Wall, J. and Marescaux, J. (2013) 'Telemicrosurgery', in Liverneaux, P., Berner, S., Bednar, M., Parekattil, S., Mantovani, R. and Selber, J. *Robot assisted microsurgery*, Springer.
- Wan, G., Wei, Z., Gardi, L., Downey, D. and Fenster, A. (2005) 'Brachytherapy needle deflection evaluation and correction', *Med. Phys.*, vol. 32, no. 4, pp. 902-909.
- Webster III, R., Cowan, N., Chirikjian, G. and Okamura, A. (2004) 'Nonholonomic modeling of needle steering', *Symposium on Experimental Robotics*, pp. 18-21.
- Webster III, R.J., Kim, J.S., Cowan, N.J., Chirikjian, G.S. and Okamura, A.M. (2006) 'Nonholonomic modeling of needle steering', *Int. Journal of Robotic Research*, vol. 25, pp. 509-525.
- Webster III, R.J., Memisevic, J. and Okamura, A.M. (2005) 'Design considerations for robotic needle steering', *IEEE International Conference on Robotics and Automation*, 3588-3594.
- Xiaohui, X., Zhijiang, D. and Lining, S. (2003) 'The design and implementation of real-time internet-based telerobotics', *IEEE Int. Conf. on Robotics, Intelligent Systems and Signal Process*, vol. 2, pp. 815-819.
- Zemiti, N., Bricault, I., Fouard, C., Sanchez, B. and Cinquin, P. (2008) 'LPR: A CT and MR-Compatible Puncture Robot to Enhance Accuracy and Safety of Image-Guided Interventions', *IEEE/ASME Transactions on Mechatronics*, vol. 13, no. 3, pp. 306-315.

List of figures

Figure 1 - Computational and physical systems that outline the work developed in this thesis.	12
Figure 1.1 - Left: Its is possible to insert 12 needles in the cylinder of 1 inch of diameter. Right: Considering the same cylinder, it is possible to insert 22 needles. These needles (22G) are thinner than the previous one (12G).	17
Figure 1.2 - Main Interventional Radiology robots for abdominopelvic procedures.	20
Figure 1.3 - LPR robotic system. Left: main LPR components. Center: parallelogram-type manipulator and needle. Right: Grippers and needle.	21
Figure 1.4 - LPR robot architecture. The needle is denoted by a vertical red line in the left image. Source: (Hung, 2014).	22
Figure 1.5 - Stop mechanism for inserting the insertion stroke. Source: (Hung, 2014).	22
Figure 2.1 - Symmetric and asymmetric forces actuating respectively on prismatic/conic (left) and bevelled (right) needle tips during insertion. Bold arrows indicate the resultant force acting at the distal end. Thin arrows show the clamping forces that cause the friction (Kataoka, Washio and Chinzei, 2002) and are distributed along the needle tip and shaft.	24
Figure 2.2 - Estimated needle force distribution for a 1mm/s insertion: constant along the needle shaft and higher at the tip. Adapted from (DiMaio and Salcudean, 2002).	24
Figure 2.3 - Locations of the tissue surface at different stages of needle insertion. (a) pre-puncture; (b) puncture; (c) post-puncture. y_1, y_2 and y_3 are the positions of the tissue surface relative to a fixed coordinate system before the puncture. Adapted from: (Simone and Okamura, 2002).	25
Figure 2.4 - Schematic of a bevelled needle interacting with soft elastic medium. The 2D model incorporates tip forces generated by rupture toughness (G_C), coefficient of friction (μ), toughness (G_C), nonlinear elasticity (C_{10}) and needle properties: bevel angle (α) and flexural rigidity (EI): Young's modulus (E) and second moment of inertia (I). Adapted from: (Misra et al., 2009)	27
Figure 2.5 - Contribution of various components of the system energy during needle insertion experiments. Source: (Misra et al., 2009).	28
Figure 2.6 - Configuration of a bevel tip needle during steering showing the front and back "wheels" at frames B and C of a superimposed bicycle-like nonholonomic model. This particular configuration presents the z-axes for all three frames pointing into the page. Adapted from (Webster III et al., 2004).	28
Figure 2.7 - A. Planar bicycle model. Needle rotates as a rigid body about a center of rotation defined by the intersection of the two wheel axes constraints. B. Planar unicycle model with a single no-slip constraint in the plain. Adapted from (Webster III et al., 2006).	29
Figure 2.8 - System of coordinates and inputs of the bevelled needle kinematic model. When pushed forward, the steerable needle bends in the direction of its bevelled tip, following an arc of approximately constant radius r. Adapted from (Park, Want and Chirikjian, 2010)	29
Figure 2.9 - Needle devised as a cantilever beam support by springs. Adapted from (Abolhassani & Patel, 2006).	31

Figure 2.10 - Motion of the needle tip with respect to the motion applied to the base determines needle steerability. The tissue Jacobian matrix $J(q)$ depends on the current needle tip configuration given by $q = [x_{tip} \ y_{tip} \ z_{tip}]^T$. Adapted from (DiMaio and Salcudean, 2005).	32
Figure 2.11 - Linear system model. Flexible beam subjected to a number of virtual springs. F_a and F_b are axial and lateral forces at the needle base. F_f is the friction force, w_{0i} is displacement at point i. K_i is the virtual spring coefficient and F_i is the force applied by a virtual spring at each joint. (Glozman and Shoham, 2007)	32
Figure 2.12 - Comparative distance (L) between insertion line and target position. Adapted from (Kobayashi, et al. 2009).	34
Figure 3.1 - Out of scale illustration of the iterative percutaneous procedure. The kinematics-based analysis devises needle path with deviation angle θ between the articulated links. Needle tip deflection δx_i is defined orthogonal to the insertion direction, according to L_i projected using N_{i-1} and N_i, along δy_i.	39
Figure 3.2 - Needle tip deflection modelling. Left: Needle deflections are assumed to be towards the direction of the bevel. Right: Components of the resultant forces.	40
Figure 3.3 - Study of angle and friction cone in the context of needle-tissue interaction.	41
Figure 3.4 - Estimated state of the system is tracked by the needle's deflection prediction model and sequential adaptive updates. Prediction δx_{i+1} is updated using inverse modelling (H_i) that absorbs scenario's uncertainties at the insertion time $i-1$, before the i-th measurement.	42
Figure 3.5 - Scenario setup using the CT scanner. A. imaging room. B. control room. Progressive images of the system were taken during needle insertion.	43
Figure 3.6 - Experiment setup. A. Customized support framework, robot and surgical drape. B. Force sensor C. Ex-vivo tissue pork. D. LPR's grippers (G1 and G2) and needle.	44
Figure 3.7 - Stainless steel bevel-tip needle composed by cannula and trocar.	44
Figure 3.8 - Qualitative tissue stiffness measurement.	45
Figure 3.9 - Three-dimensional reconstructions of percutaneous insertions using LPR.	45
Figure 3.10 - External tissue's deformation (axial direction) at surface level. Three-dimensional reconstruction obtained from CT images	46
Figure 3.11 - Displacement of glass seeds embedded into the PVC phantom tissue. A. xy plane. B. zy plane. C. 3D volume. Units in mm.	46
Figure 3.12 - Left: Manual crop of fiducial points used as needle position ground truth - P1 and P2 indicate LPR grippers positions, P3 points to the tissues surface position and P4 reveals the 3D needle tip position. Right: Needle tip deflection orthogonal to the insertion direction.	47
Figure 3.13 - Force data sample for needle vertically inserted into PVC. The three peaks (narrows) indicate insertion step performed under iterative time.	48
Figure 3.14 - Three-dimensional reconstruction of the system under submillimeter resolution. Image shows insertion sample with lateral motion in the needle base (B-B'). I. Displacement of the needle shaft in the tissue entry point (E'-E); II. Displacement of the tip (P-P') after pivoting in V; III. General view of the system for the three moments, showing main fiducial points.	48

<i>Figure 3.15 - Two-dimensional CT slices of free insertion (left) and insertion followed by lateral motion (right).</i>	49
<i>Figure 3.16 - Force data pattern for needle insertion with lateral motion using LPR. Narrows indicate insertion steps.</i>	49
<i>Figure 3.17 - Left: Surgical drape is attached to the LPR using screws. Right: Zoom showing small holes in to the sheet.</i>	50
<i>Figure 3.18 - The surgical drape works as extra-layer and can help the needle to deflect. In this example, the needle was bended nearly 10 mm even without interaction with elastic medium.</i>	50
<i>Figure 3.19 - Deflection samples of two needle insertions using PVC (A) and pork (B).</i>	51
<i>Figure 3.20 - Average error of the needle deflection predictions for insertions into pork and synthetic soft PVC. Errors were calculated comparing the simulations results with deflections obtained in the experiments.</i>	52
<i>Figure 4.1 - Teleoperated surgery using Zeus system, demonstrated by Dr. Jacques Marescaux in New York on the patient in Strasbourg, France. Source: (Marescaux et al., 2001).</i>	56
<i>Figure 4.2 - Clinical scenario. Source: (Dorileo et al., 2014).</i>	58
<i>Figure 4.3 - Teleoperation architecture.</i>	59
<i>Figure 4.4 - General abstraction of the module integration proposed for the platform. Source: (Dorileo et al., 2014).</i>	61
<i>Figure 4.5 - The state machine was proposed to improve the usability and decrease the user learning time. During the procedure, the system guides the clinician through all the phases and states.</i>	61
<i>Figure 4.6 - Robot setup on the slave side in Grenoble. The robot was placed over a gelatine phantom with 15mm Styrofoam targets.</i>	62
<i>Figure 4.7 - Public demonstration. The radiologist, in Montpellier (A), commands the robot's movements in Grenoble (C). The navigation system (B) provided user guidance during the needle positioning, orientation and insertion in order to reach the target in the phantom (D).</i>	62
<i>Figure 4.8 - Phases of needle insertion planning.</i>	66
<i>Figure 4.9 - Out of scale illustration scheme, according to the deflection model analysis (Pb).</i>	67
<i>Figure 4.10 - Out of scale illustration of deflections and errors according to the problem formulated to the analysis of the tissue's entry point assistance.</i>	68
<i>Figure 4.11 - Customized Raven II platform setup.</i>	69
<i>Figure 4.12 - Position and axial force recorded during the percutaneous insertion procedure under homogeneous tissue (V=30mm/s).</i>	70
<i>Figure 4.13 - Simplified model validation analysis. Deviations observations under linear referential, according to Pb formulation for several soft mediums.</i>	71
<i>Figure 4.14 - Modeling errors according to Pb formulation, for the several mediums.</i>	71
<i>Figure 4.15 - Insertion sequence showing preoperative planning (P) and intraoperative (online) replanning. The adaptive factor (H) updates the expected path and position of the needle (O) for each insertion step.</i>	72

- Figure 4.16 - Online adaptive path planning validation analysis. Distance study motivated by Pb2 formulation.** _____ 72
- Figure 4.17 - Comparative cross-platform evaluation of the adaptive slope deflection model into the training (LPR, 6 samples) and test experiments (Raven II, 44 samples). Results concern needle deflection for offline predictions (without adaptive corrections).**__ 73
- Figure 4.18 - Mechanical differences of the end effectors. A. LPR and B. Raven robot.** _____ 73
- Figure 4.19 - Extended presentation of the adaptive slope model to support needle steering, including the steering angle $\varphi(B, E, B_0)$ as system's input. Inverse and direct model's application, with appropriated play of inputs, supports needle position prediction ($N\varphi$), as well as, sequential updates of the adaptive parameter (H_i).**_____ 75
- Figure 4.20 - Sample of real scene of needle steering. Sequential motions were superimposed to provide sense of motion to the illustrative image. Movements are related to the sequence of three sequential moments. The steering algorithm computes the steering angle φ_i , in order to minimize $\Delta\varphi_{k, i}$, while targeting the virtual point T_i .**_____ 77
- Figure 4.21 - Raven II teleoperation platform customized to perform needle insertion procedures.** 77
- Figure 4.22 - Needle steering assistance with lateral needle motions. Zoom shows in detail visual feedback of the needle path in direction to the target.** _____ 78
- Figure 4.23 - Results of needle steering approach compared with linear-based clinical reference.** 79
- Figure 4.24 - LASTIC device used for preoperative measurement of stiffness at tissue surface level. A. Control and communication card. B. Visual feedback of tissue deformation due to the quasi-static suction forces. C. Negative pressure control and measurement mechanism. D. Suction device with camera and ex-vivo pork tissue.** _____ 80
- Figure 4.25 - Experiment setup for 3D needle steering using LPR and CT scanner. Axial and sagittal images slices were used to provide needle position feedback and online needle steering assistance during the insertion procedure.** _____ 80
- Figure 4.26 - Interactive GUI with AR-based resources. Often, the full set of the needle's fiducials were not entirely visible in every slice (I-III). AR-based resource (IV) improved visual feedback to the user by assembling all the fiducials into a same visual plane. GUI also provided feedback of system's parameters, such as $H, \epsilon_i, \delta y(\delta y_i/\delta y_0)$ and $\epsilon_n + 1$.** _____ 81
- Figure 5.1 - Comparative analysis of L_{out} and L_{in} for LPR (A) and Raven II (B) platforms, taking into account the beginning and final of the needle insertion procedure. Thin narrows indicate the actual region of the needle under effects of clamping forces (actually interacting with the tissue).** _____ 88
- Figure 5.2 - Range of motions and DoFs of LPR pre-clinical prototype. Adapted from (Hung, 2014).** _____ 93
- Figure 5.3 - Pseudo-algorithm for adaptive needle insertion planning with steering and tissue's entry point assistance. The steering algorithm (*) is triggered when the predict error is greater than a limit τ , defined according to the maximum error accepted to the procedure. Such variable has the function of avoiding to run unnecessary steering assistance for every loop. For the experiments we set $\tau = 1\text{mm}$.** _____ 97
- Figure 5.4 - Pseudo-algorithm for semi-rigid needle steering assistance (φ_i) at the insertion time i . The adaptive path replanning algorithm (*) is used to predict effects of incremental changes in the steering angle (φ_k) over targeting accuracy.** _____ 97

List of tables

<i>Table 1.1 - Main robot platforms devised to assist CT/MRI-guided needle insertion for abdominopelvic procedures. The robot validation test is either clinical patient tests (C), live animal tests (A) or phantom tests (P). Robotized needle motions are either translation (T), orientation (O) and/or insertion (I).</i>	20
<i>Table 2.1 - Relation between insertion (v) and rotational (ω) velocities and the correspondent trajectories achieved. Source: (Bernardes, 2012).</i>	30
<i>Table 4.1 - Table of phases and states of the system.</i>	60
<i>Table 4.2 - Summary of the quantified errors according to (Pb).</i>	71
<i>Table 4.3 - Example of targeting errors obtained during experiments using the needle steering approach (S) with LPR and 3D CT images. Last row (L) refers to the needle deflection regarding to the linear reference, during free (open-loop) insertion.</i>	81
<i>Table 4.4 - Needle steering and deflection prediction approaches proposed for different experimental conditions. Some information in the table may be not directly available from the study. Therefore, when applicable, it was deduced (*). For the case in which the information is not applicable or not clearly available in the article, it was set as (n/a).</i>	83
<i>Table 5.1 - List of hypothesis identified as candidate causes of model's convergence for offline predictions.</i>	87
<i>Table 5.2 - Challenges of ARCS scenario and proposals to overcome it. (*) refers to contribution proposed in this thesis.</i>	89

Abstract

This thesis describes the study and development of a robot-driven adaptive needle insertion planning system for assist insertions of semi-rigid beveled needles in percutaneous procedures. The approach is based on a novel needle deflection prediction model that can provides offline predictions and can improve its own performance online due to uncertainties of the environment and modeling approximations. Results obtained from *in vitro* tests, using different robot platforms confirmed the viability of our method. The study presented in this thesis contributes to the works previously developed in the literature, by proposing methods with potential to improve accuracy and feasibility of CT and MRI-compatible teleoperation needle insertion platforms.

Résumé

L'objectif de cette thèse est l'étude et le développement d'un planificateur de trajectoire adaptatif afin d'assister l'insertion d'aiguilles biseautées semi-rigides en procédures percutanées robotisées. L'approche proposée est basée sur un nouveau model de déflexion de l'aiguille qui permet une prédiction précise de la position de la pointe de l'aiguille en préopératoire (hors ligne) et peropératoire (en ligne). L'approche proposée permet de considérer et de compenser les incertitudes dues à l'environnement et aux approximations lors de la modélisation. Les résultats des tests *in vitro* pour différentes plateformes robotiques ont confirmé la viabilité de la méthode proposée. La contribution principale de ce travail de thèse est la proposition et validation expérimentale d'un modèle simplifié de l'aiguille qui permet d'améliorer la précision et la faisabilité des plateformes d'insertion d'aiguille télé-opérées sous guidage CT et IRM.